11-1-2018

Polarization Observables for γp −> K+Λ at Photon Energies up to 5.45 GeV

Shankar Dayal Adhikari
Florida International University, sadhi003@fiu.edu

FLORIDA INTERNATIONAL UNIVERSITY

Miami, Florida

POLARIZATION OBSERVABLES FOR $\gamma p \to K^+\Lambda$ AT PHOTON ENERGIES UP TO 5.45 GeV

A dissertation submitted in partial fulfillment of the

requirements of the degree of

DOCTOR OF PHILOSOPHY

in

PHYSICS

by

Shankar D. Adhikari

2018

To: Dean Michael R. Heithaus
College of Arts, Sciences and Education

This dissertation, written by Shankar D. Adhikari, and entitled Polarization Observables for $\gamma p \to K^+\Lambda$ at Photon Energies up to 5.45 GeV, having been approved in respect to style and intellectual content, is referred to you for judgement.
We have read this dissertation and recommend that it be approved.

David Chatfield

Joerg Reinhold

Brian Raue, Co-Major Professor

Lei Guo, Co-Major Professor

Date of Defense: November 1, 2018

The dissertation of Shankar D. Adhikari is approved.

Dean Michael R. Heithaus
College of Arts, Sciences and Education

Andrés G. Gil
Vice President for Research and Economic Development
and Dean of the University Graduate School

Florida International University, 2018

DEDICATION

This dissertation is dedicated to my parents for their endless love, support and encouragement.

ACKNOWLEDGMENTS

First and foremost, I would like to thank my advisors, Dr. Brian Raue and Dr. Lei Guo, for their guidance and support during this work and for allowing me the freedom to pursue my own ideas.

ABSTRACT OF THE DISSERTATION

POLARIZATION OBSERVABLES FOR $\gamma p \to K^+\Lambda$ AT PHOTON ENERGIES UP TO 5.45 GeV

by

Shankar D. Adhikari

Florida International University, 2018

Miami, Florida

Professor Lei Guo, Co-Major Professor

Professor Brian A. Raue, Co-Major Professor

Study of the excited-state nucleon have been long established as an important tool to understand quantum chromodynamics in the non-perturbative region. Even after decades of study, not all of the excited states predicted by different theoretical approaches have been verified. The disparity between the predicted states and the verified states is known as the "missing baryon problem." The verified states were mostly established using pion beam data or through πN decay channels, but are not sufficient to address the missing baryon problem. In recent years, new experiments were conducted worldwide at `CLAS` in Jefferson Lab, `ELSA` in Bonn, `MAMI` in Mainz, and so on, using electromagnetic probes that also included the study of multiple channels with different final states. Since excited baryon states are broad and overlap, they are difficult to disentangle using cross-section data alone. Thus, polarization observables can play a crucial role in the identification of missing baryons.

The current work uses `CLAS` g12 data, which were obtained from a circularly polarized photon beam incident upon an unpolarized hydrogen target, $\gamma p \to K^+\Lambda$, from `CLAS` at Jefferson Lab. Because of the weak decay of the Λ hyperon, it is possible to measure the polarization observables from decay products, particularly $p\pi^-$ with a 64% branching ratio. We measured the transferred polarization observables C_x and C_z, and the induced polarization P. The measurement covers the center-of-

mass energy range from 1.75 GeV to 3.33 GeV, expanding previous coverage by roughly 500 MeV for the P observable and 800 MeV for the C_x and C_z observables. We produced results for polarization observables via two topologies, $K^+p\pi^-$ and $K^+p(\pi^-)$, and found excellent agreement between them.

The current data, along with the previously published photo- and electroproduction cross section and polarization observables from `CLAS`, `SAPHIR`, and `GRAAL`, are needed in a coupled-channel analysis to find the predicted excited states. The results at higher energies are important for determining the contributions from non-resonant processes, which is a dominant background in the lower energy baryon resonance region.

TABLE OF CONTENTS

CHAPTER PAGE

1 INTRODUCTION 1
1.1 Standard Model 2
1.2 Quantum Chromodynamics 4
1.3 Hadrons 9
1.4 Baryon Spectroscopy 12
1.5 Missing Baryon Problem 20
1.6 Hyperon Photoproduction 25
1.7 Previous studies of $\gamma p \to K^+\Lambda$ 29
1.8 Summary 33

2 EXPERIMENT 35
2.1 Continuous Electron Beam Accelerator Facility (CEBAF) 36
2.2 Photon Tagger 39
2.3 The CLAS Detector 41
2.4 Triggering and Data Acquisition 51
2.5 Event Reconstruction 54

3 EVENT SELECTION 57
3.1 Reaction Channel and topologies 58
3.2 Event Filters 59
3.3 Vertex timing selection 60
3.4 Vertex position cut 62
3.5 Multiple photons 64
3.6 Geometric Fiducial Cuts 65
3.7 Time of flight paddles knockout 66
3.8 G12 Corrections 67
3.9 Kinematic Fitting 70
3.10 Conclusion of Event Selections 74
3.11 Quality Factor 75
3.12 Photon beam polarization 80

4 OBSERVABLE EXTRACTION METHOD 82
4.1 Formalism of hyperon polarization 82
4.2 Extraction of Polarization Observables 86
4.3 Kinematic Binning of Data 93

5 DETERMINATION OF C_x, C_z, AND P 96
5.1 Measurement of C_x, C_z observables 96
5.2 Comparison between two-track and three-track results 101
5.3 Systematic Uncertainty 105

6 FINAL RESULTS AND DISCUSSION 115
6.1 Double polarization C_x and C_z 115
6.2 Recoil polarization P 121
6.3 Conclusion 125

Bibliography 127

APPENDIX 132

VITA 140

LIST OF TABLES

TABLE PAGE

1.1 The six flavors of quarks from the Standard Model that make up all hadronic matter, and their properties. 9
1.2 Delta excited states with overall rating and individual channel rating from the Particle Data Group 2018. 14
1.3 Nucleon excited states with overall rating and individual channel rating from the Particle Data Group 2018. 15
1.4 Comparision of Constituent Quark Model predictions with PDG rating from PDG review of 2018. 21
1.5 Polarization observables listed along with their transversity representation and the type of experiments required to measure them. 27

2.1 Trigger configuration as a coincidence between a start counter and time-of-flight hit in the i^{th} sector or any sector, symbolized as $(\texttt{ST}\times\texttt{TOF})_i$. The $(\texttt{ST}\times\texttt{TOF})$ is called a prong. An added $\times 2$ or $\times 3$ indicates the coincidence of multiple prongs which are not in the same sector. MORA and MORB represent coincidences with tagger hits. 53

3.1 *g12* Running Parameters. 57
3.2 List of removed paddles. 67
3.3 Q-value method probability function and their parameter. 77
3.4 The degree of longitudinal electron polarization (P_e) between each Møller measurements. The uncertainties shown are statistical uncertainties. 81

4.1 Binning scheme applied for W and $\cos\theta^{CM}_{K^+}$ for two-track topology. . . 94
4.2 Binning scheme applied for W and $\cos\theta^{CM}_{K^+}$ for three-track topology. . 94

5.1 Summary of systematic uncertainties from both the scale-type and the point-to-point type. 114

LIST OF FIGURES

FIGURE PAGE

1.1 Organization of the lowest lying baryons in the octet and decuplet of Gell-Mann's eightfold-way 2

1.2 The Standard Model of the elementary particles organized in three generations of matter and the gauge bosons, where the gauge bosons are in last two columns. 3

1.3 The strong coupling constant, α_s, as a function of momentum transfer, Q^2, from different experiments. The curve is the QCD prediction. At large momentum transfer, asymptotic prediction has better explained by the experiments. 7

1.4 Schematic diagram of a baryon based on Constituent Quark Model. The baryons are represented by three valence quarks. Each quark interact with each of the other quarks 16

1.5 Constituent quark model predictions for N^*. Bar colors represents the status of excited states, light color is weakly established whereas dark color represents well established states. 17

1.6 A simple schematic of quarks arrangement in a baryon of diquark model. 18

1.7 Comparision between calculated masses (black line) from the diquark model and experimental masses from PDG for *** and **** states (up to 2 GeV). 18

1.8 Predicted N^* and Δ^* from lattice model. 19

1.9 Photoproduction cross section on a proton target from photon beam of energies E_γ= 0.2 – 2.0 GeV. Multiple channels are shown together and shows the threshold of respective channels as well as the magnitude of cross sections. 22

1.10 Comparing atomic states with baryon states. Atomic states (Top) are narrow and easy to distinguish while baryon states (bottom) are wide and overlapped. 24

1.11 The tree-level Feynmann diagrams for the reaction $\gamma p \to K^+ Y$. From left to right; s-, t-, and u-channel processes. 29

1.12 Total cross section results from previous experiment measurments including SAPHIR, LEPS, CLAS, and ABBHHM. 31

1.13 C_x (top) and C_z (bottom) from CLAS were fitted by the Bonn-Gachina multichannel prediction. 32

2.1 An arial view of Jefferson Lab showing three experimental halls, the underground accelerator facility, as well as other research facilities . . 35

2.2 Diagram of the CEBAF facility with different parts. The injector is near the north linac from where the electron beam is injected into the linac. Linacs accelerate the electron beam until it reaches the expected beam energy, later it passes to the different halls 37

2.3 A pair of superconducting niobium RF cavities. The elliptical bulges on the innermost part of above figure are the RF cavities, were kept perpendicular to the beam line. 38

2.4 Superconducting cavities with standing RF waves. These cavities always produce a positive force because of the acceleration gradient coming from RF waves throughout the electron motion in the cavities. . . 39

2.5 A schematic view of the Hall B tagging system. It includes a radiator from which electrons produce photons through Bremsstralung process. After that the hodoscope and magnetic field assists in measuring the recoil electron energy, hence, the photon beam energy from energy conservation. The photon beam then pass through the collimator to hit the target at the CLAS center. 40

2.6 A photograph of the CLAS detector. This picture was with the time-of-flight detector pulled back towards left showing the six-sector view of the region 3 drift chambers. This picture was taken from the downstream direction. 42

2.7 A schematic diagram of the CLAS detector system. The detector subsystems were color coded to seperate them one from another. This figure removes a sector to show all the parts of the detector. 43

2.8 A schematic diagram of the target cell used during the *g12* run period. The target cell is 40 cm long. 44

2.9 A schematic diagram of the CLAS start counter. 45

2.10 Photograph of the CLAS Superconducting Toroidal Magnet. 46

2.11 (Left) Superconducting Toroidal Magnet and its position in relation with DC Region 1 and Region 3. (Right) Magnetic field map for a torus current of 1930 A, corresponding to maximum field strenght of 20 kG. 46

2.12 Horizontal cut through the CLAS detector at the beam line. The two dashed lines originated from center of target show charged particles traversing the drift chambers of opposite sectors. The dotted lines show the location of torus magnets. 48

2.13 Schematic of Time of flight detector. 49

2.14 Segmented view of CC, where it shows the reflection of Cherenkov light from different mirrors after it was produced. 50

2.15 Seperated view of one sector of the forward EC showing the three planes (u,v, w) of scintillator-lead pairs that make up one of the 13 logical layers. 51

2.16 Trigger Logic — One Sector 53

2.17 Sagitta of a Circular Arc 55

3.1 Missing mass of K^+ before applying any cuts. 60

3.2 Time difference between the start counter vertex time and the RF-corrected tagger time. Events are selected within ± 1 ns. 62

3.3 Event distribution in the *g12* target. Selected events are within the rectangular box drawn by a dark line. 63

3.4 Number of tagged photons for events within the ± 1 ns vertex timing cut. 65

3.5 Effect of nominal fiducial cuts in K^+ and proton. 66

3.6 Photon beam energy (E_γ) before (red) and after (blue) correction. . . 68

3.7 Tansverse momentum balance of $p\pi^+\pi^-$ as a function of azimulthal angle (ϕ) for the proton. (top) Before momentum correction and (bottom) after momentum correction. 69

3.8 Effects of all the *g12* corrections (beam energy, energy loss, and momentum correction.) on the missing mass. red is before corrections and blue is after correction. 70

3.9 Missing mass off K^+ before kinematic fitting (all the previous cuts and corrections were implemented). 72

3.10 Kinematic fitting confidence level distributions for all the events. (a) Kinematic fit to $\gamma p \to K^+ p(\pi^-)$ – the distribution is fairly flat above 0.2. (b) Kinematic fit to $\gamma p \to K^+ p\pi^-$ – the distribution is fairly flat above 0.3, also a small rise at the end. The rise at the end was caused by the *g12* fit parameters for K^+ were taken same as π^+. 73

3.11 (Two-track topology) Missing mass off K^+ after kinematic fitting, with a larger than 5% confidence level cut. 73

3.12 (Missing mass off K^+) Events rejected by the greater than 5% confidence level cut for two-track topology. The distribution shows peak around mass of Σ°. 74

3.13 Missing mass of Kaon for 2 track topology 75

3.14 Missing mass of K^+ for a bin of W, further binned into $\cos\theta^{cm}_{K^+}$ from backward to forward angles. The fitted function was a Voigt plus first-order Chebychev polynomial. 77

3.15 Missing mass of K^+ distribution from 1001 nearest neighbor events including a randomly choosen event of mass shown by magenta vertical line. 78

4.1 Coordinate system definition for measurement of observables C_x, C_z, and P for the Λ hyperon in the reaction $\overrightarrow{\gamma} p \to K^+ \overrightarrow{\Lambda}$. (Top) The rectangular area represents the production plane defined through the incoming beam and scattered kaon. The recoil Λ is written as a vector to represent polarized production. (Bottom) The polar angle of the proton in the Λ rest frame is projected along each of the three axes defined in Λ rest frame. 84

4.2 Beam helicity asymmetry as a function of the angular distribution of the proton. Top panel are used to extract C_x and the bottom panel are used to extract C_z 88

4.3 The distribution of χ^2/ndf from the one-dimensional fit for polarization observables C_x (left) and C_z (right). 90

4.4 The distribution of χ^2/ndf from the two dimensional fit method. . . . 91

4.5 Plots of $\cos\theta^{cm}_{K^+}$ vs W, red lines indicate binning for the two-track topology. 94

4.6 Plots of $\cos\theta^{cm}_{K^+}$ vs W, red lines indicate binning for the three-track topology. 95

5.1 C_x vs $\cos\theta^{cm}_{K^+}$ for different W bins, ranged from 1.75 – 1.94 GeV. The results for C_x were measured using three different methods; the one dimensional fit method (blue), the two dimensional fit method (green), and the maximum likelihood method (red). 97

5.2 C_x vs $\cos\theta^{cm}_{K^+}$ for different W bins, ranged from 2.3 – 3.33 GeV. The results for C_x were measured using three different methods; the one dimensional fit method (blue), the two dimensional fit method (green), and the maximum likelihood method (red). 98

5.3 C_z vs $\cos\theta^{cm}_{K^+}$ for different W bins, ranged from 1.75 – 1.94 GeV. The results for C_z were measured using three different methods; the one dimensional fit method (blue), the two dimensional fit method (green), and the maximum likelihood method (red). 99

5.4 C_z vs $\cos\theta^{cm}_{K^+}$ for different W bins, ranged from 2.3 – 3.33 GeV. The results for C_z were measured using three different methods; the one dimensional fit method (blue), the two dimensional fit method (green), and the maximum likelihood method (blue). 100

5.5 Difference distributions of C_x and C_z observables from the maximum likelihood method and, the one dimensional and the two dimensional methods. 101

5.6 Comparison of results from three-track (red) and two-track (blue) topologies for the C_x observable. 102

5.7 Comparison of results from three-track (red) and two-track (blue) topologies for the C_z observable. 103

5.8 Comparison of results from three-track (red) and two-track (blue) topologies for the P observable. 104

5.9 Difference distribution between three observables. 104

5.10 Difference distributions of C_x, C_z, and P after varying the z-vertex cut from $|z - 90| < 20$ cm to $|z - 90| < 18$ cm and a radial cut from $r < 5.0$ cm to $r < 4.5$ cm. 107

5.11 Difference distributions of C_x, C_z, and P observables after varying the vertex timing cut. A variation was set to be ± 0.9 ns as opposed to the ± 1 ns nominal cut. 108

5.12 Difference distributions of C_x, C_z, and P observables after changing the fiducial cut from nominal to tight cut. 109

5.13 Difference distributions of C_x, C_z, and P observables after changing the 5% confidence level cut to 10% for $K^+p(\pi^-)$ events. 110

5.14 C_x vs $\cos\theta^{cm}_{k^+}$, weighted by a Q-value on each kinematic bin. The modification on the Q-value was done by adding and subtracting by the corresponding Q-value error. 111

5.15 An example of difference distributions for C_x: (left) Difference between measurement with Q-value and $Q + Q_{err}$. (right) Difference between measurement with Q-value and $Q - Q_{err}$. 112

6.1 C_x as a function of $\cos\theta^{cm}_{K^+}$ for different W bins. A W bin reported in each plot is an average value calculated for total events within the bin range. The error bar on each data point includes statistical and systematic error. 116

6.2 C_z as a function of $\cos\theta^{cm}_{K^+}$ for different W bins. A W bin reported in each plot is an average value calculated for total events within the bin range. The error bar on each data point includes statistical and systematic error. 117

6.3 C_x as a function of W for the Λ hyperon in the energy range of $W \in \{1.75, 3.33\}$ GeV and $\cos\theta^{cm}_{K^+}$ bin as indicated in the plots. 118

6.4 C_z as a function of W for the Λ hyperon in the energy range of $W \in \{1.75, 3.33\}$ GeV and $\cos\theta^{cm}_{K^+}$ bin as indicated in the plots.. 119

6.5 C_x vs W; plotted for the *g12* and the *g1c* in the same $\cos\theta^{cm}_{K^+}$ bin. The current measurement (red) overlapped and extends in W bins to previous measurement (black). 120

6.6 C_z vs W; plotted for the *g12* and the *g1c* in the same $\cos\theta^{cm}_{K^+}$ bin. The current measurement (red) overlapped and extends in W bins to previous measurement (black) 121

6.7 P as a function of $\cos\theta^{cm}_{K^+}$ for different W bins. A W bin reported in each plot is an average value calculated for total events within the bin range. The error bar on each data point includes statistical and systematic error. 122

6.8 C_x as a function of W for the Λ hyperon in the energy range of $W \in \{1.75, 3.33\}$ GeV. 123

6.9 P vs W; plotted for the *g12* and the *g11* in the same $\cos\theta^{cm}_{K^+}$ bin. The current measurement (red) overlapped and extends in W bins to previous measurement (black). 124

CHAPTER 1

INTRODUCTION

Particle physics started when people got curious about the composition of matter around the 6th century BC. At the early stage, it was all about philosophical reasoning rather than experimentation and empirical observation. During the ancient Greek era, different philosophers such as Leucippus, Democritus, and Epicurus proposed that the matter is made of invisible particles called "atomos," meaning "uncut" in Greek. In the 19th century, the discovery of the electron by J.J Thomson [1], succeeded by the Rutherford scattering experiment [2], shed light on the modern form of particle physics. During the development of particle physics, there was the discovery of atomic structure where the nucleus (composite system of protons and neutrons) is in the center surrounded by electrons. The proton and neutron are now known as nucleons, and in 1932 Stern *et al.* [3] verified the nucleons has an internal structure. In the evolution of particle physics, new subatomic particles were discovered, like K mesons and hyperons, by the use of cosmic ray and collider experiments. These particles do not belong to the categories of nucleons or the electron, but had different properties. Later in 1964, Gell-Mann came up with the idea of organizing those new subatomic particles based on their properties, called the *eightfold way*. The organization of the lowest lying baryons in the *eightfold way* is shown in Figure 1.1. For the first time, organization of subatomic particles was done based on their properties and their existence. The particles' arrangement pointed out the existence of a new type of particle, that was later observed experimentally, is now known as the Ω^- baryon. Gell-Mann found that three fundamental constituents can be used to describe those subatomic particles, that he named *quarks*. The two-quark system is called a meson, and the three-quark system is called a baryon. These two classes of particles are

collectively known as hadrons. The three fundamental quarks that Gell-Mann first came up with were *up*, *down*, and *strange* quarks. Later three heavier mass quarks were added for a total of six, which are categorized into three generations as shown in Figure 1.2. Gell-Mann won the Nobel prize for this work. The theory of Gell-Mann acts as a basis for the development of the Standard Model.

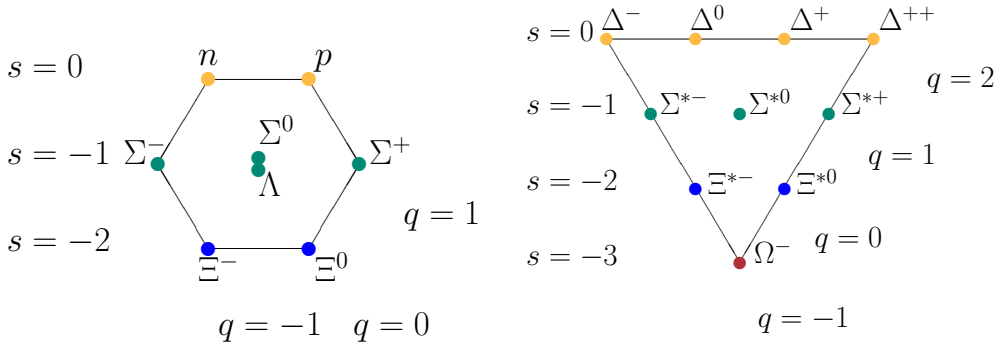

Figure 1.1: Organization of the lowest lying baryons in the octet and decuplet of Gell-Mann's *eightfold-way*. Source [4]

1.1 Standard Model

The Standard Model is a theory that explains the basic building blocks of matter and their interactions. It includes the fundamental particles of three fundamental forces out of four forces (excluding gravitational force), as well as their force carriers. Figure 1.2 shows the Standard Model particles, which includes elementary particles (*quarks* and *leptons*) called *fermions*, and four force-carrier particles that mediate the interaction between *fermions*, called *bosons*. Each of the fundamental forces have corresponding *bosons*; the strong force is carried by "gluons," the electromagnetic force is carried by the "photon," and the weak force is carried by "W" and "Z" bosons. The Gravitational force is not included in the Standard Model. Its force carrier particle, if found in the future, is the "graviton." These fundamental forces have different strengths and work over different ranges. The strong force is the strongest among all

four forces but is limited to a small range, in the order of *femtometer*. For the most part, the weak and strong forces dominate the subatomic world. The electromagnetic force is weaker than the strong force but stronger than the gravitational and weak forces. Both electromagnetic and gravitational forces act over an infinite range.

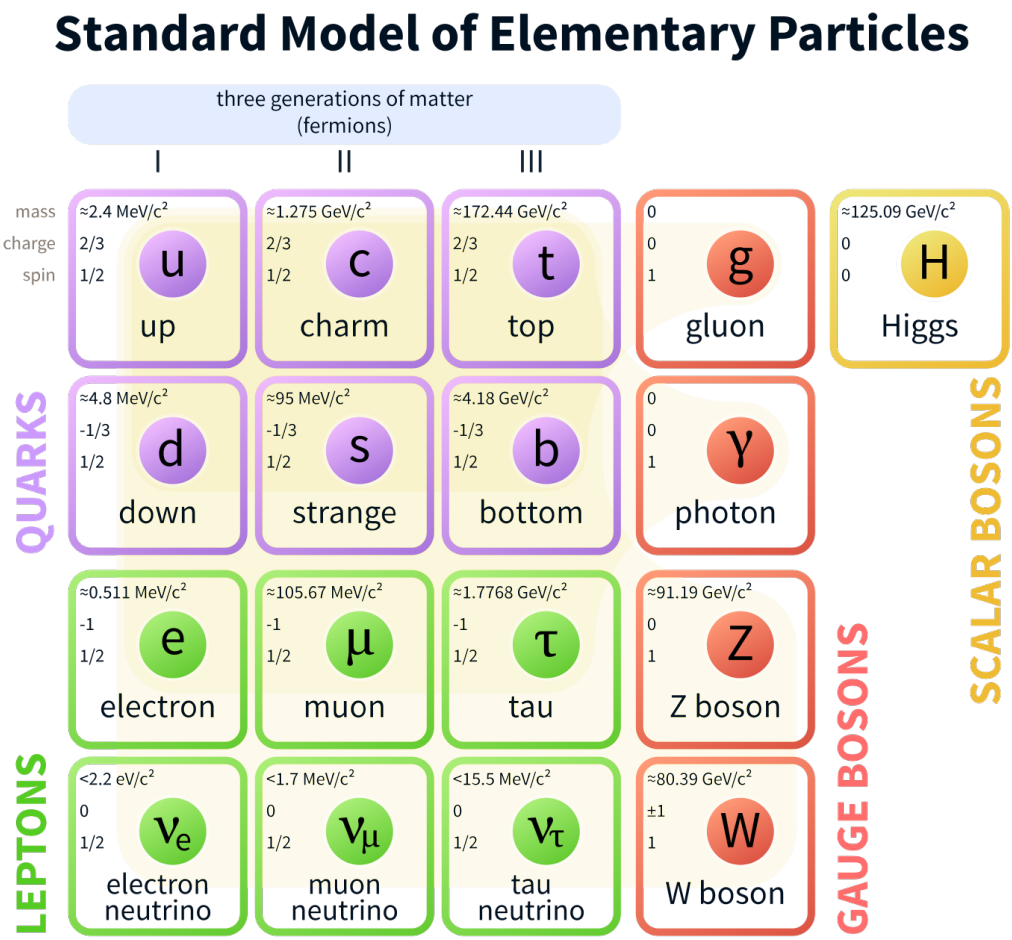

Figure 1.2: The Standard Model of the elementary particles organized in three generations of matter and the gauge bosons, where the gauge bosons are in the last two columns. Souce [5]

In the Figure 1.2, the first three columns are the three generations of fermions and are arranged based on their mass. Quarks are grouped into up and down, charm and strange, and top and bottom as I, II, and III generations, respectively. Similarly,

leptons are grouped as electron and electron neutrino, muon and the muon neutrino, and tau and tau neutrino as I, II, and III generations, respectively. Among leptons, the ν_μ and ν_τ are unstable particles and found in decay processes. The last quark found was the top quark in 1995, and the last lepton, was the tau neutrino found in 2000. The last two columns in Figure 1.2 are *bosons*. The Higgs particle is the last discovered boson in 2012, and is responsible for the *rest mass* of the fundamental particles. The spin quantum number for fermions is a half-integral number ($\frac{1}{2}$, $\frac{3}{2}$, $\frac{5}{2}$, etc) whereas for the bosons, it is an integral numbers (0, 1, 2, etc). All the fundamental fermions, from the standard model share the same spin quantum number ($\frac{1}{2}$). Particles that are made out of fundamental fermions have overall spin that is a combination of the individual fermions. In the case of bosons the spin quantum number is 1, and they belong to the vector field except the Higgs boson which has spin 0, and belongs to the scalar field.

From the standard model, the quark and gluon combinations lead to a bound state composite particle. Different models predict the different bound states of quarks. The existing and verified bound states are two- and three-quarks states. The nature of the bound state particles from quarks and the interaction between quark-quark and quark-gluon is described by a specific type of quantum field theory called Quantum Chromodynamics (`QCD`).

1.2 Quantum Chromodynamics

Gell-Mann came up with the name quarks, as originated from the phrase "Three quarks for Muster Mark" from James Joyce's *Finnegan's Wake* [4]. This name made sense when the three-quark discovery was made. Later three more flavors of quarks were added: *charm*, *top*, and *bottom*. Each flavor of the quarks has a corresponding anti-quark, and is represented as $\bar{q}$, where q is to represent the quark.

Strongly interacting particles, quarks, carry a color charge of red, green, and blue that are analogous with RGB color space, contrary to the electromagnetic interaction where the interacting particle, the electron, has a single electric charge. Also, the strongly interacting force carrier particles, gluons, can interact with themselves, since they carry the color charge. The interaction of a photon with itself is not possible in the electromagnetic interaction because the photon does not have any charge. The antiquark has an opposite color charge and opposite electric charge of the quark. Quarks and anti-quarks do not exist in isolation but are found only in specific combinations mediated by gluons. Experimental observation shows quark and anti-quark combinations must be colorless.

Quantum Chromodynamics is a gauge field theory that describes the strong interactions of colored quarks and gluons, and is the SU(3) component of the SU(3)$\times$ SU(2) $\times$ U(1) standard model of particle physics. Quantum Chromodynamics can be understood as an analogy to quantum electrodynamics (`QED`), which is a theory for the electromagnetic interaction. The `QCD` Lagrangian has the form,

$$\mathcal{L}_{\texttt{QCD}} = \overline{\psi}_i \left(i\gamma^\mu \left(D_\mu\right)_{ij} - m\delta_{ij} \right) \psi_j - \frac{1}{4} G^a_{\mu\nu} G^{\mu\nu}_a, \tag{1.1}$$

where ψ_i is the quark field of flavor i, $G^a_{\mu\nu}$ is the gluon field strength tensor for color-charge a:

$$G^a_{\mu\nu} = \partial_\mu G^a_\nu - \partial_\nu G^a_\mu - g f_{abc} G^b_\mu G^c_\nu, \tag{1.2}$$

and m is the mass of the quark. The term $\left(D_\mu\right)_{ij}$ consists of the self interaction for the quarks and the interaction between the quarks and the gluon fields:

$$\left(D_\mu\right)_{ij} = \partial_\mu \delta_{ij} - g G^a_\mu \gamma^\mu T^a_{ij}. \tag{1.3}$$

Inserting Eq. 1.3 into the Lagrangian yields;

$$\mathcal{L}_{\texttt{QCD}} = i\overline{\psi}_i\gamma^\mu\partial_\mu\psi_i - \overline{\psi}_i m\psi_i - g\overline{\psi}_i G^a_\mu\gamma^\mu T^a_{ij}\psi_j - \frac{1}{4}G^a_{\mu\nu}G^{\mu\nu}_a, \tag{1.4}$$

where the first term is the quark kinetic energy, the second term depends on the quark mass, the third is the quark-gluon interaction, and the last term contains the gluon-gluon interaction. The T^a_{ij} are the SU(3) generators, which can be represented by the Gell-Mann matrices. SU(3) is the group theory notation for the strong interaction referring to the set of all 3×3 unitary matrices with unit determinant. In the quark-gluon interaction term, g is a constant and is the same for all quarks. It may scale with the energy of the interaction, but is flavor independent. Therefore, this theory suggests all quark-gluon interactions are independent of quark flavor.

The strong interaction is a short-range interaction compared to the electromagnetic interaction and has two peculiar features: asymptotic freedom and confinement. In the short range of the strong interaction, or equivalently, high energy or momentum transfer, Q, the quarks behave as if they are free. The strong coupling constant, α_s, measures the strength of the strong interaction, vanishes asymptotically at short distances, which is called asymptotic freedom. The asymptotic freedom in the strong interaction was mathematically derived and discovered by David Gross and Frank Wilczek in 1973 [6], and also independently by David Politzer in the same year [7]. They shared the Nobel prize in 2004 for this work. At high energy or high momentum transfer, `QCD` has a solution using perturbative theory, and hence the mathematical solution of asymptotic freedom was derived. Quite the opposite to asymptotic freedom, at large distances (or equivalent to low Q), the phenomenon of confinement is observed. In this energy regime, the quarks are so tightly bound to each other that they become inseparable. The amount of energy applied to separate the quarks within the hadron favor the creation of new hadrons over the isolation of quarks.

The confinement phenomenon happens in the non-perturbative energy regime where QCD cannot be solved analytically. Hence no analytical proof of confinement exists at present. Figure 1.3 shows the experimental measurement of α_s from high energy scattering experiments [8], where it decreases at large Q and increases as $Q \to 0$.

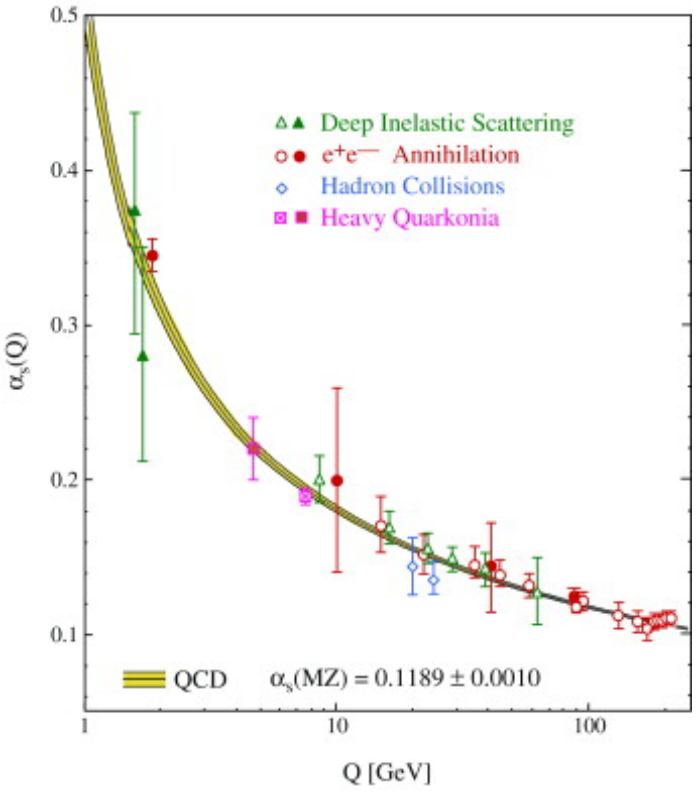

Figure 1.3: The strong coupling constant, α_s, as a function of momentum transfer, Q, from different experiments. The curve is the QCD prediction. At large momentum transfer, asymptotic prediction has better explained by the experiments. Source [8]

To understand the strong interaction, and hence to solve QCD in the low energy region, two theoretical approaches have been developed: Chiral perturbation theory and Lattice QCD. Besides that a phenomenological approach, the quark model, was developed. The theoretical models do not rely on an expansion of the power of coupling constant, but rather applied different approaches. On the other hand, the phenomenological model was proposed on the basis of the experimental discoveries.

Chiral perturbation theory is an effective field theory of QCD. In general, the basic idea of the effective field theory is to treat the light particles as the relevant degrees of freedom, while the heavy particles are reduced to static sources. The dynamics of an effective field theory are described by an effective Lagrangian, which is essentially formulated using the light particles and incorporates all important symmetries and symmetry-breaking patterns.

Lattice QCD (LQCD) is a computational approach to describe the strong interaction, first proposed by K. Wilson in 1974 [9]. In LQCD, the four-dimensional space-time is discretized, usually, on a hypercubic lattice with lattice spacing a, where quarks are placed on sites, and the gluons or gauge field is kept on the links between sites. The definition of LQCD does not rely on a perturbative expansion, rather the non-perturbative calculation is done by evaluating a path integral. For the LQCD simulation, six parameters, such as five light mass quarks (except the top quark) and α_s are fixed on the lattice so that the properties of other particles made up of these quarks and gluons can be determined. The problem in LQCD simulation is that it requires a tremendous amount of computational resources. Because of the development of technology as well as the new approach of GPU computation, LQCD techniques have had success in solving several physics problems.

The quark model was developed as a phenomenological model by Gell-Mann [4] and Zweig [10] to describe the existing and verified two- and three-quarks states discovered in different experiments. In the quark model, the hadrons are defined by the valence quarks and their properties. For example, a proton contains a *uud* quark combination, and each carries $\frac{1}{2}$ spin, so the spin of the proton is the sum of the spin from three quarks.

1.3 Hadrons

Before the quark model, Yukawa introduced pions as the force carrier to explain the interaction between nucleons in the nucleus. Later, different accelerator facilities found other hadrons. These hadrons then contribute to the development of the quark model by Gell-Mann. In the basis of the quark model, hadrons are not elementary particles but are the bound states of quarks and gluon fields. As the gluons do not have any intrinsic property beside the color charge, they do not contribute to the quantum properties of the hadrons. So, the quantum numbers of the hadrons can be determined by combinations of quantum numbers of their constituents quarks and antiquarks. Table 1.1 shows the basic properties of quarks. In addition, the quark model also helped to predict the existence of Ω baryon.

Table 1.1: The six *flavors* of quarks from the Standard Model that make up all hadronic matter, and their properties.

	u	d	c	s	t	b
Q - electric charge	$\frac{+2}{3}$	$\frac{-1}{3}$	$\frac{+2}{3}$	$\frac{-1}{3}$	$\frac{+2}{3}$	$\frac{-1}{3}$
I - isospin	$\frac{1}{2}$	$\frac{1}{2}$	0	0	0	0
I_z - isospin z-component	$\frac{+1}{2}$	$\frac{-1}{2}$	0	0	0	0
S - strangeness	0	0	0	-1	0	0
C - charm	0	0	+1	0	0	0
B - bottomness	0	0	0	0	0	-1
T - topness	0	0	0	0	+1	0

Before going into detail about possible hadrons in the quark model, the different quantum numbers should be examined. The quantum numbers are:

- Q; electric charge.
- B; baryon number.
- S; strangeness .
- J; angular momentum.
- I; isospin.
- P; parity.
- C; charge conjugation.
- G; G-parity.

The quark carries a fractional electric charge as shown in Table 1.1. So, the total charge of hadrons, becomes the additive charge from each of its constituent quarks. Another important quantum number is total angular momentum, J, the sum of orbital angular momentum L and total spin S. Therefore, J varies from $-(L+S)$ to $(L+S)$.

The isospin quantum number (I) tells us how many different charged states of particles exist that have the same spin and parity configuration. The isospin quantum number first introduced by Heisenberg in 1932 to describe nucleons, which have isospin number $\frac{1}{2}$. In that case, the total isospin states are $(2I+1) = 2$. In analogy with spin S, the third component of isospin, I_z describes the isospin state. For example, two isospin projections for nucleons are $\frac{1}{2}$ and $-\frac{1}{2}$, corresponding to the proton and neutron, respectively. Generally, the isospin states are written as,

$$p = \left|\frac{1}{2}, \frac{1}{2}\right\rangle, \; n = \left|\frac{1}{2}, \frac{-1}{2}\right\rangle. \tag{1.5}$$

Another important quantum property is the flavor number, that depends on the quark. Six quarks have been identified in nature and each of them have a unique flavor. So depending on quark flavor, the flavor quantum number is assigned and has the same sign as of the electric charge of the quark. For example the strange quark, has *strangeness* as its flavor. The strange quark carries charge $= -\frac{1}{3}(e)$, and hence the strangeness quantum number is $s = -1$.

The parity operator leads to an inversion of spatial coordinates. There are *even* and *odd* parities for hadrons. In the case of baryons, the parity is given by $(-1)^L$, but for mesons is $(-1)^{L+1}$, because the mesons are made from opposite parity quark-antiquark pairs. For example, in the ground state of baryons, the orbital angular momentum is $L = 0$, so $(-1)^L$, is an *even* parity particle.

The next quantum number is charge conjugation, C, which is responsible for interchanging a particle with its antiparticle. The C operator reverses several properties such as charge, spin, and others. In a $q\bar{q}$ system for an electrically neutral particle such as a π°, to be an eigenstate under the C operator, it must be expressed as

$$C(q\bar{q}) = (-1)^{L+S}, \tag{1.6}$$

where the $L+S$ term has been added to address the parity and spin flip under charge conjugation operation on the quark state. In the case of a charged particle, the C operator is not sufficient, and requires the isospin rotation operator, R. In such cases the charged particle could be an eigenstate of the CR operator, and this is called the G parity operator. The G parity operator is written as $(-1)^{L+S+I}$.

With the knowledge of the quantum numbers, we can now understand the nomenclature of the hadrons. For baryons, its mass, quark content, and quantum numbers I, J^P are sufficient to give it an unambiguous identification. But for the meson, an extra quantum number C is required to give its nomenclature clearly. Any

hadrons that are observed but not allowed by the quark model prediction are called exotic hadrons, such as mesons that have J^{PC}: 0^{--}, 0^{+-}, 1^{-+}, 2^{+-}, 3^{-+}, etc.

Among the three generations of quarks shown in Figure 1.2, u, d, and s quarks are known as light quarks and c, b, and t are known as heavier quarks. The hadrons made up by light quarks are discussed in the present analysis. A baryon is called hyperon if it includes at least one strange quark. The hadrons we will repeatedly mention in the current work are the proton, made by an up-up-down quark combinations, the Λ hyperon made by an up-down-strange quark combination, the K^+ meson made by an up-antistrange, and the π^- made by an antiup-down quark combination.

1.4 Baryon Spectroscopy

The complication to understanding QCD in the non-perturbative regime triggered several questions regarding the nature of the strong interaction, the formation of excited states of hadrons from the quark-gluon interaction, and their consecutive relative degrees of freedom, and many more. All of these questions developed because of the lack of an analytical solution of QCD and confinement. Despite the lack of a solution, physicists developed tools to seek the answers to all of these intriguing questions. One of the convincing tools is spectroscopy of baryons, which helps to map out the excited states and study them.

Similar to atomic spectroscopy where the atoms are studied looking into the decay spectrum, baryon spectroscopy excites baryons and detects radiation such as γ, π's, K's, to maps out the baryon spectrum. Excitation of the atom can be easily done at the local level using electricity, whereas nucleon excitation requires a particle accelerator. Also, the detection of particles emitted from excited baryons requires complicated multi-component detector systems.

The present analysis follows the quest for establishing new excited states of baryons. The Particle Data Group (PDG) lists all the established excited baryons based on their status [11]. The rating that was assigned to states in Tables 1.2 and 1.3 by the PDG ranged from * to ****. The * rating means evidence of the baryon state is poor, ** evidence is fair, *** existence is very likely but needs more information, and **** means that the existence is certain and all the properties are explored. The state with an overall rating of *** or less requires further study through different decay channels to move into ****. Table 1.3 shows an overall rating for N^*'s and a rating for each decay channel. Most of the states of mass < 1800 MeV have a PDG rating of *** or ****, and are seen in either $N^* \to N\pi$ or $N^* \to N\gamma$. On the contrary, the states of mass > 1800 MeV, mostly have the rating * or **. It has been predicted that many of these higher mass states have significant branching ratios into $K\Lambda$ or $K\Sigma$ channels [12]. Therefore the study of $K^+\Lambda$ channel through measuring the cross section and polarization observables is very crucial in order to verify the existence of those * or ** states, as well as particles predicted by quark and LQCD models but not yet observed.

Table 1.2: Nucleon excited states with overall rating and individual channel rating from the Particle Data Group 2018. Source [11].

			Status as seen in					
Particle	J^P	overall	$N\gamma$	$N\pi$	$\Delta\pi$	ΣK	$N\rho$	$\Delta\eta$
$\Delta(1232)$	$3/2^+$	****	****	****				
$\Delta(1600)$	$3/2^+$	****	****	***	****			
$\Delta(1620)$	$1/2^-$	****	****	****	****			
$\Delta(1700)$	$3/2^-$	****	****	****	****	*	*	
$\Delta(1750)$	$1/2^+$	*	*	*		*		
$\Delta(1900)$	$1/2^-$	***	***	***	*	**	*	
$\Delta(1905)$	$5/2^+$	****	****	****	**	*	*	**
$\Delta(1910)$	$1/2^+$	****	***	****	**	**		*
$\Delta(1920)$	$3/2^+$	***	***	***	***	**		*
$\Delta(1930)$	$5/2^-$	***	*	***	*	*		
$\Delta(1940)$	$3/2^-$	**	*	**	*			*
$\Delta(1950)$	$7/2^+$	****	****	****	**	***		
$\Delta(2000)$	$5/2^+$	**	*	**	*		*	
$\Delta(2150)$	$1/2^-$	*		*				
$\Delta(2200)$	$7/2^-$	***	***	**	***	**		
$\Delta(2300)$	$9/2^+$	**		**				
$\Delta(2350)$	$5/2^-$	*		*				
$\Delta(2390)$	$7/2^+$	*		*				
$\Delta(2400)$	$9/2^-$	**	**	**				
$\Delta(2420)$	$11/2^+$	****	*	****				
$\Delta(2750)$	$13/2^-$	**		**				
$\Delta(2950)$	$15/2^+$	**		**				
****		Existence is certain.						
***		Existence is very likely.						
**		Evidence of existence is fair.						
*		Evidence of existence is poor.						

There are a few phenomenological and QCD based lattice calculations developed to explain the existence of baryon excited states. A brief introduction to these models and their predictions are given below.

Table 1.3: Nucleon excited states with overall rating and individual channel rating from the Particle Data Group 2018. Source [11].

			Status as seen in									
Particle	J^P	overall	$N\gamma$	$N\pi$	$\Delta\pi$	$N\sigma$	$N\eta$	ΛK	ΣK	$N\rho$	$N\omega$	$N\eta'$
N	$1/2^+$	****										
$N(1440)$	$1/2^+$	****	****	****	****	**	****					
$N(1520)$	$3/2^-$	****	****	****	****	***						
$N(1535)$	$1/2^-$	****	****	****	***	*	****					
$N(1650)$	$1/2^-$	****	****	****	***	*	****	*				
$N(1675)$	$5/2^-$	****	****	****	****	***						
$N(1680)$	$5/2^+$	****	****	****	****	***						
$N(1700)$	$3/2^-$	***	**	***	***	*	*			*		
$N(1710)$	$1/2^+$	****	****	****	*		***	**	*	*	*	
$N(1720)$	$3/2^+$	****	****	****	***	*	*	****	*	*	*	
$N(1860)$	$5/2^+$	**	*	**		*	*					
$N(1875)$	$3/2^-$	***	**	**	*	**	*	*	*	*	*	
$N(1880)$	$1/2^+$	***	**	*	**	*	*	**	**		**	
$N(1895)$	$1/2^-$	****	****	*	*	*	****	**	**	*	*	****
$N(1900)$	$3/2^+$	****	****	**	**	*	*	**	**		*	**
$N(1990)$	$7/2^+$	**	**	**			*	*	*			
$N(2000)$	$5/2^+$	**	**	*	**	*	*				*	
$N(2040)$	$3/2^+$	*		*								
$N(2060)$	$5/2^-$	***	***	**	*	*	*	*	*	*	*	
$N(2100)$	$1/2^+$	***	**	***	**	**	*	*		*	*	**
$N(2120)$	$3/2^-$	***	***	**	**	**		**	*		*	*
$N(2190)$	$7/2^-$	****	****	****	****	**	*	**	*	*	*	
$N(2220)$	$9/2^+$	****	**	****			*	*	*			
$N(2250)$	$9/2^-$	****	**	****			*	*	*			
$N(2300)$	$1/2^+$	**		**								
$N(2570)$	$5/2^-$	**		**								
$N(2600)$	$11/2^-$	***		***								
$N(2700)$	$13/2^+$	**		**								
****			Existence is certain.									
***			Existence is very likely.									
**			Evidence of existence is fair.									
*			Evidence of existence is poor.									

Constituent Quark Model

The simplest model developed by Capstick and Roberts [13], postulating a hadron is made by bare quarks (set of valence quark), is called the Constituent Quark Model (`CQM`). In the case of baryons, the total number of excited states possible were sym-

metric combinations coming from the three valence quarks properties. The baryon wave function, ψ, is given by,

$$\psi = \psi_{color}\psi_{spin}\psi_{space}\psi_{flavor}, \tag{1.7}$$

where ψ_{color} is the color component, ψ_{spin} is the spin component, $\psi_{spatial}$ is the spatial component, and ψ_{flavor} is the flavor component of the total wave function [14]. Baryons have a color singlet antisymmetric state represented by ψ_{color} in Eq. 1.7. Since ψ has to be antisymmetric for all baryons, thus the rest of the wavefunction $\psi_{spin}\psi_{space}\psi_{flavor}$ in Eq. 1.7, must be symmetric under exchange of any pair of symmetric quarks. All model calculations and theoretical calculations incorporate this symmetry. Figure 1.4 is a proposed schematic diagram for effective degrees of freedom of baryons in the constituent quark model. Figure 1.5 shows the predicted N^* from the `CQM`.

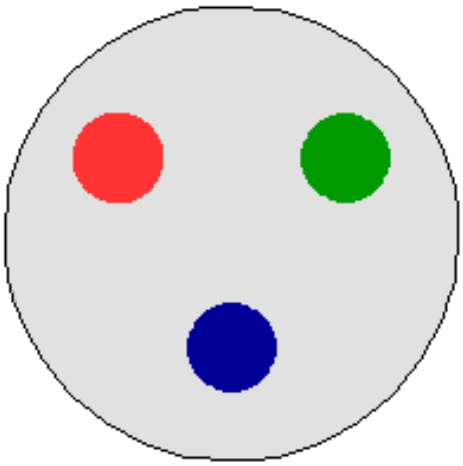

Figure 1.4: Schematic diagram of a baryon based on Constituent Quark Model. The baryons are represented by three valence quarks. Each quark interacts with each of the other quarks.

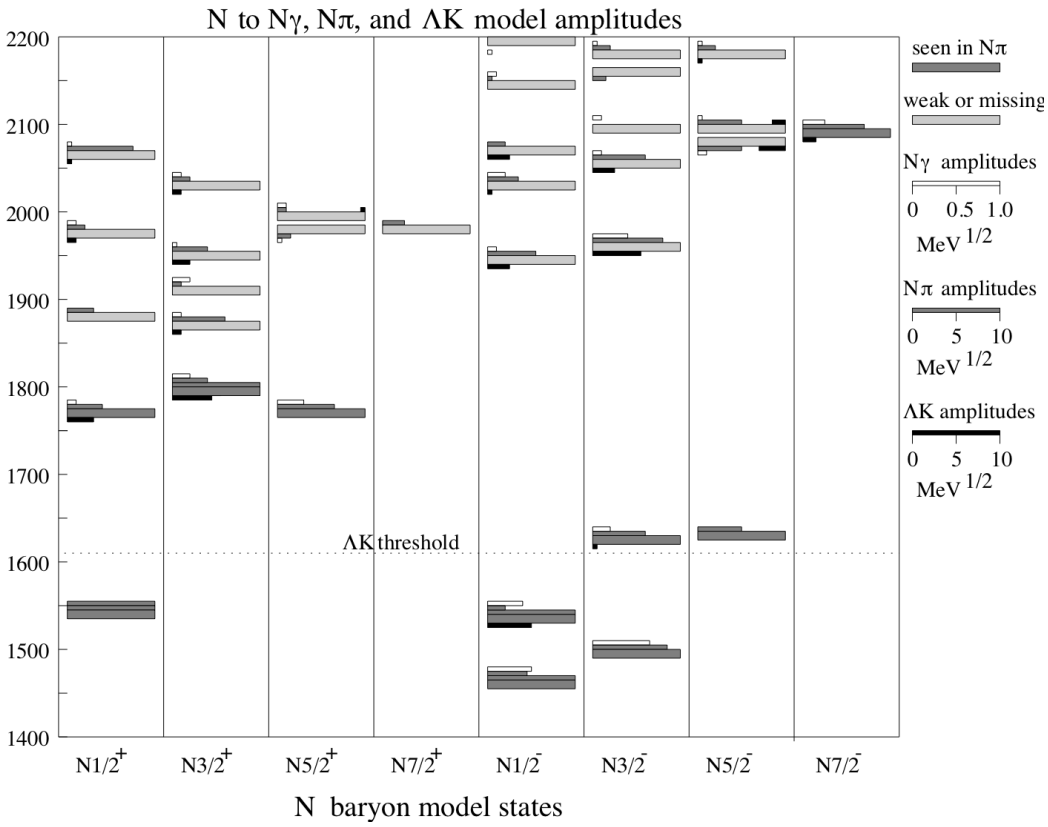

Figure 1.5: Constituent quark model predictions for N^*. Bar colors represents the status of excited states, light color is weakly established whereas dark color represents well established states. Source [13].

Quark-Diquark Model

In one modification to the constituent quark model, two of three quarks "freezes," thereby reducing the effective degrees of freedom from three to two in the baryon and is called the quark-diquark model. Figure 1.6 shows a schematic of the quark-diquark model, where the constraint on the diquark reduces the spatial excitation and hence reduces the possible number of excited states compared to the `CQM`. Figure 1.7 shows predicted N^* and Δ^* masses from the diquark model [15] compared to measured masses for *** and **** states from `PDG`. There are a fewer number of predicted states

higher than 1.7 GeV in the diquark model than in the CQM model.The diquark model cannot accommodate some experimentally verified states.

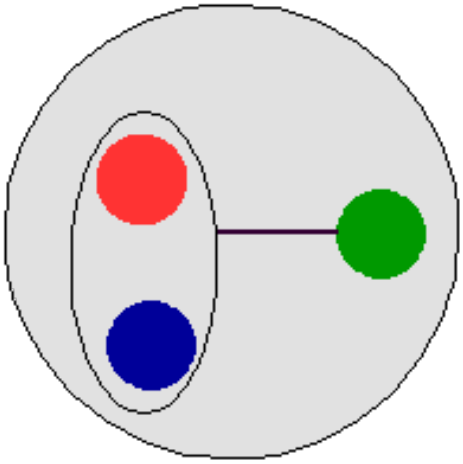

Figure 1.6: A simple schematic of quarks arrangement in a baryon of diquark model. .

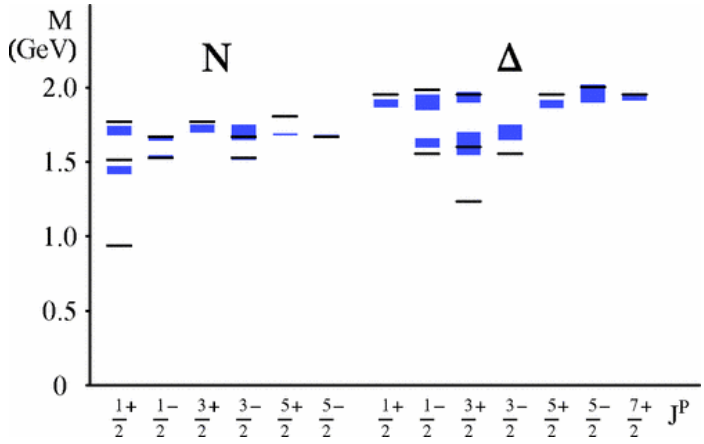

Figure 1.7: Comparision between calculated masses (black line) from the diquark model and experimental masses from PDG for *** and **** states (up to 2 GeV). Source [15]

Lattice QCD

The numerical simulation method, lattice chromodynamics (LQCD), is a computational tool developed to verify the experimentally measured quantities as well as for

predicting quantities that are not easily accessible to experiment. Lattice QCD is the *ab initio* reliable computation where the measurement is done by defining a finite number of points in a Euclidean space-time, called the *lattice*, with the gauge field as links between adjacent lattice sites and quarks defined at each lattice site as anticommuting Grassmann variables belonging to the fundamental representation of SU(3) [9]. This LQCD method is gaining momentum because of the improvement of computation power and algorithms and provides essential input on a wide range of the strongly interacting phenomena, for example, the structure of hadrons, nuclear forces, weak interactions, and more. In the field of hadron structure, the benchmark was considered the prediction of low-lying hadrons, and now extends to excited states. Recent work by Edwards, Dedek, Richards, and Wallace [16], shows predicted N^* are similar to the number of states predicted by the CQM. However, the lattice calculation predicts masses that are much higher than experimental values.

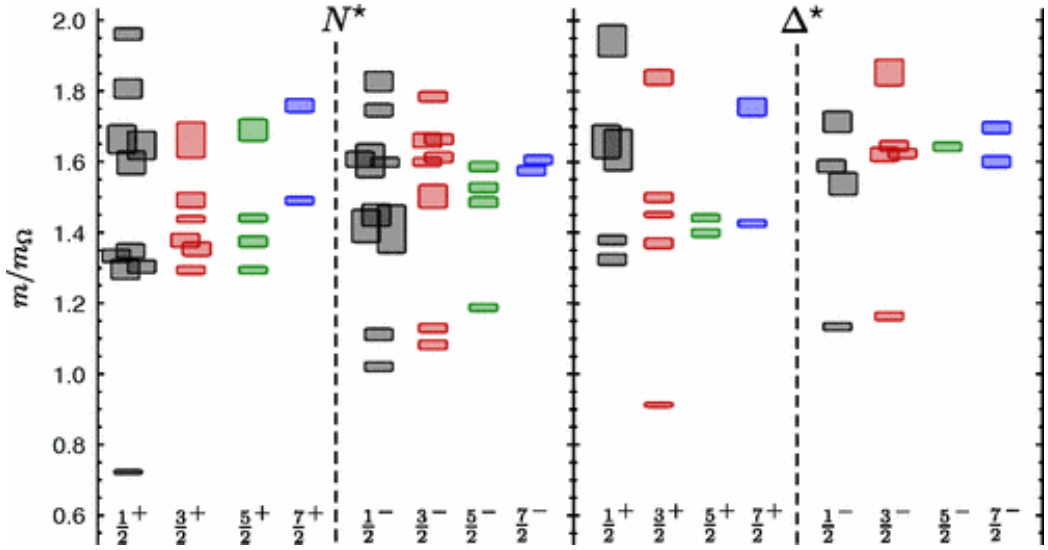

Figure 1.8: Predicted N^* and Δ^* from lattice model. Source [16]

1.5 Missing Baryon Problem

The phenomenological models and also the lattice method predict nearly the same number of excited states, which is large compared to the number of experimentally verified states as shown in Fig. 1.5. The disparity between the predicted states and experimentally verified states is called the *missing baryon problem*. Table 1.4 includes all the nucleon states predicted by constituent quark model and corresponding masses, compared with experimental values from the PDG. The ratings of those experimentally verified states in Table 1.4 suggests most of the higher mass (> 1.7 GeV) states remain undiscovered. There are multiple reasons behind the *missing baryon problem*.

Table 1.4: Comparision of Constituent Quark Model predictions [13] with PDG rating from PDG review of 2018 [11].

J^p	M_{CQM} (MeV)	M_{PDG} (MeV)	Rating	J^p	M_{CQM} (MeV)	M_{PDG} (MeV)	Rating
$1/2^-$	1460	1535	****	$1/2^+$	1540	1440	****
$1/2^-$	1535	1650	****	$1/2^+$	1770	1710	****
$1/2^-$	1945	1895	****	$1/2^+$	1880	1880	***
$1/2^-$	2030			$1/2^+$	1975		
$1/2^-$	2070	2090	*	$1/2^+$	2065	2100	***
$1/2^-$	2145			$1/2^+$	2210	2300	**
$1/2^-$	2195						
$3/2^-$	1495	1520	****	$3/2^+$	1795	1720	****
$3/2^-$	1625	1700	***	$3/2^+$	1870		
$3/2^-$	1960	1875	***	$3/2^+$	1910	1900	****
$3/2^-$	2055			$3/2^+$	1950		
$3/2^-$	2095	2120	***	$3/2^+2030$	2040	*	
$3/2^-$	2165						
$3/2^-$	2180						
$5/2^-$	1630	1675	****	$5/2^+$	1770	1680	****
$5/2^-$	2080	2060	***	$5/2^+$	1980	1860	**
$5/2^-$	2095	2200	**	$5/2^+$	1995	2000	**
$5/2^-$	2180			$5/2^+$			
$5/2^-$	2235						
$5/2^-$	2260						
$5/2^-$	2295						
$5/2^-$	2305	2570	**				
$7/2^-$	2090	2190	****	$7/2^+$	2000	1990	**
$7/2^-$	2205			$7/2^+$	2390		
$7/2^-$	2255			$7/2^+$	2410		
$7/2^-$	2305			$7/2^+$	2455		
$7/2^-$	2355						
$9/2^-$	2215	2250	****	$9/2^+$	2345	2220	****
$11/2^-$	2600	2600	***				
$11/2^-$	2670						
$11/2^-$	2700						
$11/2^-$	2770						
$13/2^-$	2715			$13/2^+$	2700	2700	**

Most of these known states were verified using pion beams (see Fig. 1.10b), and there is a possibility that missing states are not strongly coupled to the pion. As an

alternative, electromagnetic probes were considered an appropriate tool to study the missing states. Figure 1.9 shows cross-section results for multiple channels in photoproduction experiments. From this, it seems that the cross section of strangeness production channels such as $K^+\Lambda$ and $K^+\Sigma^\circ$ cannot be ingnored. Particularly, Capstick [17] suggested that there is a large possibility of some missing states, specifically at high energy, that couple to strangeness production channels.

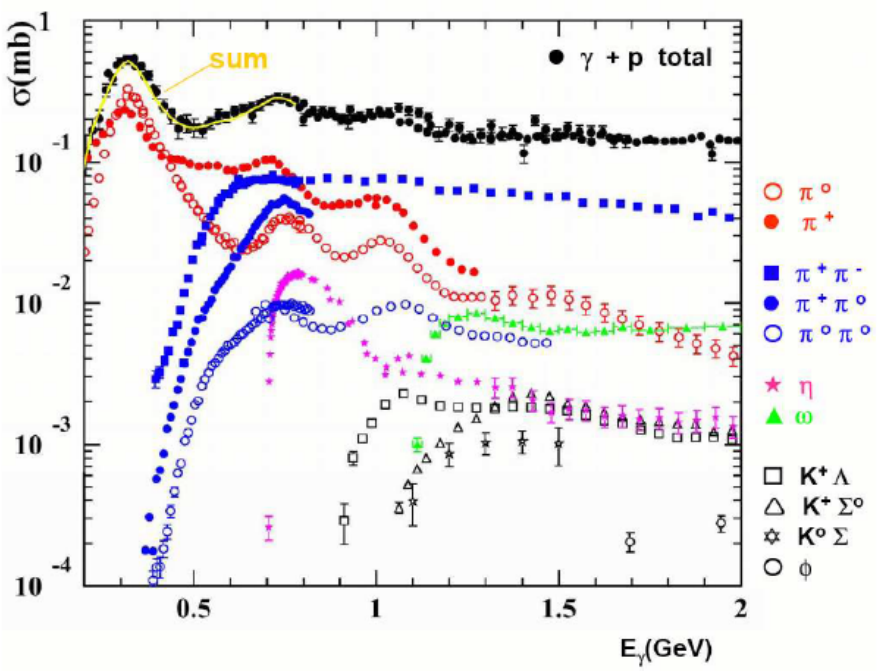

Figure 1.9: Photoproduction cross section on a proton target from photon beam of energies E_γ= 0.2 – 2.0 GeV. Multiple channels are shown together and shows the threshold of respective channels as well as the magnitude of cross sections. Source [18]

As explained in Section 1.4, the baryon spectroscopy technique is like atomic spectroscopy. However, the baryon states are more unstable compared with atomic states, with the typical lifetime being of the order of 10^{-24} s for a strongly decaying resonance. The *Heisenberg Uncertainty Principle* is

$$\Delta E \approx \frac{h}{\Delta t}, \tag{1.8}$$

where h is Planck's constant and ΔE is the energy uncertainity, and correspond to the mass width of the resonances. From the *Heisenberg Uncertainty Principle*, we find the width of the resonance is inversely proportional with particle mean lifetime Δt. The lifetime is approximately 10^{-24} s suggests that the baryon resonances are wide, on the order of 100 MeV. The width of resonance is much larger than the separation between the baryon resonances, thereby leading to highly overlapping states. Figure 1.10 shows the atomic and baryon cross section. The wide and unstable resonances are very difficult to identify by eye (see Figure 1.10b). Figure 1.10b shows a broad peak in the energy range $W \in [1.4, 1.6]$ GeV for $\pi^- p \to X$, comprised of three overlapping states. Even at high energies, the peaks are washed out because of highly overlapping states. This problem suggests the requirement of polarization observables that help us to disentangle those overlapped states. More detail about the photoproduction experiment and different production mechanisms are explained in Section 1.6.

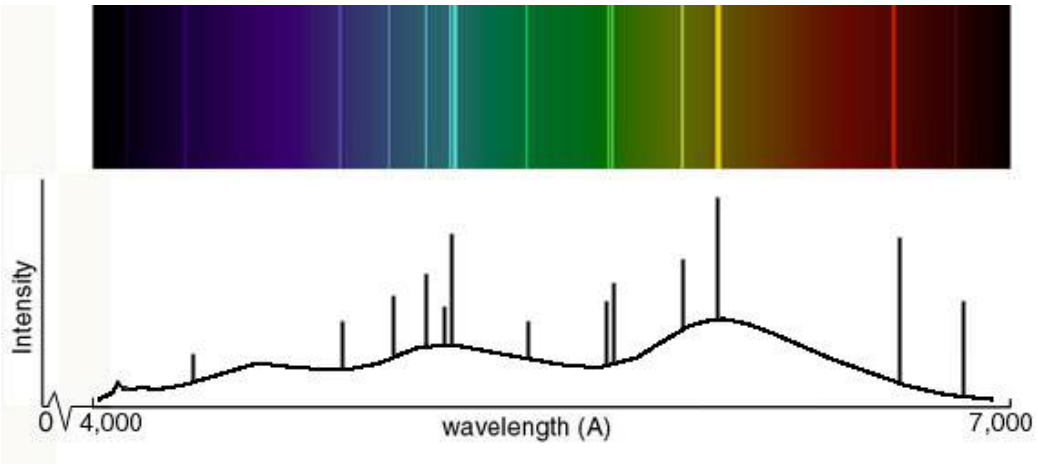

(a) Atomic spectra Source [19]

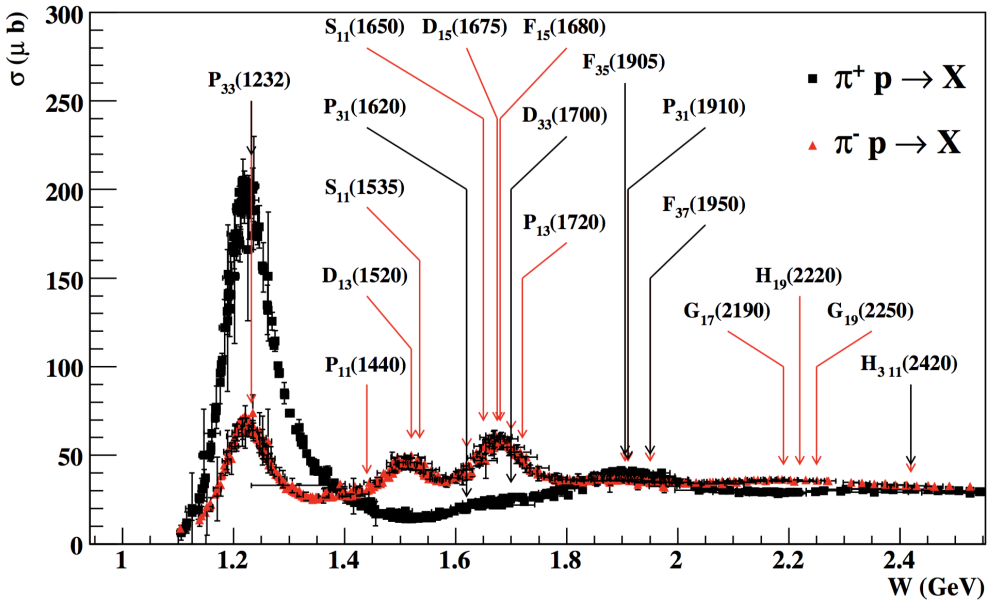

(b) Nucleon resonaces that mostly obtained 4 star from pion production.

Figure 1.10: Comparing atomic states with baryon states. Atomic states (Top) are narrow and easy to distinguish while baryon states (bottom) are wide and overlapped.

There are interfering states of excited nucleons and deltas such as $F_{37}(1950)$, $P_{13}(1950)$, and more. In order to disentangle nucleon states from delta states, we have to choose an isospin filter channel such as $K^+\Lambda$, that couples with nucleon states, but not with delta states.

One of the major motivations of the current work is to provide high-quality data for polarization observables in the $K^+\Lambda$ channel that can be used along with cross section data to determine the existence of these missing states.

1.6 Hyperon Photoproduction

From Barker [20], the photoproduction of strange hyperons (Y) in the reaction $\gamma p \rightarrow K^+Y$ is explained by eight complex helicity amplitudes dependent on the spin states of the particles (2×2×2). But because of parity invariance constraints, these eight amplitudes reduce to four independent ones [21]. The scattering amplitudes include contributions from resonant and non-resonant processes, are entangled with each other, and therefore the phase information of the amplitudes is required in addition to the magnitude to disentangle them. The four transverse amplitudes [20] are

$$\begin{aligned}
b_1 &= \frac{-i}{\sqrt{2}}[(F_1 - F_2 e^{-i\theta})e^{\frac{i\theta}{2}}, \\
b_1 &= \frac{-i}{\sqrt{2}}[(F_1 - F_2 e^{i\theta})e^{\frac{-i\theta}{2}}, \\
b_3 &= -b_1 - \frac{sin\theta}{\sqrt{2}}(F_3 + F_4 e^{-i\theta})e^{\frac{i\theta}{2}}, \\
b_4 &= -b_2 - \frac{sin\theta}{\sqrt{2}}(F_3 + F_4 e^{i\theta})e^{\frac{-i\theta}{2}},
\end{aligned} \tag{1.9}$$

where F's are Chew, Goldberger, Low and Nambu (CGLN) amplitudes [22]. These amplitudes are functions of scattering angle and energy, and are subjected to analyticity and unitarity from the amplitude expression of kaon photoproduction as presented in Ref. [23].

The amplitudes from Eq. 1.9 can be written in terms of helicity amplitudes [20]; N, S_1, S_2, and D as,

$$
\begin{aligned}
b_1 &= \frac{1}{2}[(S_1 + S_2) + i(N - D)], \\
b_2 &= \frac{1}{2}[(S_1 + S_2) - i(N - D)], \\
b_3 &= \frac{1}{2}[(S_1 - S_2) + i(N + D)], \\
b_4 &= \frac{1}{2}[(S_1 - S_2) - i(N + D)],
\end{aligned} \tag{1.10}
$$

where N is the no spin-flip amplitude, $S_{1,2}$ are single spin-flip amplitudes, and D is the double spin-flip amplitude. The helicity is a particle's spin projection in the direction of its momentum.

The four amplitudes in Eqs. 1.10 are complex and completely describe the photoproduction processes. Out of these four complex amplitudes we can derive 16 real numbers and hence we have 16 polarization observables, as shown in Table 1.5. The measurement of these observables in any experiment require beam, target, and recoil hyperon polarization, as shown in the last column of Table 1.5. Based on the fact that observables are linearly related, studies were conducted by different groups [20,21,24] to figure out the number of observables that are sufficient to calculate the amplitudes without any ambiguities. These groups eventually concluded that the measurement of the unpolarized cross section, along with three single polarization observables and four appropriately chosen double polarization observables are sufficient to resolve all the ambiguities.

Table 1.5: Polarization observables listed along with their transversity representation and the type of experiments required to measure them. Source [20].

Observable	Transversity Representation	Polarizations
Differential cross section, $\frac{d\sigma}{d\Omega}$	$\|b_1\|^2 + \|b_2\|^2 + \|b_3\|^2 + \|b_4\|^2$	–
Recoil polarization, P	$\|b_1\|^2 - \|b_2\|^2 + \|b_3\|^2 - \|b_4\|^2$	Recoiling Y
Photon beam asymmetry, Σ	$\|b_1\|^2 + \|b_2\|^2 - \|b_3\|^2 - \|b_4\|^2$	Linearly Polarized γ
Target asymmetry, T	$\|b_1\|^2 - \|b_2\|^2 - \|b_3\|^2 + \|b_4\|^2$	Target
E	$2Re(b_1 b_3^* + b_2 b_4^*)$	Beam-Target
F	$2Im(b_1 b_3^* - b_2 b_4^*)$	Beam-Target
G	$2Im(b_1 b_3^* + b_2 b_4^*)$	Beam-Target
H	$-2Re(b_1 b_3^* + b_2 b_4^*)$	Beam-Target
C_x	$-2Im(b_1 b_4^* - b_2 b_3^*)$	Beam-Recoil
C_z	$2Re(b_1 b_4^* + b_2 b_3^*)$	Beam-Recoil
O_x	$-2Im(b_1 b_4^* - b_2 b_3^*)$	Beam-Recoil
O_z	$2Im(b_1 b_4^* + b_2 b_3^*)$	Beam-Recoil
T_x	$2Re(b_1 b_2^* - b_3 b_4^*)$	Target-Recoil
T_z	$2Im(b_1 b_2^* - b_3 b_4^*)$	Target-Recoil
L_x	$-2Im(b_1 b_2^* + b_3 b_4^*)$	Target-Recoil
L_z	$2Re(b_1 b_2^* - b_3 b_4^*)$	Target-Recoil

In the current work, we measure the induced polarization observable P. Other single-polarization observables such as beam (Σ) and target (T) asymmetries, have

been previously measured [25] for photoproduction of the Λ hyperon. In addition, we are measuring double polarization observables C_x, C_z. When combined results of C_x and C_z with O_x and O_z [25], as well as single polarization observables (P, Σ, T), there is a great chance to determine the model-independent amplitudes for photoproduction of $K^+\Lambda$.

The results from previous measurement of C_x and C_z at low beam energies [26] improved the calculation of helicity amplitudes shown in Eq. 1.10. The current work extends the measurement range beyond the resonance production region to the non-resonant region up to 5.5 GeV photon beam energy. Resonant production is associated with the s and u channels, while t channel production is non-resonant. Resonant production happens after absorbing an incoming γ by the nucleon, N, which then excites an N^*, that then decays through the KY channel. In contrast, non-resonant production is carried by momentum transfer from the incoming photon to the target, thereby leading to exchange of mesons and baryons for the t and u processes, respectively. Figure 1.11 shows the Feynmann diagrams for s, t, and u channel processes. The name s-, t-, and u- channel was choosen based on the Mandelstam variables. For the reaction $\gamma p \to K^+ Y$, these variables can be written as,

$$\begin{aligned} s &= (P_\gamma + P_p)^2, \\ t &= (P_\gamma - P_K)^2, \\ u &= (P_\gamma - P_Y)^2. \end{aligned} \tag{1.11}$$

The other important motivation of the current analysis is to measure the polarization observables within and beyond the resonance production region. The measured value beyond the resonance region can be used to constrain the contributions from the other processes, most of which are background for s channel resonance pro-

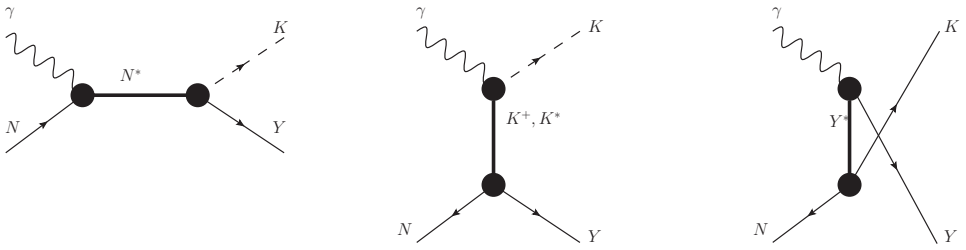

Figure 1.11: The tree-level Feynmann diagrams for the reaction $\gamma p \to K^+ Y$. From left to right; s-, t-, and u-channel processes.

duction. The current work is the first-time measurement of polarization observables for photoproduction of $K^+\Lambda$ at center-of-mass energy higher than 2.45 GeV for C_x and C_z, and higher than 2.84 GeV for P. At higher than 2.38 GeV, we might have a chance to see *missing* resonances that were predicated by `CQM` and `LQCD`.

Within the resonance region, there are several previous results for $\gamma p \to K^+\Lambda$ since 1957. These results include the differential cross section as well as polarization observables. In the section below, we will walk through a few of these measurements and show the necessity of them.

1.7 Previous studies of $\gamma p \to K^+\Lambda$

The research conducted at different experimental facilities such as JLab, ELSA, and LEPS on hadron spectroscopy already verified several excited states of baryons, N^* and Δ^*, along with other hyperon states. But as discussed above, there are additional states that need to be verified by studying their properties. The necessity of $K^+\Lambda$ channel and the polarization observables are described in the previous sections. The main focus in this section is to show the previous measurements and compare them to the model prediction for photoproduction of the $K^+\Lambda$ channel. An emphasis will be

made on where the current data are lacking and what measurements will be needed to further develop a phenomenological understanding of the reaction processes and how those measurements will enhance the world database and constrain various theoretical models for hyperon photoproduction.

Differential cross section

The first cross section results for $\gamma p \to K^+\Lambda$ are from 1958 [27] using bubble chamber measurements. Following this bubble chamber experiment, there were plenty of other experiments [28–38] that measured the cross section from threshold (0.91 GeV) to much higher energies. These results all came before the modern and high-statistics datasets first became available in 1994 from ELSA [39]. As a result of sparse data coverage in the center-of-mass energies and angular distributions, and because of the high systematic uncertainities, these pre-ELSA data had limited utility for understanding the physics of photoproduction of the $K^+\Lambda$ channel.

The modern era for $K^+\Lambda$ cross-section measurement was started with `SAPHIRE` collaboration results [39–41], followed by `CLAS` [42, 43] and `LEPS` [44, 45]. The `CLAS` results for differential cross sections have large statistics and large angular coverage compared with other results, as seen in Figure 1.12. Even though, there is aggreement at small W, there is a discrepency at high W region where the `CLAS` results are consistently higher than the `SAPHIR`. The descripency between the cross section results from `SAPHIR` and `CLAS` was later described in a subsequent measurement from `CLAS` [46].

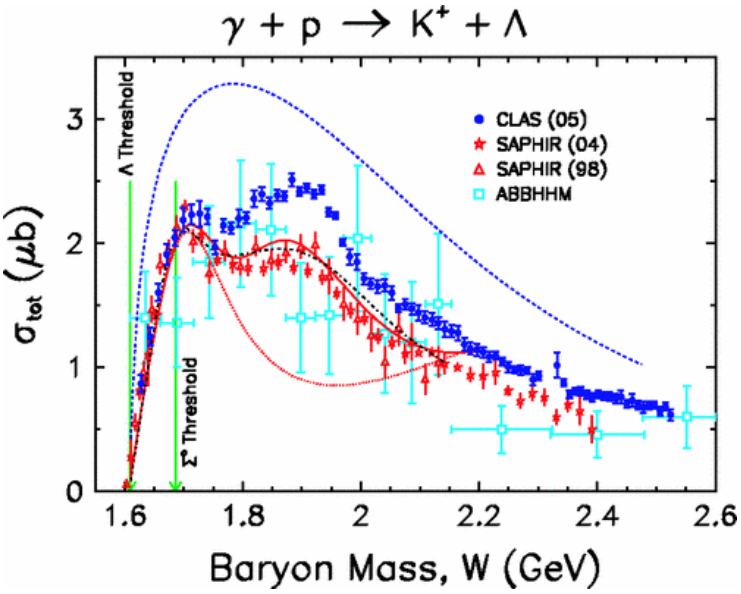

Figure 1.12: Total cross section results from previous experiment measurments including SAPHIR, LEPS, CLAS, and ABBHHM. Source [43]

Polarization observables

Because of the interference of multiple excited states as explained in Section 1.5, polarization observables are great assets for understanding the missing baryon problem. For $K^+\Lambda$ channels there are previous measurement on different polarization observables from CLAS, SAPHIRE, and LEPS. The results from CLAS on hyperon recoil polarization (P) [46], had much higher precision than the previous SAPHIR and LEPS data and also extended the measurement range in center-of-mass energy up to 2.84 GeV. The current work has even higher statistics and extends the measurement in center-of-mass energy to 3.33 GeV. The measurement of P at center-of-mass energy higher than 2.84 GeV is a first time measurement.

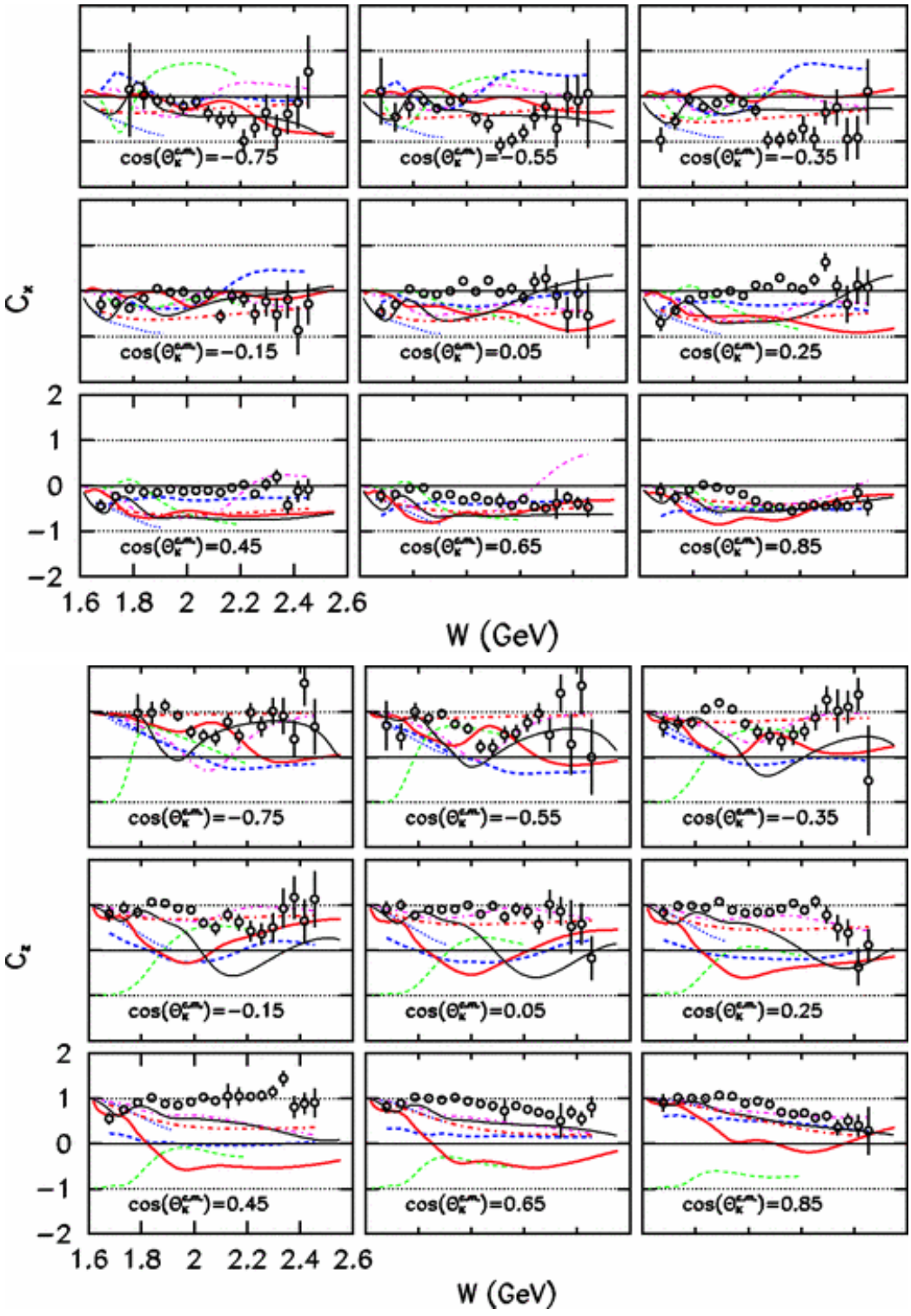

Figure 1.13: C_x (top) and C_z (bottom) from CLAS were fitted by the Bonn-Gachina multichannel predictions. Source [47]

In addition to single polarization observable P, CLAS published first-ever measurements of the polarization transfer observables C_x and C_z for $K^+\Lambda$ in 2007 [26]. These results are plotted in Figure 1.13. From this result, it shows that the C_z component has nearly full polarization transferred from threshold to 1.9 GeV, regardless of kaon production angle. At higher energies, this full polarization behavior appears to fall-off as a function of kaon angle, particularly at backward angles. For C_x, the results are generally closer to zero for most of the kinematic range. In the case of C_x and C_z observables, the present work covers the same kinematic range and extends it to 3.33 GeV.

1.8 Summary

The lack of analytical solution for quantum chromodynamics in the non-perturbative regime creates a difficulty for the understanding of confinement and hence the bound state of quarks and gluons in the hadrons. To address this issue, scientists developed an approach called baryon spectroscopy in analogy to atomic spectroscopy. Similar to the way atomic spectroscopy helps to understand atomic spectra, baryon spectroscopy helps to understand the effective degrees of freedom in the baryon by studying the baryon spectrum, called resonances. However, baryon spectroscopy is more difficult to interpret than atomic spectroscopy because of broad and overlapping nature of the states. To disintangle those overlapped states require not only the cross section but also the polarization observables from different channels.

Past experiments conducted using pion-beam already established a number of excited states that were predicted in the different effective model such as Constituent Quark Model. However, large number of states still need to establish in the experiment. The disparity of predicted and established states is known as missing resonance problem. A possible explanation for these missing resonances is that they perhaps do

not couple strongly to the pion-beam. An alternative approach to study the missing states is the photoproduction experiment. Nonetheless, πN channel was used previously to study the resonance through cross section measurement. Resonances produce wide and large number of states overlapped, so, the strangeness production channel offers the possibility of reducing the density of states and disentangle the interference between the overlapped states. Particularly, the $K^+\Lambda$ channel is an important channel that only coupled with N^* due to isospin conservation. In addition, weak decay of Λ allows us to measure the polarization observables using decay angular distribution. The polarization observables are important that provides phase information of the amplitudes. The current work utilizes a circularly polarized photon beam to measure C_x and C_z observables in $\gamma p \to K^+\Lambda$. Since Λ hyperon produce polarized, so we can measure induced polarization P as well. Our results when compare to models of $K^+\Lambda$ should provide some insight into the strangeness production process. Moreover, the results from this analysis when added to the previous measurements, should facilitate a model-independent determination of any missing states without phase ambiguities.

CHAPTER 2

EXPERIMENT

The data for this analysis were taken at the Thomas Jefferson National Accelerator Facility, also known as Jefferson Laboratory (JLAB), located in Newport News, Va. Jefferson Lab has four experimental halls A, B, C, and D. The current analysis includes data from the past era of JLAB before the facility was upgraded to produce 12 GeV electron beams. The end point electron beam energy in the past was 6 GeV, which only went to three halls: A, B, and C. Hall D was later added for the 12 GeV era. These different halls at JLAB are designed to conduct different physics experiments. The accelerator facility at JLAB is known as the Continuous Electron Beam Accelerator Facility (CEBAF). An aerial view of the JLAB facility is shown in Figure 2.1.

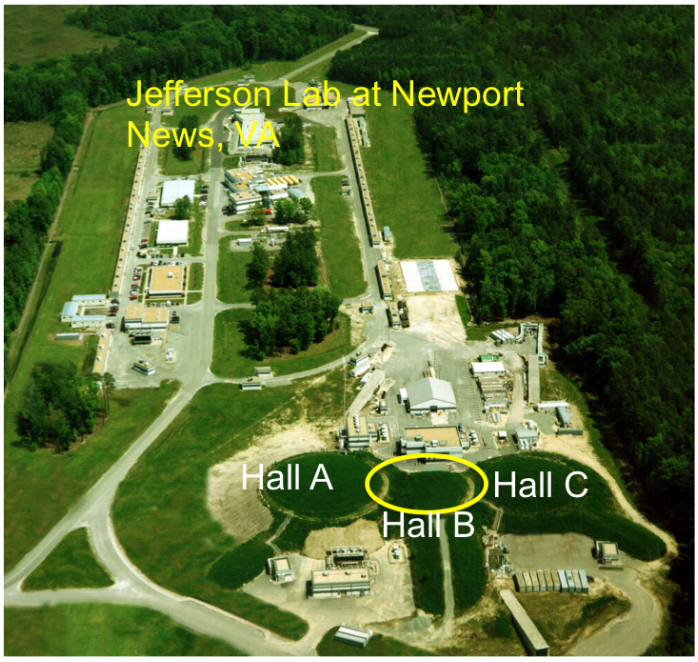

Figure 2.1: An arial view of Jefferson Lab showing three experimental halls, the underground accelerator facility, as well as other research facilities. Source [48]

The data for this experiment came from the *g12* run, where *g* stands for *gamma*, referring to a real photoproduction experiment. The *g12* experiment was conducted in Hall B using the CEBAF Large Acceptance Spectrometer (CLAS) in 2008. The CLAS spectrometer had a large acceptance, covering almost 80% of 4π solid angle, and was optimized for hadron spectroscopy with multiple hadrons in the final state. A tagged real photon beam from the *bremsstralung* process was incident on the liquid hadrogen target, and produced multiple final state particles in the *g12* experiment. The sections below briefly describe the accelerator, the photon tagging system, the components of the CLAS detector, the triggering systems, and the data acquition system for the *g12* experiment.

2.1 Continuous Electron Beam Accelerator Facility (CEBAF)

Figure 2.2 shows a composite view of the accelerator and the position of the different halls at JLab. In the accelerator facility, the electron beam is first produced through the injector, then travels to the two linear accelerators (LINAC) to achieve the required electron beam energy. The CEBAF acclerator facility uses radio frequency (RF) cavities to accelerate the electron beam, which is a significant improvement to the previous copper RF cavities.

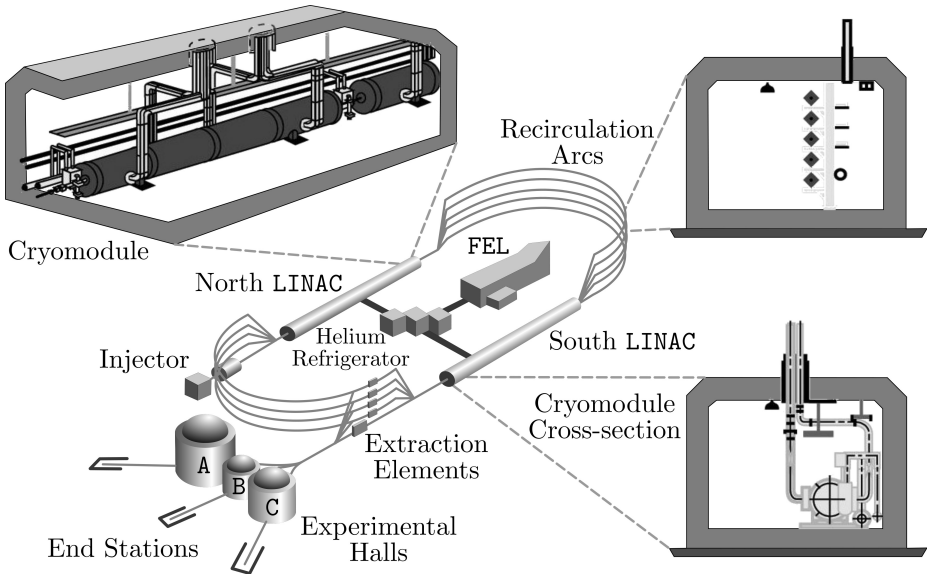

Figure 2.2: Diagram of the CEBAF facility with different parts. The injector is near the north linac from where the electron beam is injected into the linac. Linacs accelerate the electron beam until it reaches the expected beam energy, later it passes to the different halls. Source [48]

The injector had a photo-emission electron gun, a radio frequency (RF) cavity, and a beam chopper. To provide seperate beam properties for the users in three different halls, the CEBAF electron gun used three diode lasers. These lasers were independently pulsed at 499 MHz, 120° out of phase. The overall frequency from the three lasers was 1497 MHz, and hence the experimental halls receive electron bunches once every 2 ns with a frequency of 499 MHz. The combined laser pulse first irradicates the $GaAs$ photocathode to produce electron bunches. Then these bunches are accelerated to 45 MeV by two RF cavities, then packaged by the optical chopper before being sent to the recirculating linacs of the CEBAF.

The important component of the CEBAF accelerator at JLab was the superconducting RF cavity. Figure 2.3 shows a pair of typical RF cavities. These cavities were made of niobium and were kept in a liquid helium bath at a very low temperature, 2 K, to maintain the superconductivity. Klystrons were used to set up the radio frequency standing waves in these cavities, providing the acceleration gradient for the

electron beam. The RF waves in the cavity had a frequecy of 1497 MHz, and were in phase with the beam's electron bunches so that there was always a positive electric force on an electron bunch when it crosses an RF cavity. Figure 2.4 shows how the acceleration of an electron beam bunch workes in an RF cavity. Each RF cavity had its own Klystron and control package to allow optimal tuning of the phase and the acceleration gradient.

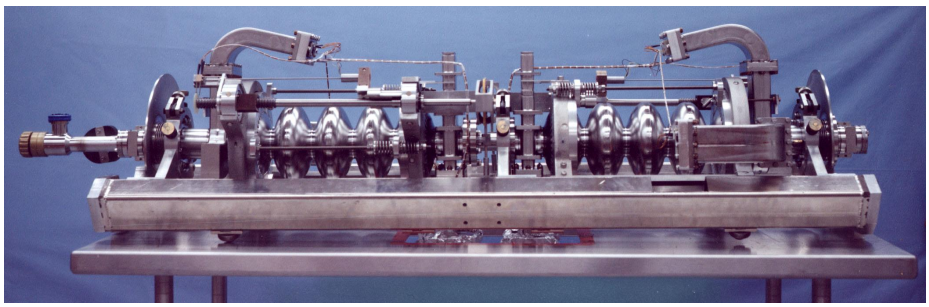

Figure 2.3: A pair of superconducting niobium RF cavities. The elliptical bulges on the innermost part of above figure are the RF cavities, were kept perpendicular to the beam line. Source [49]

The acceleration of the electrons, and hence the energy, was achieved as electrons traversed through the two linacs. These two linacs were connected by nine recirculation arcs, allowing the beam to make a total of five passes through both linacs. Figure 2.2 shows the CEBAF "racetrack" course of the accelerator. In the linac region, the electron beam achieves a 600 MeV acceleration on each pass, through 168 RF cavities, to reach a 5.71 GeV beam energy for the *g12* experiment. The beam for an experiment hall was extracted using RF seperator cavities. All the experimental halls could run at the maximum energy but no two halls could run with same energy, because the seperator only extracted a single beam energy for one hall on any given pass. The extracted beam was then directed toward the individual experimental halls, Hall A, B, and C.

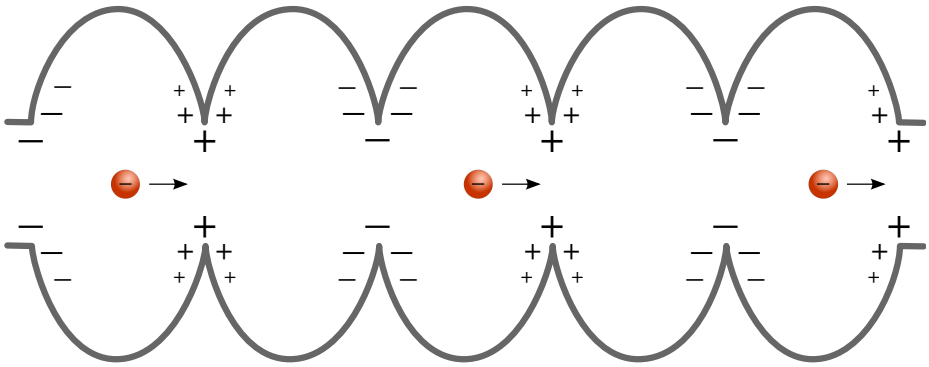

Figure 2.4: Superconducting cavities with standing RF waves. These cavities always produce a positive force because of the acceleration gradient coming from RF waves throughout the electron motion in the cavities.

2.2 Photon Tagger

A photoproduction experiment like *g12* requires a real photon beam. Since CEBAF produces an electron beam, the conversion to a photon beam is done via the *bramsstrahlung* process. The *bramsstrahlung* process happens when the electron beam passes through a gold radiator of thickness 10^{-4} radiation length. Gold is a high density metal, so when electrons are incident on the gold foil, the electrons decelerate and produce real photons in the vicinity of the electromagnetic field of nuclei. The photon beam energy depends on the amount of electron energy lost. In addition, electrons transfer their polarization to the photons. The amount of photon polarization depends on the incoming electron energy and the scattered photon energy [50] as,

$$P_\gamma = \frac{E_\gamma(E_e + \frac{E_e - E_\gamma}{3})}{E_e^2 + (E_e - E_\gamma)^2 - \frac{2}{3}(E_e - E_\gamma)} P_e. \tag{2.1}$$

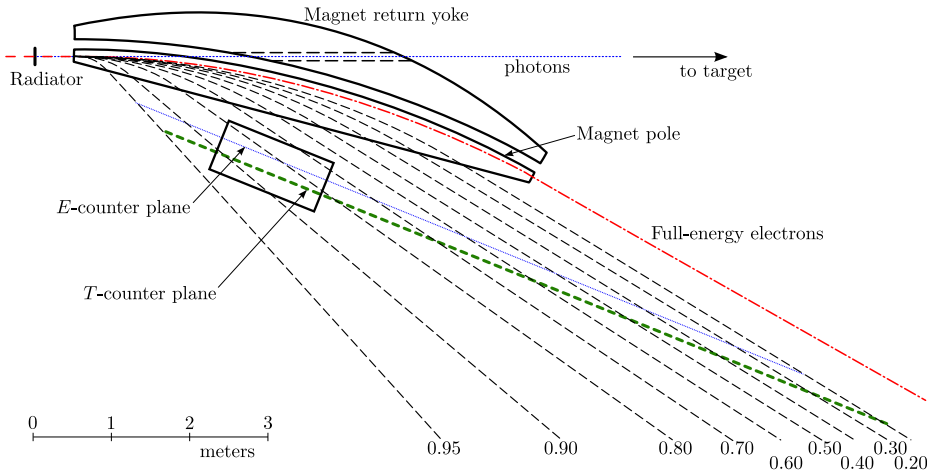

Figure 2.5: A schematic view of the Hall B tagging system. It includes a radiator from which electrons produce photons through *bremsstralung* process. After that the hodoscope and magnetic field assists in measuring the recoil electron energy, hence, the photon beam energy from energy conservation. The photon beam then pass through the collimator to hit the target at the `CLAS` center. Source [51].

After the electron beam passes through the radiator, the beam becomes a mixture of scattered electrons, *bremsstralung* photons, and the non-interacting electrons. The tagger magnet placed after the radiator sweeps the electrons out of the beam line, allowing the photon to proceed towards the `CLAS` target. The photons produced from *bremsstralung* process have an energy range determined by the incoming electron energy and the measured scattered electron energy via $E_\gamma = E_e - E_{e'}$. The scattered electron energy was measured by one of the hodoscope planes located below the tagger magnet. The magnet for the tagger system was a normal-conducting dipole magnet of strength 1.75 T. The magnetic field was tuned such that those electrons that did not interact with the radiator are deflected toward the beam dump, while the recoil electrons were bent towards the hodoscope planes.

The two planes of the hodoscopes, each made of overlapping arrays of scintillators, were the `E`-plane and the `T`-plane. The `E`-plane contains 384 scintillator paddles (`E`-counters), with a 20 cm length, a 4 mm thickness, and a width from 6 mm to 18 mm, arranged in an overlapping fashion to increase the granularity of the en-

ergy measurement. The momentum resolution from the E-counters was very narrow, about $\frac{\delta p}{p} = 1 \times 10^{-3}$. The second plane of the hodoscope, the T-plane, was designed to measure the timing information of the recoil electrons. The T-plane was made of 61 scintillator paddles (T-counters), each 2 cm thick, to accumulate sufficient light to determine the pulse-shapes accurately. The width of the paddles varied from 9 to 20 cm, so that each paddle has a uniform counting rate, despite the $\frac{1}{E_\gamma}$ dependence of the bremsstrahlung cross section. The T-counters had a timing resolution of 110 ps to match the accelerator electrons coming every 2 ns, and hence measure the timing of the induced photon that produces the physics event. The field of the tagger was set to tag photons ranging from 20% to 95% of the incident electron beam energy. Figure 2.5 shows a schematic diagram of the tagger spectrometer with some typical trajectories for the recoiling electrons corresponding to various fractional energies transferred to the outgoing photon.

Before the photon beam reaches the CLAS target, it passes through a pair of the collimators to trim the beam halo. A set of magnets were placed after the first collimator to sweep out the charged particles created during the interaction with the collimator. More details about the Hall B tagging system is in Ref. [51].

2.3 The CLAS Detector

The primary detector in experimental Hall B was the CEBAF Large Acceptance Spectrometer (CLAS) [52] detector, shaped like an onion centered around the beam line (see Figs. 2.6 and 2.7). The CLAS detector was used to track and detect the reaction products produced during the experiment. The CLAS detector had several detector subsystems, such as the start counter, the drift chambers, the time-of-flight scintillators, the Cherenkov counters, and the electromagnetic calorimeters, which were arranged in the six-sectors geometry, as shown in Figure 2.6. Not all the subsystems

of CLAS were utilized for each experiment, but depends on the type of physics under study. For the case of lepton detection (and to seperate electron-pion) in the final state, the Cherenkov counter and the electron calorimeter were useful. In the current work, the final state particles are all hadrons, which does not require these subsystems. During *g12* experiment, the CLAS target was moved upstream in order to avoid loss of high momentum charge tracks in the very forward direction where the beam passes through. More details on the detector subsystems and their properties are included in the following sections.

Figure 2.6: A photograph of the CLAS detector. This picture was with the time-of-flight detector pulled back towards left showing the six-sector view of the region 3 drift chambers. This picture was taken from the downstream direction. Source [49]

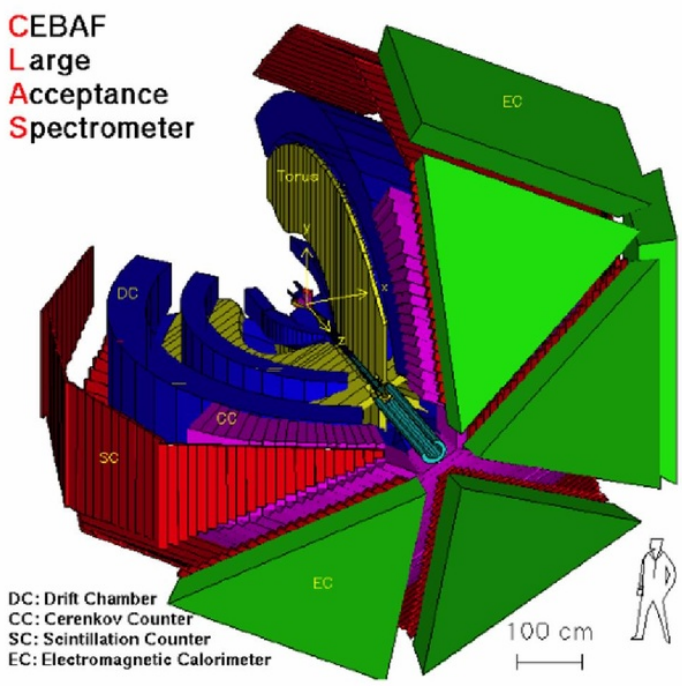

Figure 2.7: A schematic diagram of the CLAS detector system. The detector subsystems were color coded to seperate them one from another. This figure removes a sector to show all the parts of the detector. Source [49].

2.3.1 Target

There were different target materials used for the different experiments in Hall B since it started taking data in 1998. For the *g12* experiment, the target material was liquid hydrogen that was kept inside a cylindrically shaped target cell of length 40 cm and radius of 2 cm as shown in Figure 2.8. The wall of the target cell was made of aluminum, and the window of the target cell was made of Kapton. The advantage of Kapton is that it resistant to the effects of high temperature and high radiation. The position of the target was shifted upstream of the CLAS nominal center by 90 cm to increase the acceptance at small scattering angles. Thus the target was kept in the range of -110 to -70 cm relative to the nominal center of CLAS.

Figure 2.8: A schematic diagram of the target cell used during the *g12* run period. The target cell is 40 cm long. Image source: [53]

2.3.2 Start Counter

The start counter (ST) detector system was located at the inner-most region of CLAS and surrounded the target (shown in Figure 2.9). The ST was divided into six sectors, each have four scintillator paddles equipped with photomultiplier tubes (PMT) at the end [54]. The ST detector covered the polar angle range from 7° to 145°, and azimuthal angle range per sector was $-29°$ to 29°. The ST was built to measure the time when the track hit the scintillator paddle in each sector of the detector. The time measured through the ST counter had a resolution of about ≈ 350 ps, which is worse than the resolution of the RF corrected tagger time, ≈ 15 ps. Although the resolution is poor, nevertheless the ST time can still be used as the event start time because the ST was just outside the target. The event start time was later used to measure the speed of charged tracks that hit the multiple detectors during their trajectory through CLAS. Moreover, in this analysis, the ST time is paired with the RF corrected tagger time to select the right photon in the target. In addition, the ST was included in the trigger configuration with a tagger hit and a time-of-flight hit (more details about trigger is in Section 2.4).

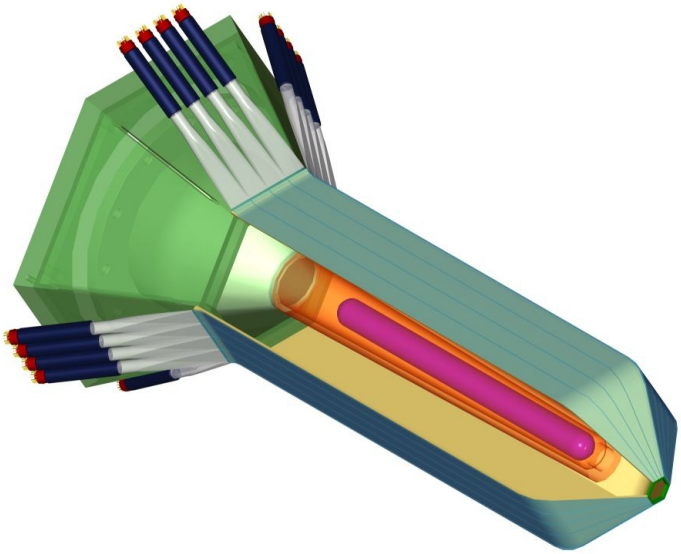

Figure 2.9: A schematic diagram of the CLAS start counter. Source [54].

2.3.3 Superconducting Toroidal Magnet

CLAS had a superconducting toroidal magnet as the heart of its magnetic spectrometer. The toroid had six superconducting coils that consisted of four layers of 54 windings of aluminum stabilized niobium-titanium NbTi/Cu superconductor [55]. The six sector geometry of the CLAS detector was defined by the torus arrangement (see Figure 2.10), where torus coils were placed at 60° intervals about the beamline. Also, the magnetic coils were located between Region 1 and Region 3 of the DC, see Fig. 2.11. The maximum field strength that could be achieved by the toroidal magnet was 35 kG, at the highest current of 3861 A. During the *g12* run period, the toroidal magnet operated at a current of 1930 A, corresponding to a maximum field of about 20 kG. Operating at almost half the maximum magnetic field strength increased the acceptance of the negatively charge particles but reduced the momentum resolution of the charged particles.

Figure 2.11 shows the field map in the presence of a 20 kG field. The magnetic field was primarily directed along the azimulthal direction, which causes charged

particles to bend in the polar angle. Using the charged particle track curvature in the presence of magnetic field, the momentum of a charged particle can be determined as,

$$p_{\perp} = qrB \tag{2.2}$$

Figure 2.10: Photograph of the CLAS Superconducting Toroidal Magnet. Source [56].

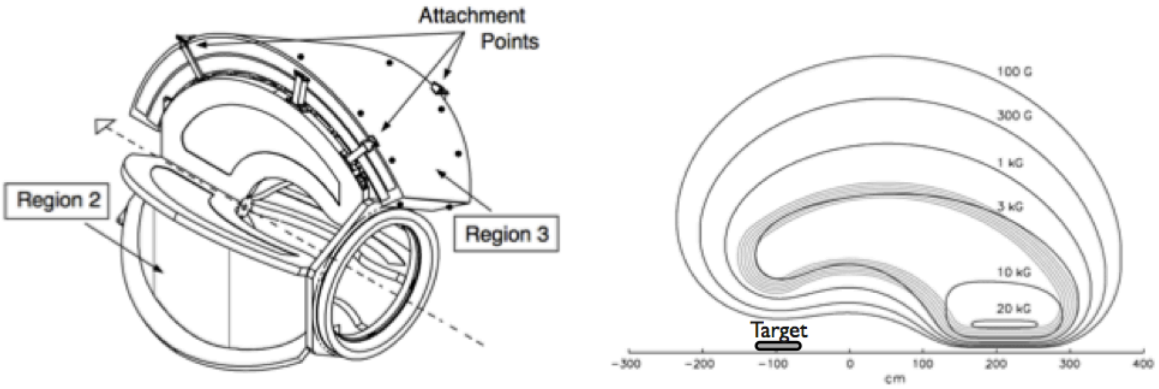

Figure 2.11: (Left) Superconducting Toroidal Magnet and its position in relation with DC Region 1 and Region 3. (Right) Magnetic field map for a torus current of 1930 A, corresponding to maximum field strenght of 20 kG. Source [55].

2.3.4 Drift Chambers

CLAS has drift chamber (DC) detectors behind the start counter and before the Time-of-flight detectors. The DC detector system includes three regions: Region 1, Region 2, and Region 3 as shown in Figure 2.12. Region 1 lies between the start counter and the inner part of the toroidal magnet. Region 2 is situated in between the superconducting coils shown by the dotted line in Figure 2.12. Region 2 is exposed to the strong magnetic field and is used to determine the particle curvature, and hence the momentum of the particle. Lastly, the outermost part of the DC system is Region 3, which resides outside of the toroidal magnet. The magnetic field strength in Region 1 and Region 3 is negligible in comparison to Region 2.

Each region of the DC is further divided into six sectors for a total of 18 drift chambers. Each drift chamber is composed of two superlayers. Each of the superlayers had sense wires and field wires. The field wires were 140 μm gold plated aluminum alloy that defined a hexagonal configuration with a gold plated 20 μm thick sense wire at the center. In the first superlayer, the wires were oriented axially to the magnetic field direction while the second *superlayer* had wires tilted at a 6° stereo angle. Six hexagonal cells were structured on each *superlayer* where the separation between each cell is half the cell width. The DC was filled with a mixture of 90% argon and 10% carbon-dioxide gas.

During operation, the sense wires were kept at positive potential whereas field wires were at a negative high voltage, resulting in a high potential difference between the wires. A particle track that passes through the gas inside the DC produces ionization with electrons drifting towards the sense wire because of the high potential different between sense wires and field wires. This process produced an electrical pulse that was then processed with preamplifiers and discriminators before being recorded

by the time-to-digital-converters (TDC). More details about the CLAS drift chamber systems' design, fabrication, and testing are in Ref. [57].

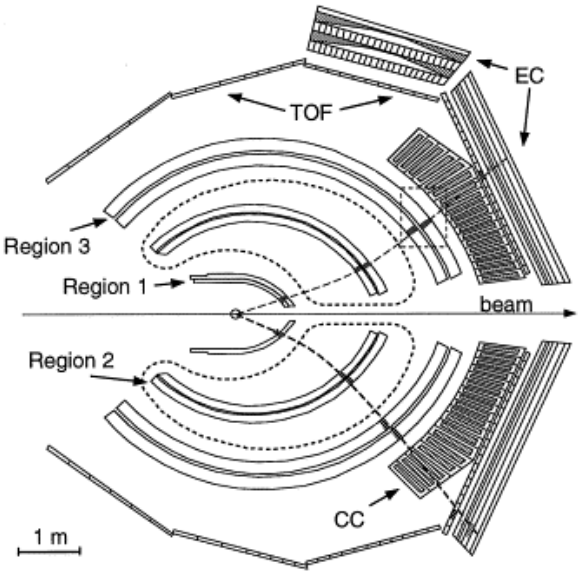

Figure 2.12: Horizontal cut through the CLAS detector at the beam line. The two dashed lines originated from center of target show charged particles traversing the drift chambers of opposite sectors. The dotted lines show the location of torus magnets. Image source [57]

2.3.5 Time-of-flight Scintillators

Outside the Region 3 DC a wall of scintillator exists, known as the time-of-flight detector (TOF). It is about 4 m away from the CLAS target and had six sectors. In each sector there were four panels and a total of 57 bars (TOF-counters). Each counter had a thickness of 2 inches to allow 100% detection of the charged particles and had variable length and width based on the angular coverage. In the forward-region where the scattering angle is less than 45° the counters had a width of 15 cm and a length that ranged 32cm to 276 cm, while at the large-angle region the counters had a width of 22 cm and a length that ranged from 271 cm to 445 cm. These panels were arranged in such a way that they faced the beam line as shown in Figure 2.13. Each counter had a pair of PMTs on both sides to collect the signals of the track hit and to get the timing

information. The timing resolution of the TOF detector was 80-160 ps depending on the length of the counters. For this analysis, the TOF detector is a vital component that was added to the first level trigger of the *g12* experiment. Moreover, the timing information from the TOF was used for particle identification of the charged hadrons in the final state. More details about the TOF system, calibration, and reconstruction are in [58].

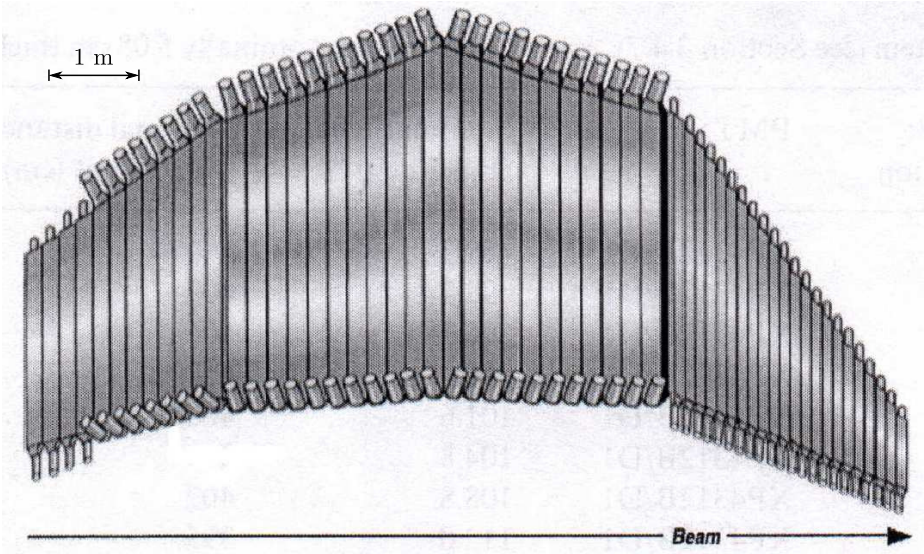

Figure 2.13: Schematic of Time of flight detector. Source [58]

2.3.6 Cherenkov Counter

The Cherenkov Counter (CC) was in between the Region 3 DC and the TOF detector in the forward region covering polar angles of 8° to 45° in each detector. This angular coverage was only true if the target was at the CLAS center. For the *g12* experiment, the target was placed 90 cm upstream to the CLAS center, because of this, the angular coverage changes to approximately 6° to 35° in the lab frame.

The Cherenkov counter works by producing light when a particle passes through the medium with a velocity larger than the speed of light. The velocity of the particle in the medium is given by $v = \frac{c}{n}$, where n is the refractive index of the medium and

c is the velocity of light. The gas used in the CC was C_4F_{10} (*perfluorobutane*) with an index of refraction 1.00153. The produced Cherenkov light then reflected into an array of PMTs using mirrors as shown in Figure 2.14. The CLAS CC is used to separate leptons from pions of momentum less than 2.5 GeV. The threshold for charged kaons and protons is much higher than the maximum beam energy for *g12*; therefore this detector does not detect those particles. Because we don't need electron/pion seperation in the current work, we are not including any information from the CC in this analysis. More detail about the CC is found in [59].

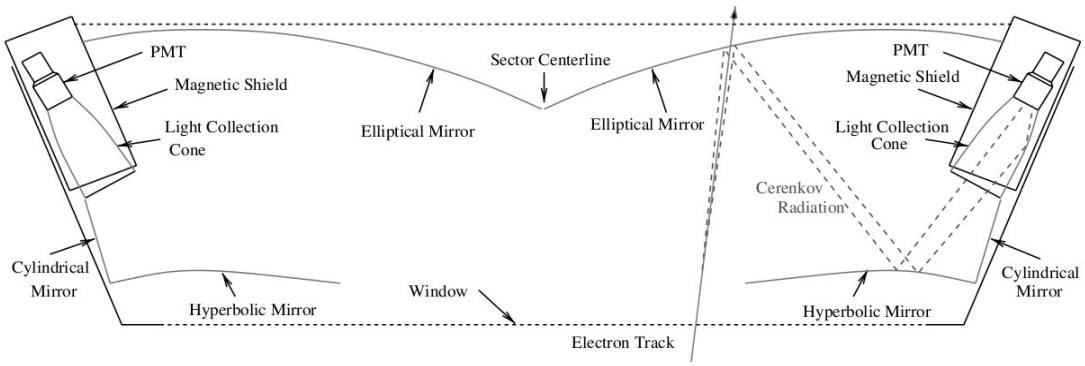

Figure 2.14: Segmented view of CC, where it shows the reflection of Cherenkov light from different mirrors after it was produced. Source [59]

2.3.7 Electromagnetic Calorimeter

The last detector system of CLAS was located at the outer edge; it covered most of the forward region and is called the electromagnetic calorimeter (EC), and is shown in Figure 2.15. This calorimeter had importance primarily for physics analyses that have leptons in the final states, where it was used to separate high momentum electrons from pions, or when detection of neutral particles (n, γ) is needed.

The arrangement of the EC detector system also matches the geometry of the rest of CLAS, consisting of six sectors. Each sector had triangular shaped EC modules made by multiple layers of Pb (absorber) and scintillators (detector) placed alternatively. A

layer was made by the 10-mm-thick BC412 scintillator and 2.2-mm-thick lead. Each module had three different views set by the scintillator arrangement; u, v, and w. In total 216 PMTs were needed per module, and therefore 1296 PMTs in total. Fig. 2.15 shows the different views of EC system.

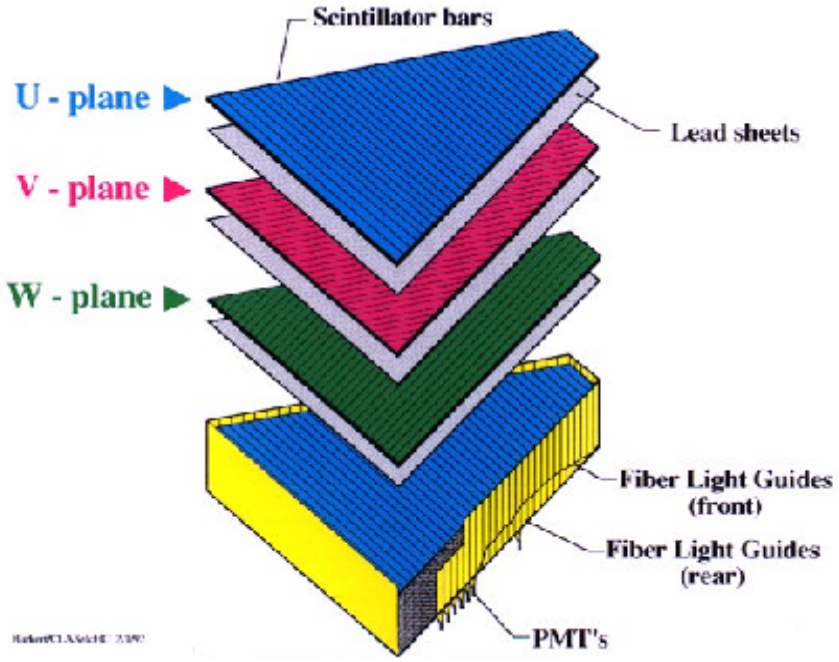

Figure 2.15: Seperated view of one sector of the forward EC showing the three planes (u,v, w) of scintillator-lead pairs that make up one of the 13 logical layers. Source [60].

2.4 Triggering and Data Acquisition

As described in the previous sections, CLAS was comprised of multiple detector subsystem. Each of these subsystems included its own electronic package to collect signals. The signals from a detector system was only digitized when it crossed a preset threshold for the corresponding subsystem. The signals from detectors are recorded after being digitized. The signal digitization was primarly done by two types of hardware, Time-to-digital converters (TDCs) and Analog-to-digital converters (ADCs). TDCs are

for reporting the time at which a signal arrives, while an ADC's job is to report a number corresponding to the signal size.

The output of the TDCs and the ADCs were then triggered to verify that the event was of interest or not. The trigger is a combination of signals from various subsystems required for an event to be written out to disk. An item in the trigger list is known as trigger "bit". For the first time, the *g12* run used a field programmable gate array (FPGA) logic processor as the trigger supervisor to collect the data. The FPGA allowed for 12 independent trigger configurations to be employed at one time, as well as the ability to change the trigger configuration during the running.

There were two levels of triggering during the *g12* run period; level-1 (L1) and level-2 (L2). The detector subsystem used by the level-1 (L1) triggering system are TAGR (Section 2.2), ST (Section 2.3.2), CC (Section 2.3.6), TOF (Section 2.3.5), and EC(Section 2.3.7). Figure 2.16 shows a level-1 trigger using different detector system except TAGR. For each sector, the trigger requires a coincidence between a hit in either of four paddle of ST with a hit in any of 57 TOF paddles. This trigger set is represented as ST$\times$TOF and is called a prong. The hardware and configuration does not allow for two signals from the same sector of TOF because there are only six signals recorded, one from each sector. The coincidence of a single "prong" with photon tagger hit, called "Master-OR" (MOR), is given in the table below. A more detailed explanation on the trigger configurations and efficiences can be found in References [61, 62].

When a first level trigger requirement is satisfied, a second-level (L2) trigger is required in addition to the L1 trigger. A L2 trigger is usually a software routine and is always slower than L1 trigger. Specifically the second level trigger requires a valid track to be verified in the DC.

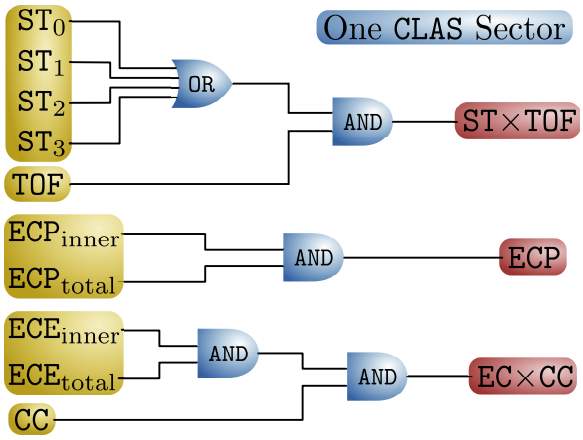

Figure 2.16: Level 1 trigger logic for one of the six sectors of CLAS. The ST×TOF signal is a coincidence between any of the four start counter TDC signals (numbered from 0 to 3) and any of the 57 TOF TDC signals. The $\mathrm{ECE}_{\mathrm{inner}}$ and $\mathrm{ECE}_{\mathrm{total}}$ are the *electron*-threshold EC signals for the energy deposited in the *inner* layer and in *all* layers. These are combined with a CC signal to produce the EC×CC trigger for this sector. The ECP trigger signal is the *photon*-threshold EC signal. Source [61]

Table 2.1: Trigger configuration as a coincidence between a start counter and time-of-flight hit in the i^{th} sector or any sector, symbolized as $(\mathrm{ST}\times\mathrm{TOF})_i$. The (ST×TOF) is called a *prong*. An added ×2 or ×3 indicates the coincidence of multiple *prongs* that are not in the same sector. MORA and MORB represent coincidences with tagger hits.

g12 runs 56363–56594, 56608–56647			
bit	definition	L2 multiplicity	prescale
1	MORA·$(\mathrm{ST}\times\mathrm{TOF})_1$·(ST×TOF)	–	1
2	MORA·$(\mathrm{ST}\times\mathrm{TOF})_2$·(ST×TOF)	–	1
3	MORA·$(\mathrm{ST}\times\mathrm{TOF})_3$·(ST×TOF)	–	1
4	MORA·$(\mathrm{ST}\times\mathrm{TOF})_4$·(ST×TOF)	–	1
5	MORA·$(\mathrm{ST}\times\mathrm{TOF})_5$·(ST×TOF)	–	1
6	MORA·$(\mathrm{ST}\times\mathrm{TOF})_6$·(ST×TOF)	–	1
7	ST×TOF	–	1
8	MORA·(ST×TOF)×2	–	1
11[a]	MORB·(ST×TOF)×2	–	1
12	(ST×TOF)×3	–	1

[a]bit 11 and MORB were included in the trigger starting with run 56519.

If all the trigger condition are satisfied then the detector information for a event is recorded to the magnetic tape after passing through the "event builder" via CAMAC [55], for future offline analysis. At the time *g12* was run, the DAQ was capable of running at 8 kHz.

2.5 Event Reconstruction

The process of converting the raw data in the form of ADC and TDC information to the physics analysis data, such as the particles' four vector, is called reconstruction. The tracks were reconstructed using hit-based and time-based tracking algorithms. The hit-based tracking algorithm looks for a hit in the drift chamber sense wires of each superlayer. It then creates track segment in each region of DC. A track that aligned in physically allowable curve of the superlayer is assigned as one candidate of the track. Track information is refined by time based tracking. The time information were taken from the TOF hit are used to correct the drift times inside the DC, which are then coverted to drift distances. The track segment is then corrected for each superlayer and a new track is found. The process of correction is done recursively until a physically possible alignment is not achieved.

After a track segment is determined, the length of the curvature of the track (l) is used to determine the momentum of the track using

$$p = \frac{\ell^2 qB}{8s}, \tag{2.3}$$

where s is the sagitta length and is calculated as depicted in Figure 2.17, B is the magnetic field strength, and q is the charge of the particle.

The final procedure of reconstruction is to assign a mass to the particle track. The particle mass is calculated using time infromation from ST and TOF, as well as

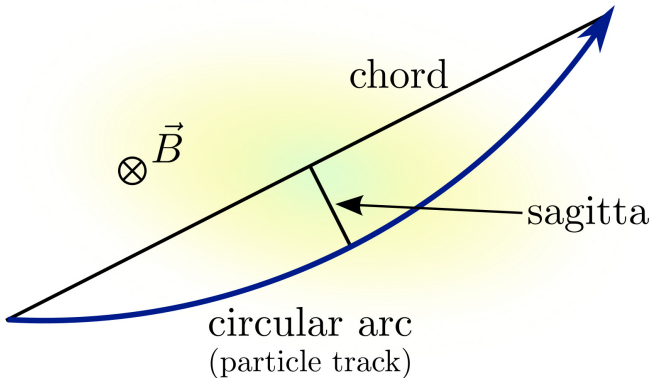

Figure 2.17: The sagitta of a circular arc is the maximum distance between the arc and a given chord. Since charged particles traveling perpendicular to a uniform magnetic field trace a circular path, this is used as an approximation for determining the maximum error of the measured momentum. Shown here is a positively charged particle moving through a uniform magnetic field ($\vec{B}$) going into the page.

the total path length of the trajectory. With all this information, the velocity of the particle is calculated using,

$$\beta = \frac{l_{sc}}{t * c}, \tag{2.4}$$

where c is the speed of light.

Using the momentum (p) and velocity (β) information calculated above, the mass of the particle is given by,

$$m = \frac{p\sqrt{(1-\beta^2)}}{\beta}. \tag{2.5}$$

Once the mass has been determined, particles are given an identification number. This process is called particle identification (`PID`). The criteria used for `PID` are,

$$\texttt{PID} = \begin{cases} \pi^{\pm}, \text{ if } m < 0.3 \text{ GeV and } q^{\pm} \\ K^{\pm}, \text{ if } 0.35 < m < 0.65 \text{ GeV and } q^{\pm} \\ p^{\pm}, \text{ if } 0.8 < m < 1.2 \text{ GeV and } q^{\pm} \\ d, \text{ if } 1.75 < m < 2.2 \text{ GeV} \end{cases} \tag{2.6}$$

Particles that do not fall into the criteria above are considered as *unknown* particles. After the particle identification was completed, all the relevant information about those particles were collected for the event of interest and saved in the bos format. The saved bos files are useful for further physics analysis after passing through a user analyzer. The user analyzers are different for different physics purposes. In the current work, the analyzer was set to select the final state particles; K^+, proton, and π^-.

CHAPTER 3

EVENT SELECTION

The *g12* experiment collected more than 128 TB of raw data, which consists of 26 billion events with an integrated luminosity of 68 pb^{-1}. The *g12* experiment is the largest meson photoproduction experiment and was done using a circularly polarized photon beam incident on an unpolarized liquid hydrogen target. For this experiment, the photon beam energies ranges from 1.1 to 5.45 GeV. More details about the *g12* experiment's running conditions, data acquisition, and triggering is in Ref. [61]. Table 3.1 shows the general running conditions of the *g12* experiment.

Table 3.1: Running conditions for *g12*

Electron Beam Energy	5.714 GeV
Electron Beam Current	60-65 nA (production) & 24 nA(single-prong)
Photon Beam Polarization	Circular
Radiator Material/Density	Au / 646 μg/cm^2
Radiator Thickness	$10^{-4}\chi_0$
Radius of Photon collimator	6.4 mm
Photon Beam Energy Range	1.142-5.425 GeV
Target Shell Material	Kapton
Target Length/Diameter	40 cm/4 cm
Target Material	ℓH_2
Target Position	-90 cm from `CLAS` center
Target Polarization	None
Torus Magnetic Current	$\frac{1}{2}B_{max}$ = 1930 A

3.1 Reaction Channel and topologies

In the current work, we analyzed the photoproduction of the Λ hyperon through the channel

$$\gamma p \rightarrow K^{+}\Lambda. \tag{3.1}$$

The Λ decays through the weak process into two decay modes, $p\pi^{-}$ with a 64% branching ratio and $n\pi^{0}$ with a 36% branching ratio. The `CLAS` detector had low efficiency for the detection of neutral particles, so, the current work only includes the charged-particle decay mode, $p\pi^{-}$. With $p\pi^{-}$, the final state particles are K^{+}, p, and π^{-}. It is possible that all of the charged particles in our analysis, K^{+}, p, and π^{-} could be detected. However, the negatively charged particles in `CLAS` were bent toward the beam line, where the `CLAS` detector had hole, in the presence of nominal polarity for the toroidal magnetic field. Because of low acceptance for π^{-}, its detection reduced the $K^{+}p\pi^{-}$ events heavily. To address this issue, we include two topologies in our analysis.

- "three-track": $\gamma p \rightarrow K^{+}p\pi^{-}$, where all three charged particles are detected by `CLAS`.
- "two-track": $\gamma p \rightarrow K^{+}p(\pi^{-})$, where only K^{+} and proton are detected. The missing π^{-} particle is later reconstructed using the missing mass technique.

The missing mass technique that we used for π^{-} is based on energy-momentum conservation that uses the four vectors of the incoming beam and the target, which is then subtracted from the four vectors of the K^{+} and p. In general a four vector is the composite representation for a particle's three-momentum and energy. The missing

four-vector is given by

$$P_x = P_\gamma + P_{target} - P_{K^+} - P_p, \tag{3.2}$$

where P_x, P_γ, P_{target}, P_{K^+}, and P_p are the four-vector's for the missing particle, the incoming photon, the target, the detected K^+, and proton, respectively. The missing four vector for π^- in our analysis is later calculated using the missing momentum components from P_x and the known mass for $\pi^- = 0.13957$ GeV.

3.2 Event Filters

For the *g12* experiment, the first level triggering for a charged particle was set up as a coincidence between a hit in any sector of `TOF` with one `ST` hit in the same sector. More detail about triggering is in Section 2.4. The trigger allowed recording of a large variety of particles along with the particles of interest for this analysis. The large data set was then skimmed for events with at least two charged tracks, one of which is K^+. A K^+ was tentatively identified in the skim based upon the `PART` bank idenfication or if the `PART` bank identified the particle as a high momentum π^+ (> 2 GeV) or a high momentum proton (> 3 GeV). This was done because of poor particle ID at high momenta.

Figure 3.1 shows the missing mass off the K^+ before any additional selection criteria were applied. There are many events of mass higher than that of Λ (1115.57 MeV). Two filters were used in the analyzer to reduce the file sizes to a reasonable value for both topologies. The criteria were: the missing mass off $K^+ < 1400$ MeV and the missing mass squared off $K^+p < 300$ MeV^2. These filters reduce the number of background events. During this analysis, we will check the

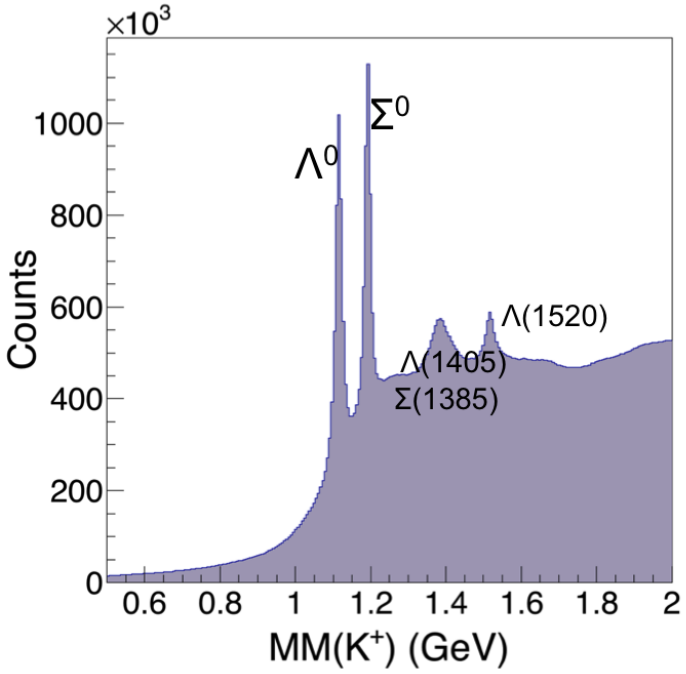

Figure 3.1: Missing mass of K^+ before applying any cuts.

effectiveness of selection cuts on total data from the missing mass distribution of K^+, calculated as,

$$MM_{K^+} = \sqrt{(P_\gamma + P_{target} - P_{K^+})^2} \tag{3.3}$$

Figure 3.1 shows the missing mass distribution before any cuts, where we have a large peak for Λ. In addition, we have other hyperons with decay channel of K^+Y, and Y referred to Σ^0, $\Lambda(1405)$, $\Lambda(1520$ and so on. The following sections will elaborate all the cuts that were applied to remove the background in the $K^+\Lambda$ events.

3.3 Vertex timing selection

The `CLAS` detector has multiple timing-measurement subsystems that provide the particle's hit time in the corresponding detectors. The most important detector sys-

tems (to this analysis) that provide timing information, are the tagger (TAGR), the start counter (ST), and the time-of-flight (TOF). Besides those subsystems, there are other subsystems of CLAS that provide the timing information about the particle hit such as the drift chamber (DC), the Cherekov counter (CC), etc. The time measured in the ST, TAGR, and TOF can be reconstructed to the CLAS target in order to get the event's start time. Since the start counter is the closest detector to the target, it was used to select the right photon incident on the target.

To achieve the most precise arrival time of the photon at the event vertex, the RF-corrected tagger time was choosen. The RF time serves as the most precise timing measurement available with a resolution of approximately 15 ps. The RF correction to the tagger time was made after choosing the right photon bunch. The RF-corrected vertex time from the tagger is

$$t_{vtx}(TAG_{RF}) = t_{TAG,RF} + t_{prop}, \tag{3.4}$$

where $t_{TAG,RF}$ is the RF-corrected time that crossed the center of the target, and t_{prop} is the propagation time from the center of the target to the track's vertex z-coordinate.

Figure 3.2 shows the events within one nanosecond agreement between the event-vertex time as calculated by the RF-corrected tagger and the start counter.

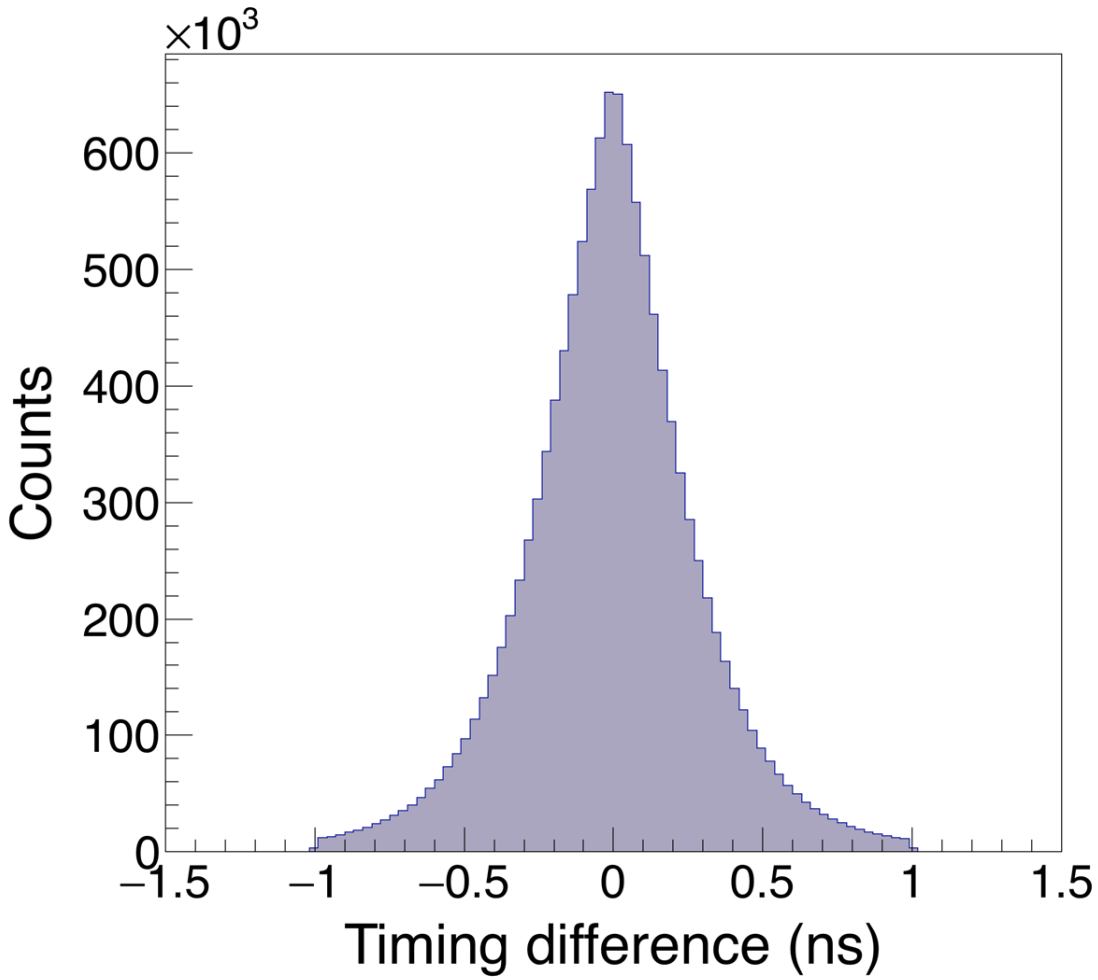

Figure 3.2: Time difference between the start counter vertex time and the RF-corrected tagger time. Events are selected within ±1 ns.

3.4 Vertex position cut

The cylindrical target for the *g12* experiment had a radius of 2 cm and a length of 40 cm, and was positioned upstream of the `CLAS` center from -110 cm to -70 cm. The best estimate of where an event happened for the aforementioned reaction was the distance of closest approach to the beam line of the reconstructed tracks of the final-state particles. The detailed studies about the track reconstruction and event vertex determination are explained in Ref. [42]. For this analysis we are getting the event

vertex information from the MVRT bank of the CLAS software. In our analysis, a good event is considered when the reconstructed vertex position along the longitudinal direction resides within 5 cm of the target ends from -110 to -65 cm. The ranges assigned for the vertex selection are larger than the actual target dimension. It is important to includes events outside a target dimension since the finite lifetime of Λ could lead to a decay in that region.

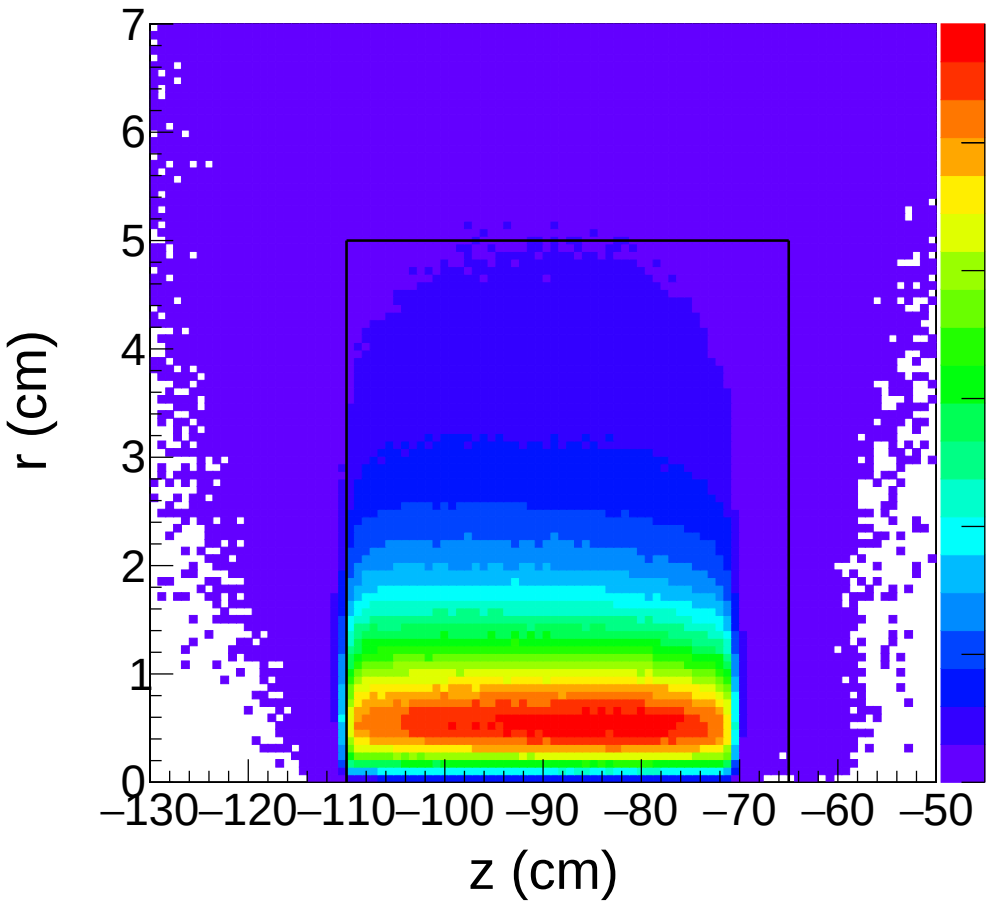

Figure 3.3: Event distribution in the *g12* target. Selected events are within the rectangular box drawn by a dark line.

3.5 Multiple photons

The production runs we are using have a beam current of 60–65 nA. With this beam current there is a high probability that multiple photons were produced and tagged. If the timing difference between tagger hits and other detector components, such as the start counter, is greater than ± 1 ns, the timing cut is sufficient to remove multiple-photons events. But if the photons coincide within 2.004 ns, then they cannot be differentiated with the timing cut. In the case where multiple photons were tagged for an event, several algorithms to select the correct photon for the event were considered: choose a photon at random, choose the more energetic photon, or eliminate events with multiple tagged photons. For this analysis, events with multiple tagged photons were removed. Figure 3.4 shows the distribution of the number of tagged photons for all events. The selection of a single tagged photon events reduce the total $K^+\Lambda$ events by 10%.

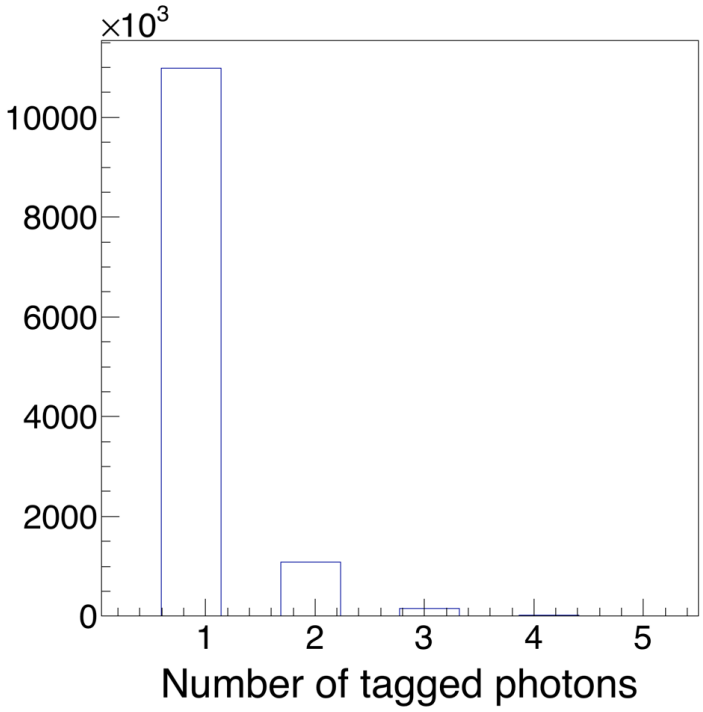

Figure 3.4: Number of tagged photons for events within the ±1 ns vertex timing cut.

3.6 Geometric Fiducial Cuts

Geometrical fiducial cuts are used to exclude events in regions where the acceptance is not well understood, in particular the region near the sector edge occupied by the toroidal magnet coils. The geometrical fiducial cut analysis was performed by Jason Bono of the `FIU` group. The cuts were produced by checking the acceptance along the azimuthal direction on each `CLAS` sector as a function of particle momentum, charge, and the polar angle. There are three options to implement this cut: *loose*, *nominal*, and *tight*. These options refer to the amount of area to be cut between sectors. In the current work we applied the *nominal* fiducial cut. The effect of the *nominal* fiducial cut in the geometric distribution for K^+ and proton are shown in Figure 3.5. The tight and loose cuts correspond to a 4° reduction and increase, respectively, in the azimulthal angle, ϕ. More details about the this cut can be found in Ref. [63].

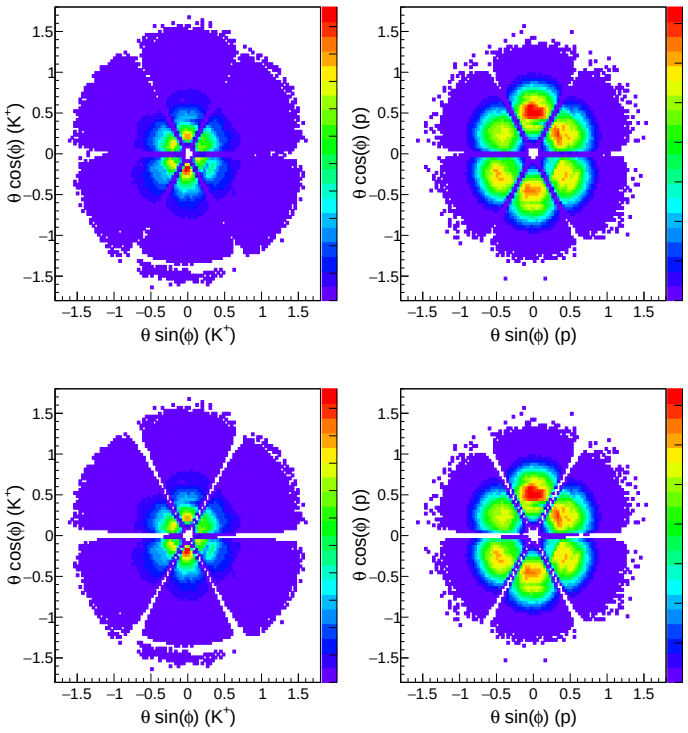

Figure 3.5: Effect of *nominal* fiducial cuts on K^+ and proton acceptances. Top panels shows the K^+ (left) and proton (right) distributions before fiducial cuts while the bottom panels shows the same distributions after fiducial cuts.

3.7 Time of flight paddles knockout

Inefficient time-of-flight (`TOF`) scintillator paddles were removed from this analysis. The efficiency of a `TOF` paddle was estimated by comparing the relative occupancy of it with counterparts in other sectors. For a paddle, say x in sector y, the efficiency is the ratio of number of hits to the average hits of the remaining three paddles. Three out of five paddles from five different sectors were choosen to calculate the average occupancy value, avoiding those with the largest and the smallest occupancies. Details can be found in Ref. [64]. The list of the omitted paddles is in Table 3.2.

Table 3.2: List of removed paddles.

Sector 1:	6, 35, 40, 41, 50, 56
Sector 2:	2, 8, 34, 35, 41, 44, 50, 54, 56
Sector 3:	11, 35, 40, 41, 56
Sector 4:	41, 48
Sector 5:	48
Sector 6:	1, 5, 33, 56

3.8 G12 Corrections

3.8.1 Beam Energy

During the calibration process it was found that the computed missing masses were systematically low. Further investigation confirmed that the low missing masses are dependent on the run numbers and vary up to 10 MeV [62]. Two reactions, the exclusive photoproduction of $p\pi^+\pi^-$ and the semi-inclusive photoproduction of $p\pi^+\pi^-(n)$ were choosed to understand and correct this problem. The study confirmed the problem was not from an "energy loss" but was from an inaccurate determination of the photon beam energy. After regorous investigation, it was found that the *g12* missing mass fluctuation was due to tagger magnet hysteresis. Magnetic hysteresis is the phenomenon that multiple distinct magnetic field strengths are possible for a given current. Hysteresis occurs in a ferromagnetic material in which the relation between the magnetic induction $\vec{B}$ and the magnetic field $\vec{H}$ is nonlinear. This affects the trajectory of the scattered electron from the bremsstralung process and, ultimately the energy measured for a tagged photon. The correction for this effect was derived in Ref. [62] and its relative size is $\frac{\Delta E_\gamma}{E_\gamma} \approx 10^{-3}$. Figure 3.6 shows the effect of *g12* beam energy correction.

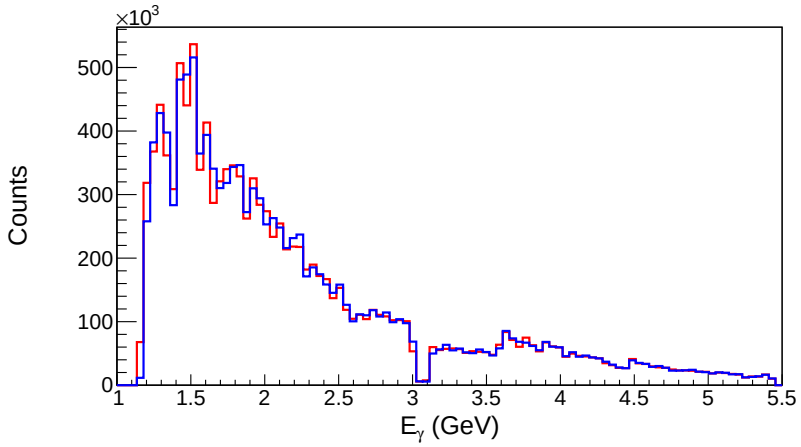

Figure 3.6: Photon beam energy (E_γ) before (red) and after (blue) correction.

3.8.2 Energy Loss

A particle loses energy when it tranverses through different materials along its path before it reaches the DC in the CLAS detector. The possible components where energy loss could occur are in the target material and walls, the beam pipe, the start counter, the air gap between the start counter and the inner region of the drift chamber, and so on. Therefore, the momenta measured by the region 2 drift chambers is not the original momentum of the particle. These momenta were corrected based on the particle track and material through which it passed. For CLAS analyses, these corrections are handled using the *eloss* package, written by Eugene Pasyuk [65].

3.8.3 Momentum Correction

The magnetic field map was calculated based on several approximations, which ended up having discrepencies with the actual magnetic field. Thus, the momentum was measured by the reconstructed particle tracks using a magnetic field value that was not accurate. The momentum correction for the *g12* run period was derived using the reaction $\gamma p \to p\pi^+\pi^-$. The beam energy and energy-loss corrected final state

particle momenta show a systematic shift as a function of azimulthal angle for each of $p\pi^+\pi^-$. The plots in Figure 3.7 show the effect of the momentum correction in the "transverse momentum balance" plots. The transverse momentum balance in $p\pi^+\pi^-$ for p is defined as the sum of the momentum of the π^+ and π^- projected onto the line that is perpendicular to the beam, keeping the same ϕ angle range. More details about the *g12* momentum correction is in Ref. [64].

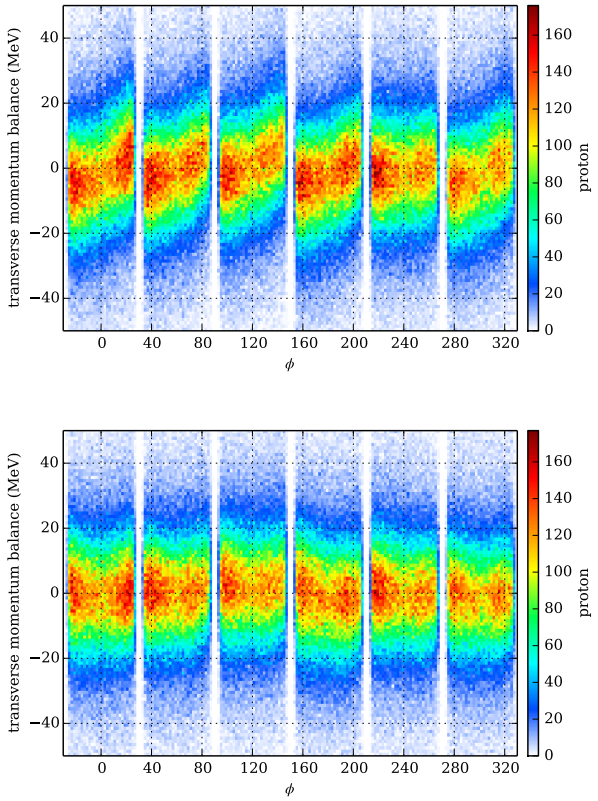

Figure 3.7: Tansverse momentum balance of $p\pi^+\pi^-$ as a function of azimulthal angle (ϕ) for the proton. (left) Before momentum correction and (right) after momentum correction. Source [64]

Figure 3.8 shows the total effect on the missing mass distribution from all the corrections described here. Events that are considered in this comparison are from the three-track topology that passed a 1% confidence level cut (described in next section). The effect on missing mass distribution is minimal. The distribution's mean shifted,

and the width after correction was reduced. However, the correction does not have dramatic effect on the overall distribution.

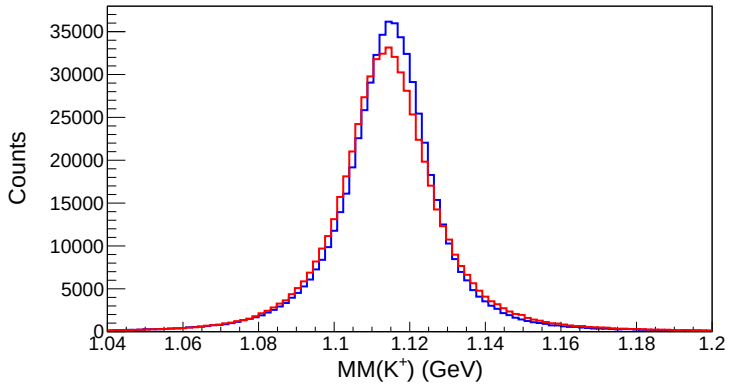

Figure 3.8: Effects of all the *g12* corrections on the missing mass. red is before correction and blue is after corrections.

3.9 Kinematic Fitting

The missing mass distribution from the two-track topology, with all the above cuts and corrections, is shown in Figure 3.9. We have $K^+\Lambda$ events along with $K^+\Sigma^\circ$ events. Since the current work is only devoted to the $K^+\Lambda$ analysis, the $K^+\Sigma^\circ$ events are considered as background. There is also a background from misidentified particles, mostly π^+ identified as K^+, that forms a continuous background under both the Λ and Σ°. So far, we do not have any cut that separates the $K^+\Lambda$ from the $K^+\Sigma^\circ$ background. In this section, we describe the kinematic fitting procedure that was used to filtered out such unwanted background from the $K^+\Lambda$ signals. Kinematic fitting is a process that used the measured quantity (energy and momentum) of the charged tracks and imposed kinematic constraints on those measured quantities in order to improve their accuracy.

For kinematic fitting, we first need to set up a hypothesis for the physics process. For example, when we have three charged tracks K^+, proton, and π^- detected in

the final state for the $K^+\Lambda$ process, then the hypothesis is *nothing missing*. The nothing missing condition is satisfied using conservation of energy and momentum for a reaction process $\gamma p \rightarrow K^+ p\pi^-$. The total energy and momentum vector are then considered constraints along with the vertex position to improve the measured quantities. The measured quantity can also be expressed as,

$$\vec{\eta_i} = \vec{y_f} + \vec{\epsilon}, \tag{3.5}$$

where $\vec{y_f}$ is a set of n measured variables, $\vec{\eta_i}$ are the true values for those variables, and $\vec{\epsilon}$ are the deviations needed to shift the observed values. The idea is now to estimate $\vec{y_i}$ from $\vec{\eta}$. In the case of $\gamma p \rightarrow K^+ p(\pi^-)$, the missing π^- hypothesis has a π^- mass constraint, and is known as the single constraint (1-C) fit. On the other hand, $K^+ p\pi^-$ has nothing missing and requires a set of constraints for momentum and energy, which is known as the four constraint (4-C) fit.

During track reconstruction, the track covariance matrix (C_η) was calculated taking into account resolution uncertainities. The fitting process started by taking the initial measured values, and the minimization required for $\vec{\delta_i} = \vec{y_f} - \vec{y_i}$ in multiple iterations using the covariance matrix, $\vec{\delta^T} C_\eta^{-1} \vec{\delta}$. Lagrange multipliers were used to handled the constraints and minimization was done using a least-squares fitting technique. A detailed description about kinematic fitting is found in Refs. [66, 67]. The kinematic fitter used in *g12* analyses was written by Dustin Keller [66]. The performance of the fit was measured using a confidence level distribution. The corresponding confidence value was defined as,

$$CL = \int_{\chi^2}^{\infty} f(x;n)dx, \tag{3.6}$$

where $f(x;n)$ is the χ^2 distribution function for n degrees of freedom. It denoted the probability distribution function for certain external constraints. In the ideal case such as where all events satisfied the fit hypothesis, the confidence level distribution would be flat from (0,1).

Figure 3.10 shows the confidence level distribution for two-track (left) and three-track (right) events. We see that these distributions for signal events are resonably flat. This is a good indicator that the kinematic fits are working properly for both channels. For the "two-track" and "three-track" events, the "good event" selection is greater than 5% and 1% respectively. The 5% confidence level cut is extremely effective for background removal from two-track analysis as shown in Figure 3.11. Moreover, the removed events with a confidence level less than 5%, are dominated mainly by $K^+\Sigma^\circ$ signals as shown in Figure 3.12.

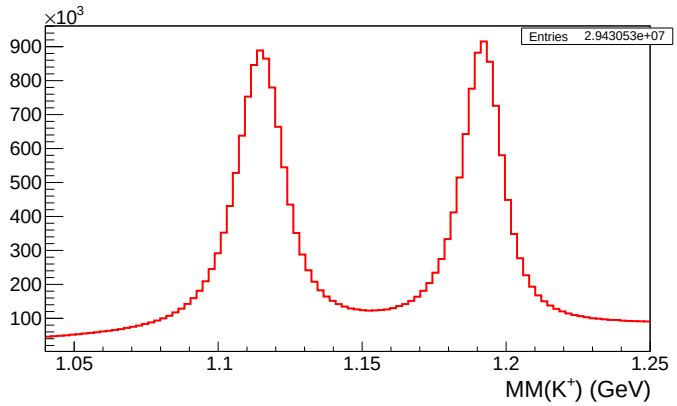

Figure 3.9: Missing mass off K^+ before kinematic fitting (all the previous cuts and corrections were implemented).

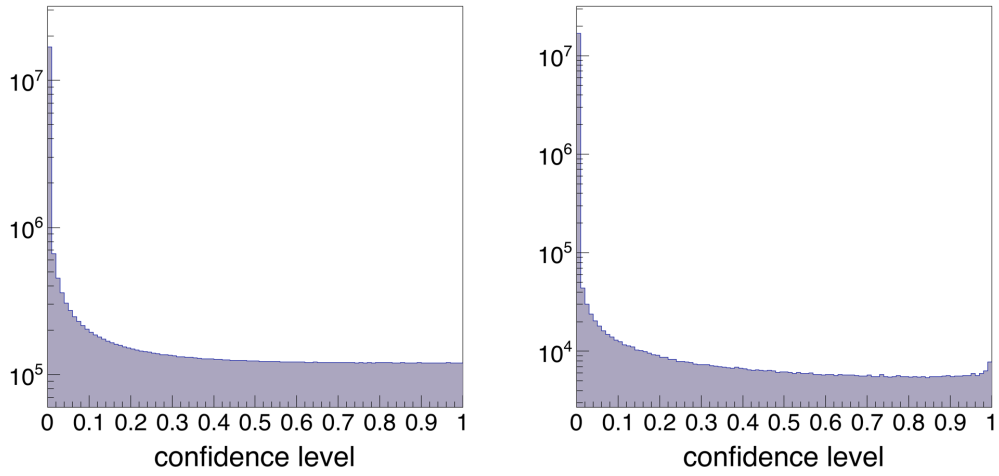

Figure 3.10: Kinematic fitting confidence level distributions for all the events. (a) Kinematic fit to $\gamma p \to K^+ p(\pi^-)$ – the distribution is fairly flat above 0.2. (b) Kinematic fit to $\gamma p \to K^+ p\pi^-$ – the distribution is fairly flat above 0.3.

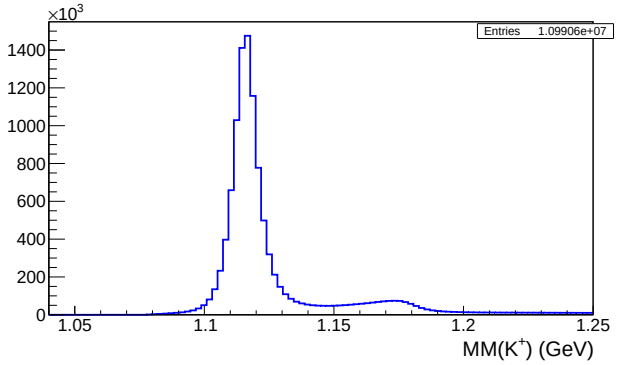

Figure 3.11: (Two-track topology) Missing mass off K^+ after kinematic fitting, with a larger than 5% confidence level cut.

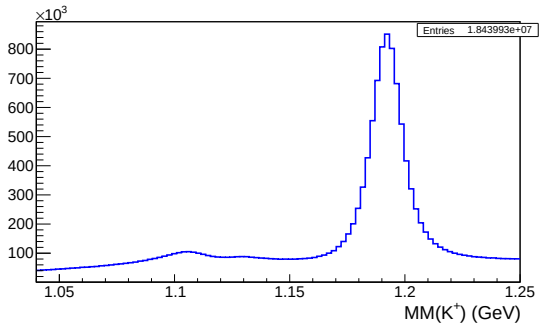

Figure 3.12: (Missing mass off K^+) Events rejected by the greater than 5% confidence level cut for the two-track topology. The distribution shows a peak around mass of Σ°.

3.10 Conclusion of Event Selections

After all the selection criteria were applied, the missing mass distribution from both analyses are shown in Figure 3.13. Here, the events for $K^+\Lambda$ from the three-track is about 0.75 million and from the two-track is about 10.1 million, that is approximately 14 times more than the three-track. Moreover, the missing mass distribution from the three-track topology (on the left) seems completely background free, but the two-track still have some background under the Λ peak. The final results for polarization observables could have dilution from these background events. The background could be polarized or unpolarized. The possible source of polarized background is $K^+\Sigma^\circ$ events. The Λ and Σ peaks are close enough (see Figure 3.9) that, there is a small probability of $K^+\Sigma^\circ$ events under the $K^+\Lambda$ peak. In the case of an unpolarized background, there is higher chance of particle misidentification between kaons and pions. The background in the two-track topology could not be further eliminated by the application of additional cuts. And due to the lack of model dependent simulation, we cannot estimate the background events. Here we have a case where the distribution of signal and background are not known and the background is not completely reduced. To handle this problem we choose the Q-factor method to estimate the

effect of the background. In this method, the desired signal events of the Λ hyperon can be extracted by weighting every single event by a quality factor, Q: $0 < Q < 1$.

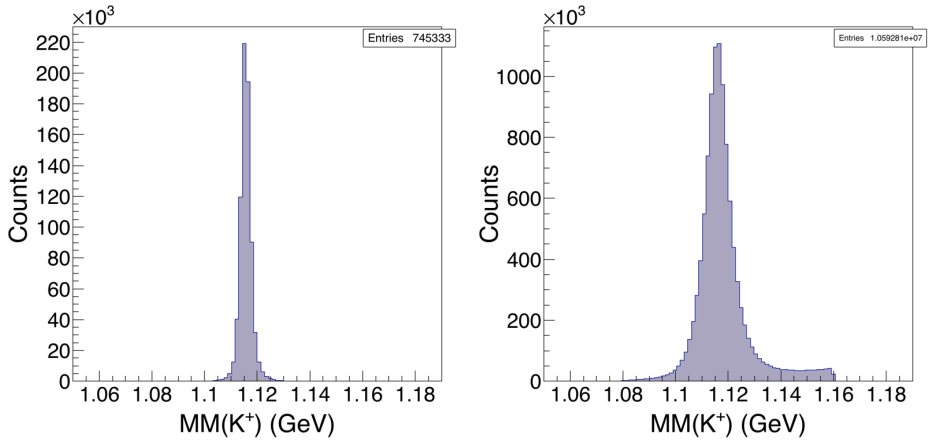

Figure 3.13: Missing mass distributions after kinematic fitting for three-track events (left) and two-track events (right).

3.11 Quality Factor

In this method, the set of coordinates that defines the multi-dimensional phase space of the reaction are categorized into two types: *reference* and *non-refrence* coordinates. With *reference* coordinate, we must know the distribution of signal and background using any set of parameters either known or unknown. In this case we are choosing the missing mass of K^+ as a reference coordinate. For *non-reference* coordinates, no *prior* information is required about the signal and background distribution, not even parametrizations are necessary. In the current work, we choose the following kinematic variables as *non-reference* coordinates:

- The cosine of the production angle of K^+ in the CM frame ($\cos\theta^{K^+}_{CM}$) with the total distribution of $\cos\theta^{K^+}_{CM}$ from -1 to 1.
- The cosine of the proton angle in the Λ-helicity frame ($\cos\theta^{p}_{\Lambda HF}$) with a range from -1 to 1.

- azimuthal angle of the proton in the Λ-helicity frame ($\phi^{p}_{\Lambda HF}$) with a range of 2π
- center-of-mass energy of the photon, W, with a range within the bin-width.

For each event, we then find a set of nearest neighbors (N_c) in the phase-space of *non-reference* coordinates by taking a minimum distance from the target event. The distance calculation is conducted using the expression,

$$d^2_{ij} = \sum_{k=1}^{3} \Big(\frac{\xi^i_k - \xi^j_k}{r_k} \Big), \tag{3.7}$$

where ξ_k are the *non-reference* coordinates (defined above), r_k is the range of the k^{th} variable. In the current work, we set N_c=1000. Thus, a sample of the 1000 nearest events were taken for every target event. Then, on an event-by-event basis, a K^+ missing mass histogram having 1000 entries from the nearest neighbor of an event was fitted by a distribution function defined as,

$$f(x) = f_s \cdot S(x) + (1 - f_s) \cdot B(x), \tag{3.8}$$

where $S(x)$ denotes the signal probability density function (`PDF`) that is defined by a relativistic Breit-Wigner convoluted with a Gaussian (Voigt function). $B(x)$ is the background probability density function that we fit with a first-order Chebychev polynomial. f_s was the signal fraction with a value between 0 and 1. The parameters and the constraints imposed on the fit are shown in Table 3.3. Before deciding an appropriate *pdf* for our data, we checked the missing mass distribution fitted by the total *pdf* (Voigt plus Chebychev) per energy bin and further $\cos\theta^{cm}_{K^+}$ within the same energy bin as shown in Figure 3.14.

Table 3.3: Q-value method probability function and their parameter.

PDF	Parameters	Initial Value	Constraints
Voigtian	Mean; μ	1115 MeV	1100 - 1130 MeV
	Gaussian width; σ	13 MeV	1 - 50 MeV
	Decay width; Γ	6 MeV	fixed
Chebychev poly.	a_0	0.5	-10 to 10

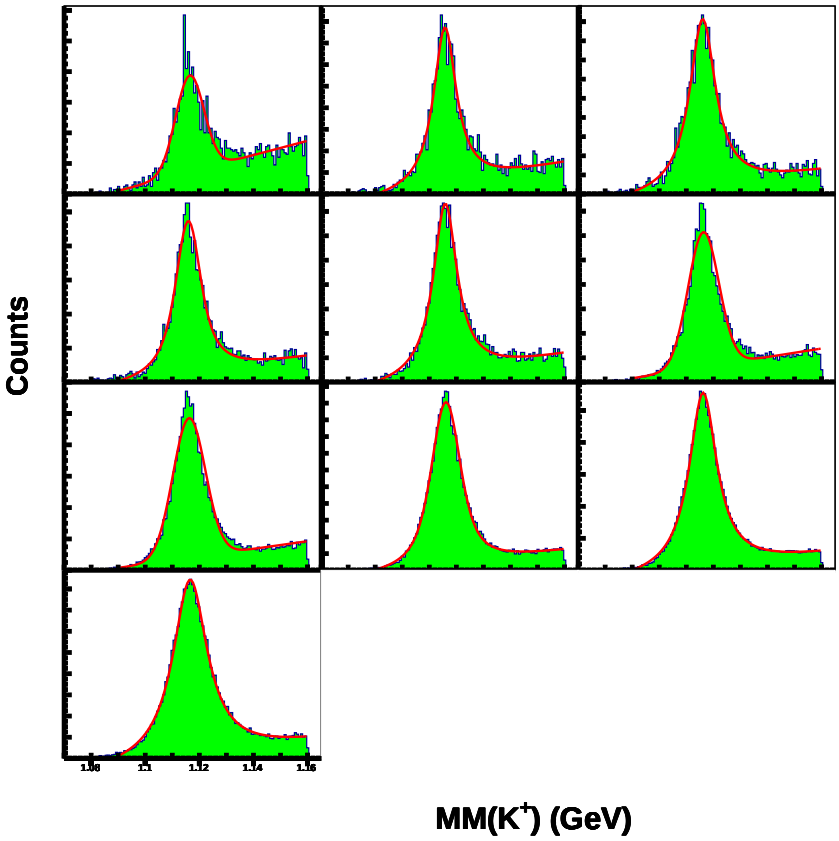

Figure 3.14: Missing mass of K^+ for a bin of $W \in [3.1, 3.2]$, further binned into $\cos\theta^{cm}_{K^+}$ from backward to forward angles. The fitted function was a Voigt plus first-order Chebychev polynomial.

The fiting procedure to extract the Q-factor was done using an unbinned maximum likelihood method from the *RooFit* package [68]. The Q-factor itself was then given by,

$$Q = \frac{s(x)}{s(x) + b(x)} \tag{3.9}$$

where x refers to missing mass of K^+, $s(x) = f_s \cdot S(x)$, and $b(x) = (1 - f_s) \cdot B(x)$. The Q-factor, which ranges from 0 to 1, is then used as an event weight to determine the signal contribution to any physics distribution.

To perform the Q-factor method in our data, we first divided the data based on different W bins (defined in Section 4.3). The Q-factor machinery was then applied to each data subset seperately. This enabled us to parallelize the procedure by submitting multiple jobs, thus significantly reducing the processing time. Figure 3.15 shows the fits to the 1000 nearest events of a randomly choosen event. Superimposed are the total fit function (blue solid line), the signal function (red solid line), and the background function (blue dotted line).

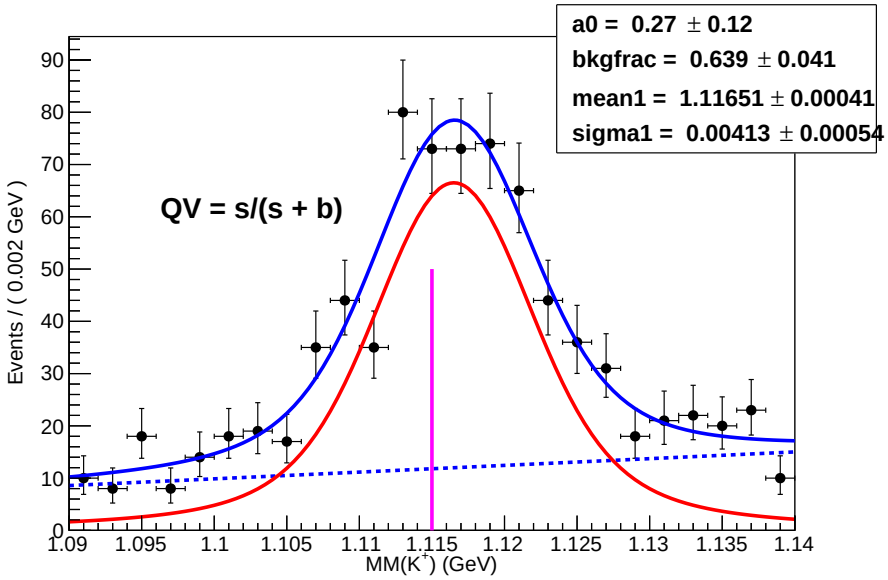

Figure 3.15: Missing mass of K^+ distribution from 1001 nearest neighbor events including a randomly choosen event of mass shown by magenta vertical line.

Figure 3.16 shows the missing mass distribution (same as in Figure 3.14), where the orange is the signal (data weighted with Q), the blue is background (data weighted with $(1-Q)$), and the total data distribution is behind shown in green.

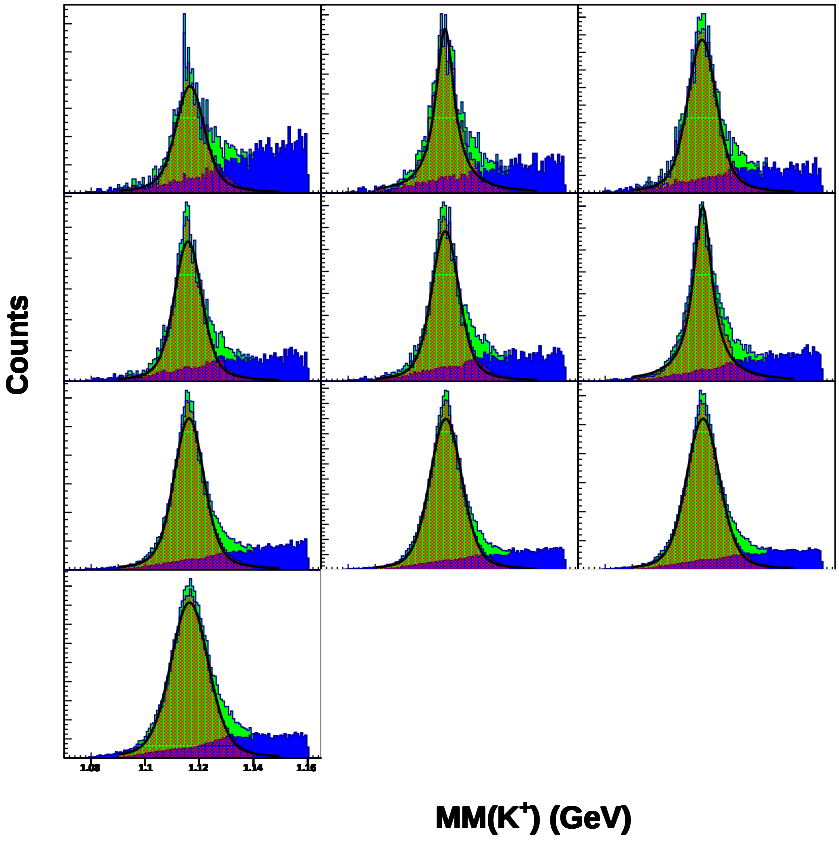

Figure 3.16: Comparison between the missing mass of K^+ for (orange) the signal events after being weighted by Q and (blue) the background events after being weighted by $(1-Q)$. The total data distribution is behind shown in green.

3.11.1 Q-factor Uncertainties: δ_Q

Q-factor uncertainties are computed as in Refs. [69, 70] using,

$$\delta_Q^2 = \sum_{ij} \frac{\partial Q}{\partial Q_{par_i}} (C^{-1}_{Q_{par}})_{ij} \frac{\partial Q}{\partial Q_{par_j}} \tag{3.10}$$

where Q_{par} are the parameters listed in Table 3.3 and $C_{Q_{par}}$ is the covariance matrix obtained from each event's fit. The δ_Q is later used to estimate the background related systematic uncertainty in each kinematic bin.

3.12 Photon beam polarization

The electron beam used for the *g12* experiment was lognitudinally polarized. The polarized electron beam produced a polarized a photon beam through the *bremsstrahlung* process using the radiator. The nature of the photon beam polarization depends on the material used for the radiator. The radiator for *g12* `CLAS` experiment was a 4 micron gold foil, allowing circular polarization of the photon beam. The degrees of the photon beam polarization is calculated using the Maximon-Olsen equation [71],

$$P_{\odot}(E_{\gamma}) = \frac{x(4-x)}{4-4x+3x^2} P_{elec}, \tag{3.11}$$

where $x = E_{\gamma}/E_{elec}$ is the ratio of the photon beam energy to the electron beam energy. The *g12* experiment ran with a constant electron energy of $E_{elec} = 5.715$ GeV. The photon beam energy is calculated using the scattering electron energy determined by the tagger and the incoming electron energy. The polarization of the electron beam was measured regularly using the Møller polarimeter. The polarimeter measures electron polarization by making use of the helicity dependent nature of Møller scattering [55, 72]. The results of the Møller measurements are summarized in Table 3.4.

Table 3.4: The degree of longitudinal electron polarization (P_e) between each Møller measurements. The uncertainties shown are statistical uncertainties.

Run Range	Møller Readout (P_e)
56355 – 56475	$(81.221 \pm 1.48)\%$
56476 – 56643	$(67.166 \pm 1.21)\%$
56644 – 56732	$(59.294 \pm 1.47)\%$
56733 – 56743	$(62.071 \pm 1.46)\%$
56744 – 56849	$(62.780 \pm 1.25)\%$
56850 – 56929	$(46.490 \pm 1.47)\%$
56930 – 57028	$(45.450 \pm 1.45)\%$
57029 – 57177	$(68.741 \pm 1.38)\%$
57178 – 57249	$(70.504 \pm 1.46)\%$
57250 – 57282	$(75.691 \pm 1.46)\%$
57283 – 57316	$(68.535 \pm 1.44)\%$

CHAPTER 4

OBSERVABLE EXTRACTION METHOD

After the clean $K^+\Lambda$ events are selected, our attention is focused on extracting the various polarization observables for the Λ hyperon; C_x, C_z, and P. Before we present the results, we would like to discuss the formalism we are using to measure the observables. The weak decay of the Λ, carried by flavor exchange, allows us to measure the polarization observables from the Λ decay products. The results will be extracted in different $\theta_{cm}^{K^+}$ and E_γ bins.

4.1 Formalism of hyperon polarization

As stated in the previous chapter, we are choosing the $p\pi^-$ decay mode of Λ, rather than $n\pi^0$ because of the low neutral particles detection efficiency in the `CLAS` detector. The polarization observables can be measured using either of the decay products of the Λ. In this analysis, we are choosing the proton in the Λ rest frame to measure the required polarization observables.

The double polarization observables C_x and C_z are related to the photon-beam polarization. The photon beam was circularly polarized, and resulted from the longitudinally polarized incident electron beam. The measurement of electron beam polarization, and hence the calculation of the degree of photon beam polarization is explained in Section 3.12.

The measurement of observables was based on the axes defined by the production plane. The production plane is defined by the momentum vectors of the incoming photon and the outgoing K^+ in the center-of-momentum frame of the $\gamma p \to K^+\Lambda$. Figure 4.1 shows the schematic for the production plane. In order to define the axes,

we utilize four vector notation for each of the particles as,

$$\gamma(k) + p(q_1) \rightarrow K^+(q_2) + \Lambda(q_3) \tag{4.1}$$

The momentum vectors are $\vec{k}$, $\vec{q_1}$, $\vec{q_2}$, and $\vec{q_3}$, which correspond to four vectors k, q_1, q_2, and q_3, respectively. As stated above, the production plane is defined by the unit vector as,

$$\hat{y} = \frac{\vec{k} \times \vec{q_2}}{|\vec{k} \times \vec{q_2}|}, \tag{4.2}$$

which is the cross product of the beam and kaon momentum.

The z-component is defined along the photon beam direction as,

$$\hat{z} = \frac{\vec{k}}{|\vec{k}|} \tag{4.3}$$

And x-component is defined from the cross product of $\hat{y}$ and $\hat{z}$ as,

$$\hat{x} = \hat{y} \times \hat{z}. \tag{4.4}$$

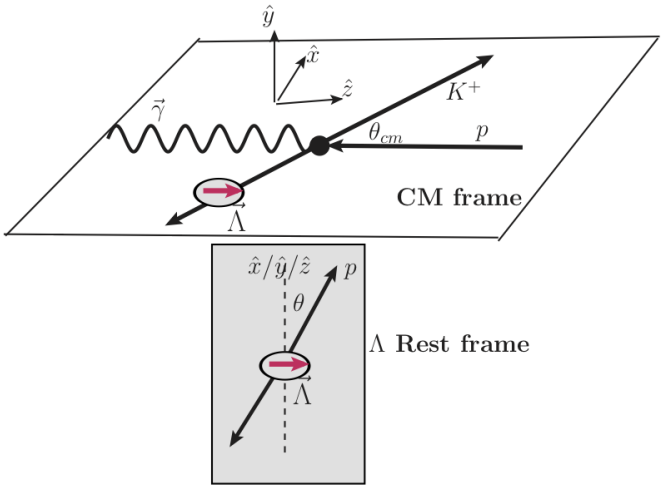

Figure 4.1: Coordinate system definition for measurement of observables C_x, C_z, and P for the Λ hyperon in the reaction $\overrightarrow{\gamma}p \to K^+\overrightarrow{\Lambda}$. (Top) The rectangular area represents the production plane defined through the incoming beam and scattered kaon. The recoil Λ is written as a vector to represent polarized production. (Bottom) The polar angle of the proton in the Λ rest frame is projected along each of the three axes defined in Λ rest frame.

The induced polarization, P, of the Λ is measured by determining the $\hat{y}$ component of the Λ polarization. The transferred polarization, C_x and C_z, are measured by determining the $\hat{x}$ and $\hat{z}$ components of the Λ polarization.

Regarding the measurement of polarization observables, there are two conventions used in defining the axes; unprime and prime. The vital difference between these two frames is on the z-coordinate definition. For the prime coordinate system, the $\hat{z}'$ is along the outgoing kaon momentum direction. We are adopting the unprimed coordinate system as in previous published analysis from `CLAS` [26], to assure the consistency of measurements.

From Ref. [20], the expression for the spin-dependent cross section ($\frac{d\sigma}{d\Omega}$) is,

$$\rho_Y \frac{d\sigma}{d\Omega_{K^+}} = \frac{d\sigma}{d\Omega_{K^+}}\Big|_{unpol.} \{1 + \sigma_y P + P_\odot(C_x\sigma_x + C_z\sigma_z)\} \tag{4.5}$$

where the hyperon density matrix ρ_Y is

$$\rho_Y = (1 + \vec{\sigma} \cdot \vec{P_Y}). \tag{4.6}$$

In Eq. 4.6, the σ's are the Pauli spin-matrices, $\sigma_x = \begin{pmatrix} 0 & 1 \\ 1 & 0 \end{pmatrix}$, $\sigma_y = \begin{pmatrix} 0 & -i \\ i & 0 \end{pmatrix}$, $\sigma_z = \begin{pmatrix} 1 & 0 \\ 0 & -1 \end{pmatrix}$, and P_Y is the hyperon polarization.

By solving Eqs 4.5 and 4.6, the hyperon polarization components are related to spin observables as,

$$\begin{aligned} P_{\Lambda_x} &= P_{\odot} C_x \\ P_{\Lambda_y} &= P \\ P_{\Lambda_z} &= P_{\odot} C_z \end{aligned} \tag{4.7}$$

The above expressions show the $\hat{x}$ and $\hat{z}$ components of hyperon polarization in the production plane are proportional to transferred spin observables through the beam polarization and $\hat{y}$ component is equal to recoil polarization.

The hyperon polarization can be expressed using a decay distribution $I_i(\cos\theta_i)$ as,

$$I_i(\cos\theta_i) = \frac{1}{2}(1 + \alpha P_{Y_i} \cos\theta_i), \tag{4.8}$$

where $P_{Y_i}, \forall i \in x, y, z$ is representing three components of hyperon polarization, and θ_i is the proton polar angle with respect to the given axis in the Λ rest frame. The

weak decay asymmetry α is 0.642 for the Λ hyperon. Expression 4.8 can be generalized to other hyperon polarization measurement as in the Refs. [25, 26, 73].

4.2 Extraction of Polarization Observables

This analysis contains three strategies to extract the double polarization observables. One is done using the beam helicity asymmetry. The beam helicity is the projection of beam polarization along the momentum direction. For the *g12* experiment, the electron-beam helicity was flipped at a rate of 30 Hz. The helicity information was recorded and stored for each event. The asymmetry is calculated for a proton angle bin ($\cos\theta_p$), by recording the number of events as $N_\pm$ for positive and negative helicity states. This asymmetry dependent method has two categories. A one dimensional fit method yielding either C_x or C_z or two dimensional fit that simultaneously yields C_x and C_z observables. A third method, called a maximum likelihood fit yields simultaneous extraction of P, C_x, and C_z. The details of these methods are described below. The examples shown in the following subsections are for two-track events.

4.2.1 One Dimensional Fit Method

This method is a simple method previously implemented for hyperon polarization measurements in the Refs. [25, 26, 73]. In this method the beam helicity asymmetry is related to the angular distribution of the proton as,

$$A(\cos\theta^p_{x/z}) = \frac{N_+ - N_-}{N_+ + N_-} = \alpha P_\odot C_{x/z} \cos\theta^p_{x/z} \tag{4.9}$$

where A is the beam helicity asymmetry, $P_{\odot}$ is the photon beam polarization, α is the weak decay asymmetry, and $\cos(\theta^{p}_{x/z})$ is the angular distribution of proton in the rest frame of Λ.

Eq. 4.9 shows that the asymmetry is a linear function of the cosine of the proton angle, and the slope of this distribution gives the polarization observables. $N_{\pm}$ is the helicity-dependent hyperon yield for a single bin. Detector effeciencies are not affected by the helicity states of the incident photon, and hence the helicity asymmetry does not require acceptance correction. Any possible acceptance corrections would factor out in the asymmetry measurements.

Figure 4.2 shows the asymmetry distribution plotted against the proton angle projections along x (top) and z (bottom) axes for W= 3.2 – 3.33 GeV in different $\cos\theta^{cm}_{K^+}$. The asymmetry is then fit with a linear function. These fits for proton angular distribution will give us the spin observables C_x and C_z after equating the slope value to $\alpha P_{\odot} C_{x/z}$.

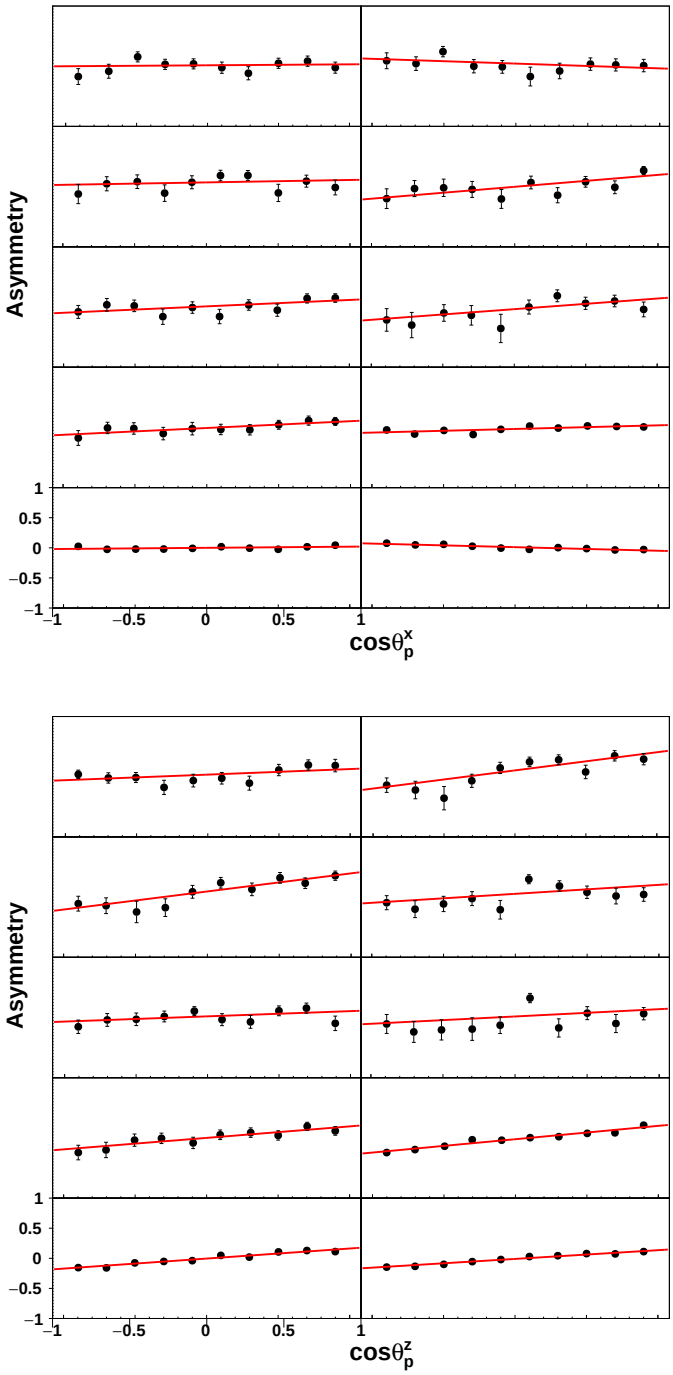

Figure 4.2: Beam helicity asymmetry as a function of the angular distribution of the proton. Top panel are used to extract C_x and the bottom panel are used to extract C_z

The error bars on the asymmetries are purely statistical uncertainties and were calculated analytically as,

$$\delta_A = \sqrt{\delta_{N_+}^2 \left(\frac{\partial A}{\partial N_+}\right)^2 + \delta_{N_-}^2 \left(\frac{\partial A}{\partial N_-}\right)^2}, \tag{4.10}$$

where $\delta_{N_\pm}$ are the yield uncertainties for the specified helicity and is the square root of the yield number. The partials in Eq. 4.10 are

$$\frac{\partial A}{\partial N_\pm} = \pm \frac{2N_\pm}{(N_+ + N_-)^2}, \tag{4.11}$$

Substituting partials from Equation 4.11 to Equation 4.10, the error on the asymmetry becomes,

$$\delta_A = \frac{2}{(N_+ + N_-)^2} \sqrt{N_-^2 \delta_{N_+}^2 + N_+^2 \delta_{N_-}^2} \tag{4.12}$$

The uncertainity on observables C_x and C_z are the fit uncertainity coming from the linear fit to the asymmetry distribution. The results from the one dimensional fit method strictly depends on fit quality. The quality of a fit was checked by both visual inspection and measuring the χ^2/ndf for the fit. The distribution of χ^2/ndf after a linear fit to the asymmetry distribution for all energy and kaon angle bins, is shown in Figure 4.3. The best fit is considered when $\chi^2/ndf \approx 1$. During the fitting process, we allowed the fit parameter to be free, that caused some of the $\chi^2/ndf > 1$. Those bins were further checked by visual inspection to verify the quality of fit.

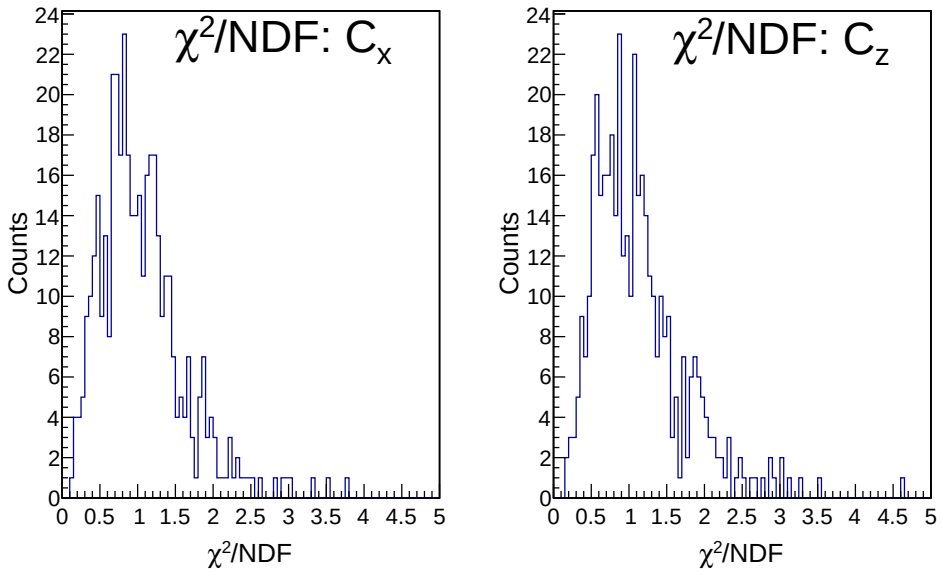

Figure 4.3: The distribution of χ^2/ndf from the one-dimensional fit for polarization observables C_x (left) and C_z (right).

4.2.2 Two Dimensional Fit Method

In this method we can extract both transferred polarization observables C_x and C_z simultaneously. The asymmetry expression for this method is,

$$A(\cos\theta_x^p, \cos\theta_z^p) = \frac{N_+ - N_-}{N_+ + N_-} = \alpha P_\odot C_x \cos\theta_x^p + \alpha P_\odot C_z \cos\theta_z^p, \tag{4.13}$$

where A is the asymmetry, and is a function of both angular distributions of the proton ($\cos\theta_x^p$ and $\cos\theta_z^p$). The $N_\pm$ are the number of events for positive and negative helicity events after the two dimensional binning on the angular distribution of the proton. After the two dimensional fit on the asymmetry, the observables are extracted from the fit parameters of the distribution. Figure 4.4 shows the χ^2/ndf for all the fits.

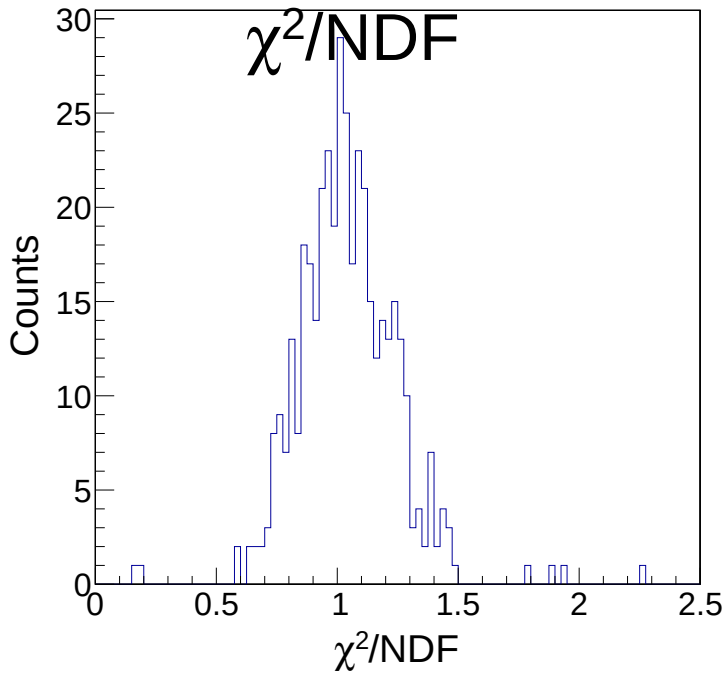

Figure 4.4: The distribution of χ^2/ndf from the two dimensional fit method.

4.2.3 Maximum Likelihood Method: Extracting C_x, C_z, and P

In the previous two methods, the asymmetry data were fitted using a least squares method to extract the polarization observables. The asymmetries were binned in the proton angular distribution, where binning was governed based on the number of events. It is possible that the binning of data can hide some of the features of the asymmetry. The maximum likelihood method is an event-by-event based method that does not require any binning, thereby preventing any loss of information. The Unbinned maximum likelihood method allowed us to extract the polarization observables C_x, C_z, and P simultaneously. A detailed description about the method and techniques of implementation was described in a `CLAS` note [74]. In the maximum likelihood method, the fit is optimized by maximizing the likelihood function. The likelihood function is defined as the product of the probability density function as,

$$\mathbb{L} = \prod_{i=1}^{N} \mathcal{P}_i, \tag{4.14}$$

where $\mathcal{P}_i$ is the total probability density function that requires a product of individual distribution function for all events N. A single event probability distribution function is defined as,

$$\mathcal{P}(\cos\theta_x^p, \cos\theta_z^p, \cos\theta_y^p | C_x, C_z, P) = 1 \pm P_\odot \alpha (C_x \cos\theta_x^p + C_z \cos\theta_z^p) + \alpha P \cos\theta_y^p. \tag{4.15}$$

In this analysis each event has its own weight, w_i, it was calculated using the Q-factor method (see Section 3.11. So the likelihood function from Eq. 4.14 becomes,

$$\mathbb{L} = \prod_{i=1}^{N} [\mathcal{P}_i]^{w_i} \tag{4.16}$$

It is convenient to minimize the negative log-likelihood rather than maximizing likelihood by using the standard packages, named `MINUIT` [75, 76]. After applying the natural logarithm, the product on the right side of Equation 4.15 turns into a summation as,

$$-\log\mathbb{L} = -\sum_{i=1}^{N} w_i \log(P_i) \tag{4.17}$$

Using probability distribution function from Eq. 4.15 into Eq. 4.16,

$$-\log \mathbb{L} = -\sum_{i=1}^{N} w_i \log(1 \pm P_{\odot}\alpha(C_x \cos\theta_x^p + C_z \cos\theta_z^p) + \alpha P \cos\theta_y^p). \tag{4.18}$$

In the next chapter, we are executing all of the formalisms that were developed in this section to obtain the results for the polarization observables. The results can then be compared between different methods.

4.3 Kinematic Binning of Data

Before elaborating on the kinematic binning of our data, we must discuss the kinematic coverage. The incoming electron beam had a constant energy of 5.71 GeV. With this electron energy, after the *bremsstralung* process, the photon beam has an energy range. The calculation of a photon energy is associated with the measured energy in the tagger system. Since the `CLAS` tagger system detects electrons with energy of 20 to 95 % of the incoming energy, the *g12* photon beam has energy from 1.1 to 5.45 GeV. The spin observables are also extracted within this range. Previously, the measurements were conducted down to the threshold energy of 0.91 GeV. In this analysis the measurement go down to 1.17 GeV, instead.

The spin observables are measured as a function of the center-of-momentum energy, W, and the kaon center-of-momentum angle $\cos\theta_{K^+}^{cm}$. The data are binned in W and $\cos\theta_{K^+}^{cm}$. The binning has been choosen to match that of the previous `CLAS` results, when possible. Large bin sizes are necessary at higher energies to improve statistical precision. The binning is shown in Table 4.1 and Figure 4.5 for the two-track topology and in Table 4.2 and Figure 4.6 for the three-track topology events.

Table 4.1: Binning scheme applied for W and $\cos\theta^{CM}_{K^+}$ for two-track topology.

W Bin GeV	Bin width GeV	No. of Bins	$\cos\theta^{CM}_{K^+}$	Bin width	No. of Bins
[1.75, 2.35)	0.02	30	[-0.85, -0.5)	0.35	1
[2.35, 2.5)	0.05	3	[-0.5, 0.0)	0.25	2
[2.5, 2.56)	0.06	1	[0.0, 0.4)	0.2	2
[2.6, 3.2)	0.1	6	[0.4, 0.55)	0.15	1
[3.2, 3.33)	0.13	1	[0.55, 0.95)	0.1	4

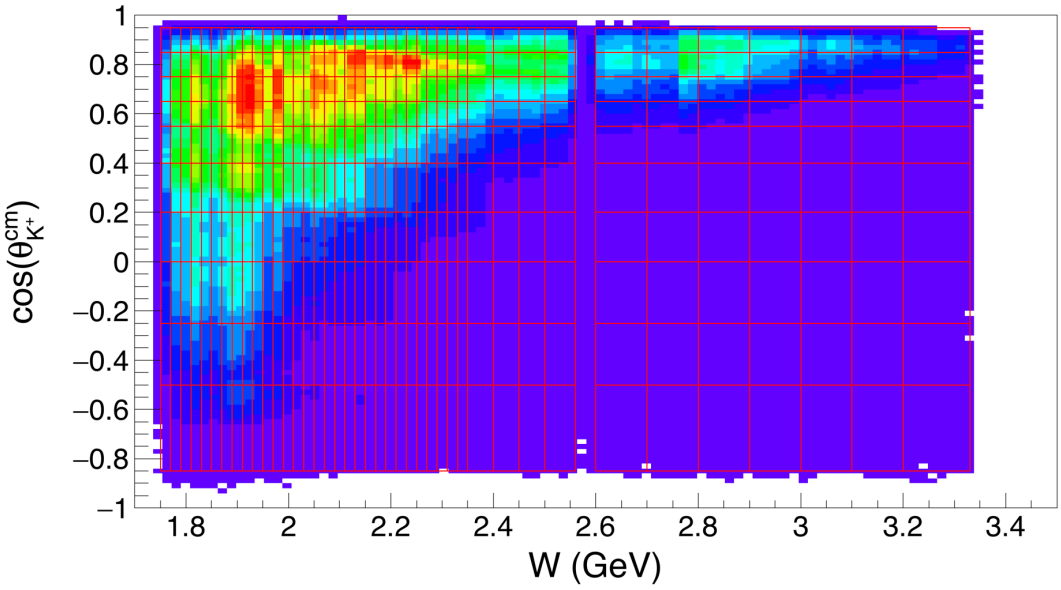

Figure 4.5: Plots of $\cos\theta^{cm}_{K^+}$ vs W with lines to show the binning for the two-track topology.

Table 4.2: Binning scheme applied for W and $\cos\theta^{CM}_{K^+}$ for three-track topology.

W Bin GeV	Bin width GeV	No. of Bins	$\cos\theta^{CM}_{K^+}$	Bin width	No. of Bins
[1.75, 2.55)	0.05	16	[-0.85, -0.5)	0.35	1
[2.5, 2.95)	0.1	4	[-0.5, 0.0)	0.25	2
[2.95, 3.1)	0.15	1	[0.0, 0.4)	0.2	2
[3.1, 3.33)	0.23	1	[0.4, 0.55)	0.15	1
			[0.55, 0.95)	0.1	4

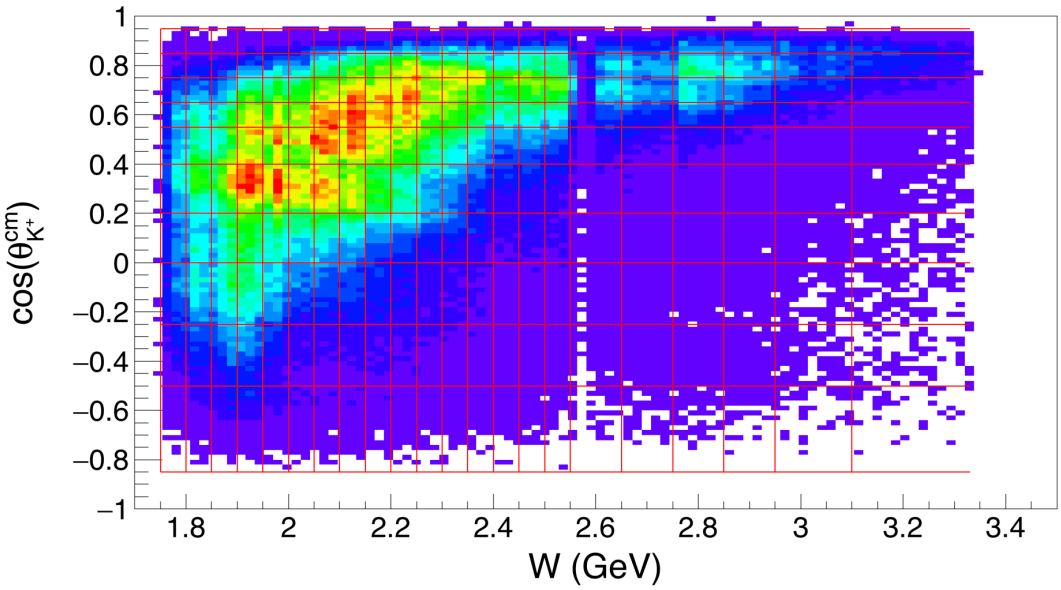

Figure 4.6: Plots of $\cos\theta^{cm}_{K^+}$ vs W with lines to show the binning for the three-track topology.

CHAPTER 5

DETERMINATION OF C_x, C_z, AND P

This chapter provides the results of our Λ polarization measurement in the reaction $\gamma p \to K^+\Lambda$. For extracting the polarization observables C_x, C_z, and P, we used two- and three-track topologies. A comparison between the results of polarization observables from the two topologies are discussed in section 5.2. Moreover, three methods from previous chapter were used to measure the polarization observables. The results of these three methods are provided in section 5.1. Furthermore, we present the studies performed to quantify the systematic uncertainties of the polarization observables.

5.1 Measurement of C_x, C_z observables

The helicity dependent observables C_x and C_z were extracted using all three methods; the one-dimensional fit, the two-dimensional fit, and the maximum likelihood, while the helicity independent observable, P, was extracted using only the maximum likelihood method.

Figures 5.1 to 5.4 show comparisons between three methods for the C_x and C_z as a function of $\cos\theta^{cm}_{K^+}$ for fixed W, respectively. The one-dimensional results are shown in red, the two-dimensional are in green, and the maximum likelihood are in blue.

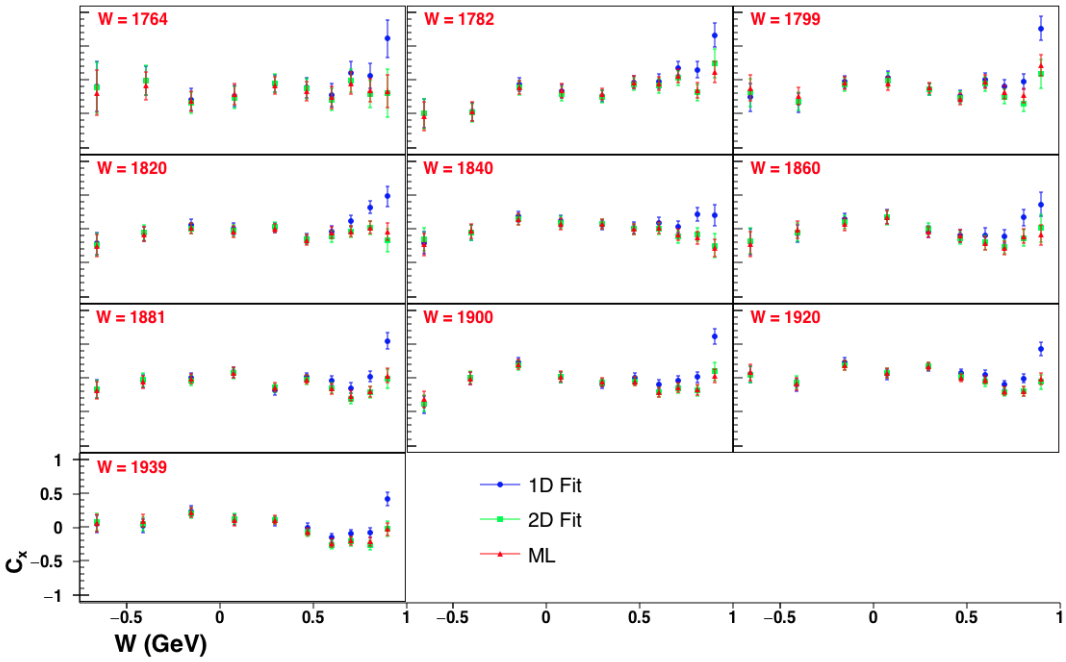

Figure 5.1: C_x vs $\cos\theta^{cm}_{K^+}$ for different W bins, ranged from 1.75 – 1.94 GeV. The results for the C_x were measured using three different methods; the one dimensional fit method (blue), the two dimensional fit method (green), and the maximum likelihood method (red) from two-track analysis.

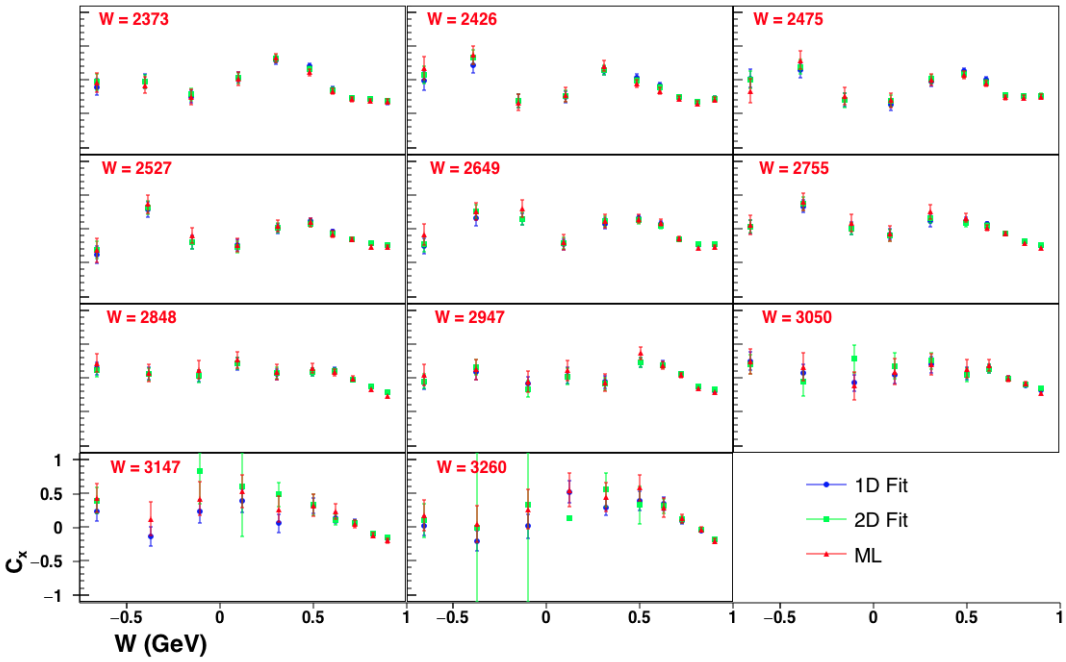

Figure 5.2: C_x vs $\cos\theta^{cm}_{K^+}$ for different W bins, ranged from 2.3 – 3.33 GeV. The results for the C_x were measured using three different methods; the one dimensional fit method (blue), the two dimensional fit method (green), and the maximum likelihood method (red) from two-track analysis.

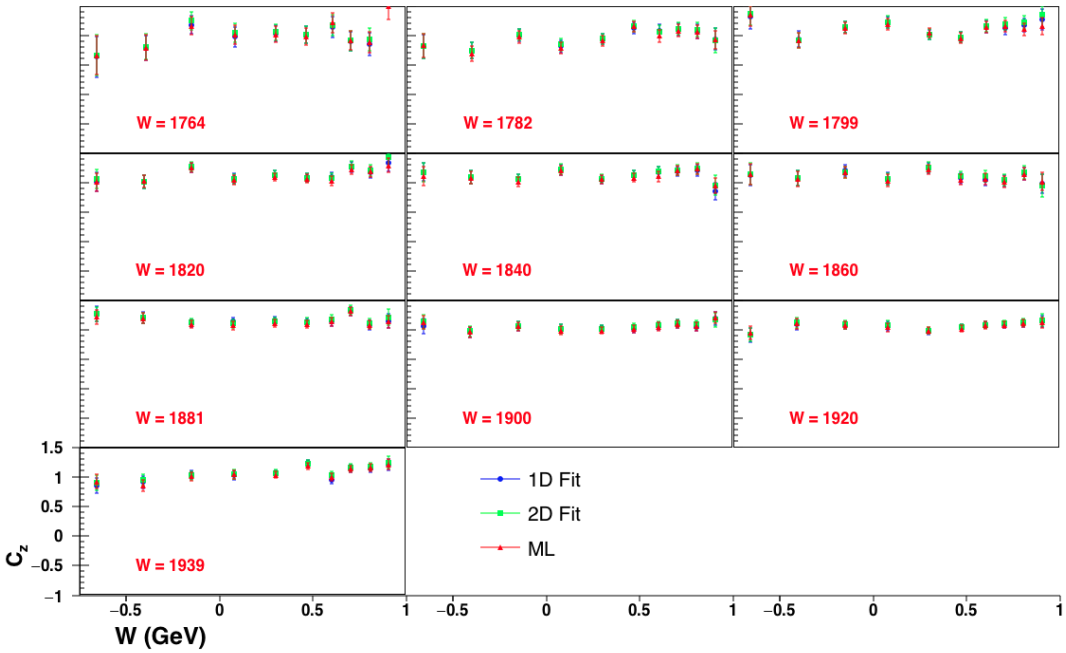

Figure 5.3: C_z vs $\cos\theta^{cm}_{K^+}$ for different W bins, ranged from 1.75 – 1.94 GeV. The results for the C_z were measured using three different methods; the one dimensional fit method (blue), the two dimensional fit method (green), and the maximum likelihood method (red) from two-track analysis.

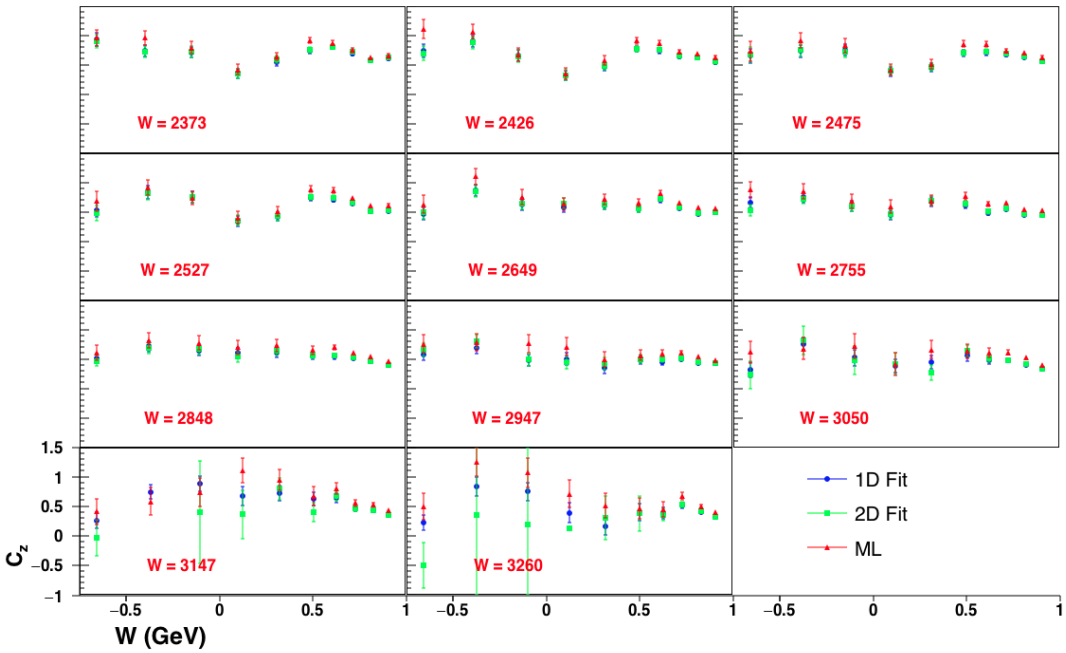

Figure 5.4: C_z vs $\cos\theta^{cm}_{K^+}$ for different W bins, ranged from 2.3 – 3.33 GeV. The results for the C_z were measured using three different methods; the one dimensional fit method (red), the two dimensional fit method (green), and the maximum likelihood method (red) from two-track analysis.

Figures 5.1 and 5.3 include the results from low energies region, i.e., W= 1.75 – 1.94 GeV, where the two-track has almost no background events. Within this W range, the results from three methods show an excellent agreement for both C_x and C_z . On the other hand, at high energy region, i.e., W = 2.3 – 3.33 GeV, the results from the one-dimesional and the two-dimensional does not agree well with the maximum likelihood method. The difference distribution in Figure 5.5 shows the variation between the maximum likelihood method and, the one dimensional and the two-dimensional fit methods. Because the results from maximum likelihood method were corrected to background but not for other two methods, the high energy results from Figures 5.2 and 5.4, are inconsistent. We prefered the maximum likelihood method that can easily handle the background using the Q-factor method.

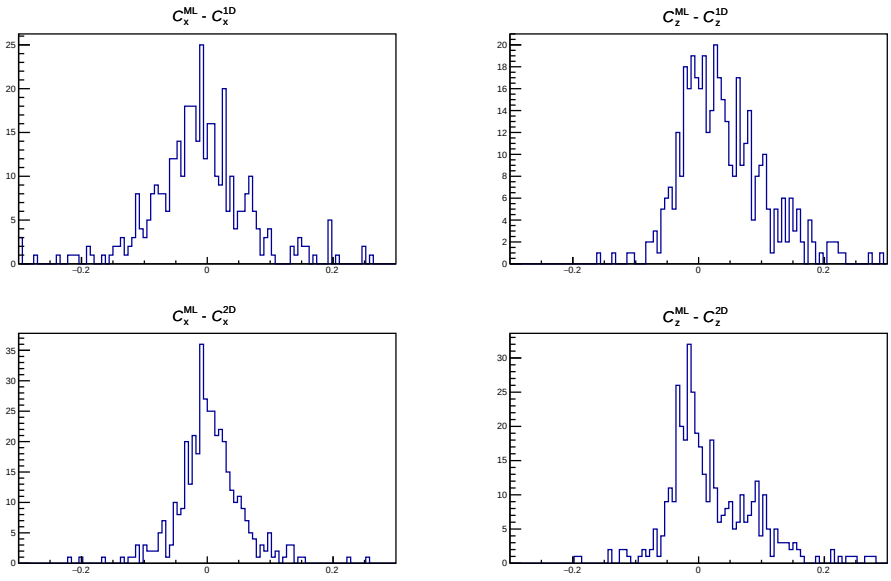

Figure 5.5: Difference distributions of C_x and C_z observables from the maximum likelihood method and, the one dimensional and the two dimensional methods.

Among these three measurement methods, the maximum likelihood method has the advantage of measuring three observables simultaneously. Moreover, the Q-value can be used in the distribution function as a weight for the maximum likelihood method, so that we can reduce the dilution from the background directly in the process of measurement. Because of these reason, we are extracting the final results of the polarization observables using the maximum likelihood method.

5.2 Comparison between two-track and three-track results

Figures 5.6, 5.7, and 5.9 show comparison of our results from the two topologies. The binnings in W and $\cos\theta^{cm}_{K^+}$ are different in both cases, are described in Section 4.3. Both results were binned within the same end point energy range from 1.75 GeV to 3.33 GeV in W, as well as the same $\cos\theta^{cm}_{K^+}$ bins from -0.85 to 0.95. Because of the high level of exclusivity, the final $K^+\Lambda$ events for the three-track topology has fewer

statistics compare to the two-track that requires a wider binning in W, compared to two-track topology.

We used almost the same event selection processes, except for the confidence level cut (see Section 3.9). Also, we used the same method, the maximum likelihood method. The agreement between the two results for C_x and C_z is very good over the entire kinematic range, in Figures 5.6 and 5.7 respectively. Due to limited statistics in the three-track analysis, the statistical error bars of our results (shown in blue) are large, and the two-track results (shown in red) fall within statistical uncertainty.

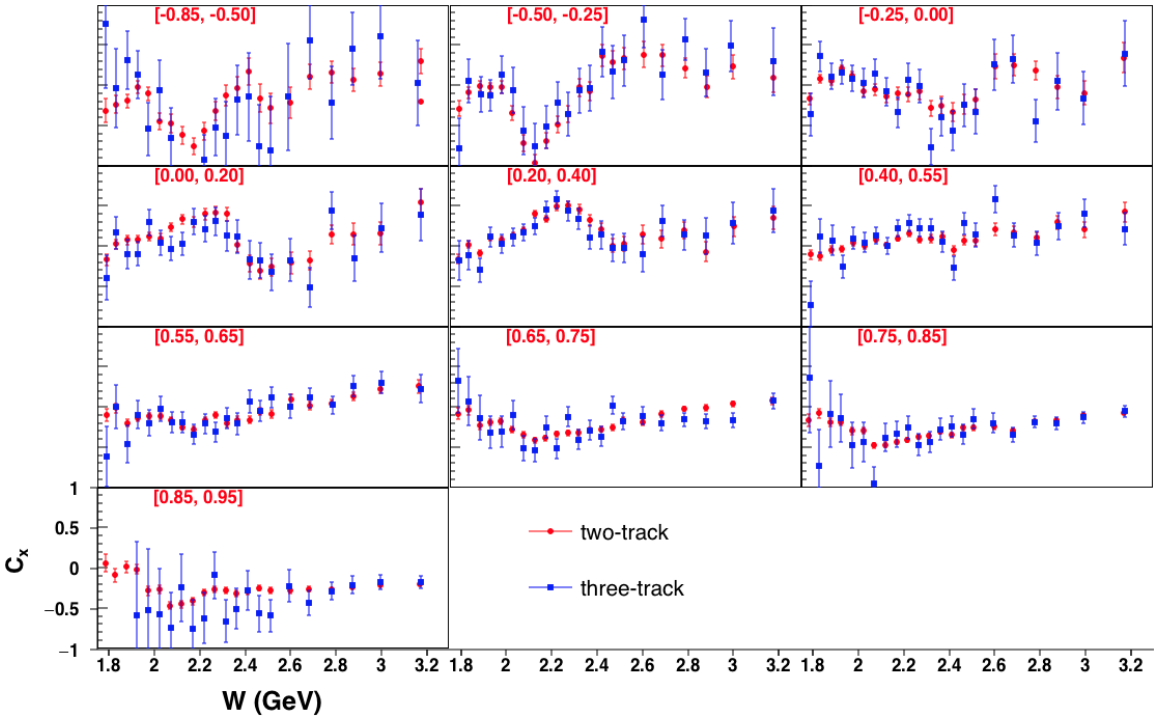

Figure 5.6: Comparison of results from three-track (red) and two-track (blue) topologies for the C_x observable.

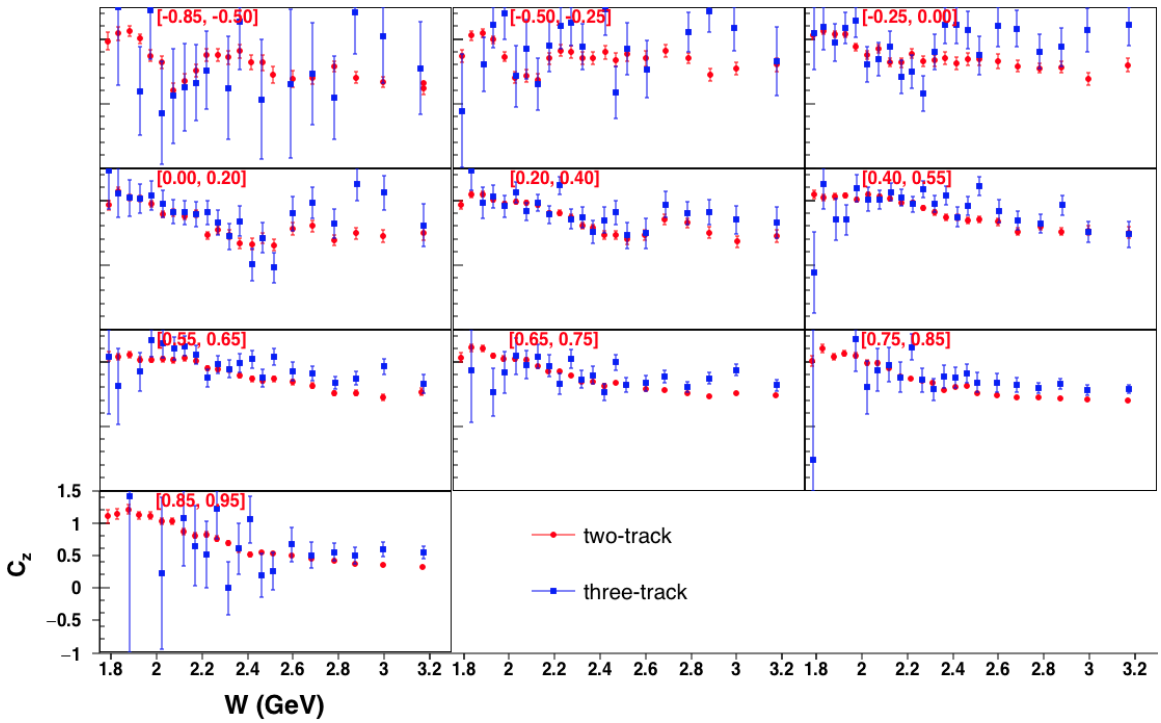

Figure 5.7: Comparison of results from three-track (red) and two-track (blue) topologies for the C_z observable.

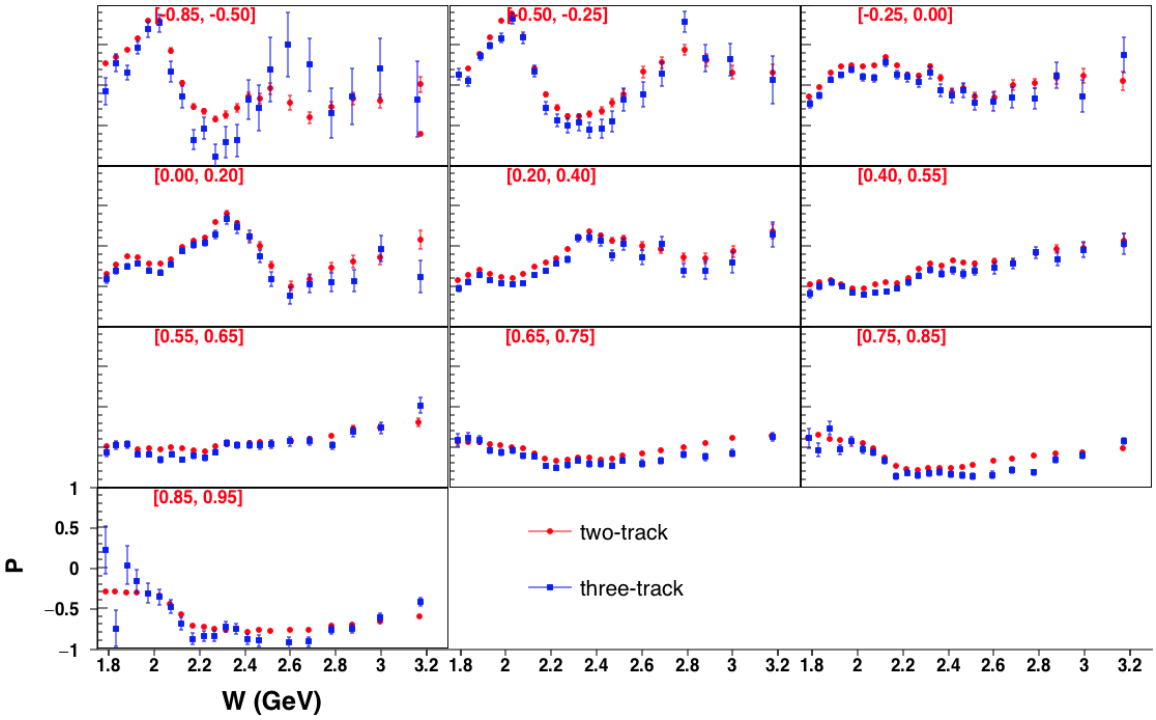

Figure 5.8: Comparison of results from three-track (red) and two-track (blue) topologies for the P observable.

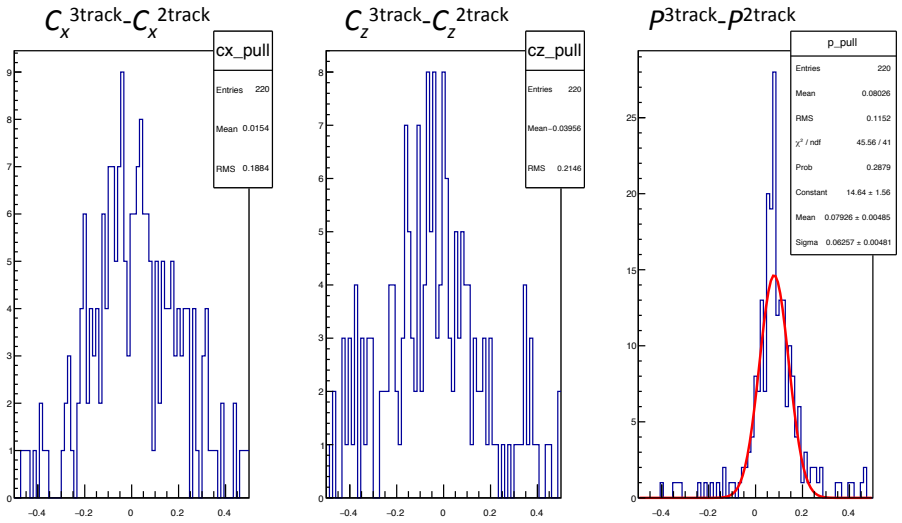

Figure 5.9: Difference distribution between three observables.

5.3 Systematic Uncertainty

The total uncertainty for C_x, C_z, and P has two contributions, statistical uncertainty and systematic uncertainty. The statistical uncertainties are given by the measurements based on the total number of counts on each kinematic bin, which has already been described in the previous chapter. Unlike statistical uncertainty, there is no clear recipes for the determination of the systematic uncertainty. Sometimes it is hard to disentangle the systematic uncertainty from statistical uncertainty. In any experiment, there are multiple sources of systematic uncertainties: detector acceptance, detector resolution, backgrounds, and so on. In this section, we will describe the sources of systematic uncertainties that contribute to the total systematics by factoring the systematics into two broad categories: Point-to-point (uncorrelated) and Scale-type. Furthermore, the point-to-point type includes the event-selection cuts and the background subtraction process, whereas, the scale-type includes the photon polarization and the hyperon analyzing power. Particulary, from the point-to-point type, the total systematic uncertainty is calculated by adding all the individual sources in quadrature, assuming no correlation between each of those as,

$$\delta_{sys,tot} = \sqrt{\sum_{src} \delta^2_{sys,src}} \tag{5.1}$$

where $\delta_{sys,src}$ is a single source systematic uncertainty for a measurement.

More details about each source for systematic uncertainty are presented and the summary table at the end reports all the systematic uncertainties.

5.3.1 Uncertainties from event-selection cuts.

We have implemented multiple selection cuts in Chapter 3 to obtain pure $K^+\Lambda$ events. With the variation of a selection cut, the datasets are enlarged or reduced, thus the effects of specific sources of systematics may be enhanced or reduced. The selection cuts we have are the timing cut, the vertex cut, the fiducial cut, and the confidence level cut. By changing the nominal value for a cut, the resulting observable was varied. The uncertainties are then calculated using the two different measurements by,

$$\delta_{sys} = \sqrt{\frac{\sum_i \left(\frac{\mathcal{O}^i_{nom} - \mathcal{O}^i_{alt}}{\delta\mathcal{O}^i_{nom}}\right)^2}{\sum_i \left(\frac{1}{\delta\mathcal{O}^i_{nom}}\right)^2}}, \tag{5.2}$$

where $\mathcal{O}_{nom}$ is the general representation for a polarization observable that was measured using the nominal cut in the event selection process, and $\mathcal{O}_{alt}$ is the measurement after modification of the selection cut.

Vertex cuts

The vertex cut discussed in section 3.4 has two parts, a z-vertex cut and a radial vertex cut. The z-vertex cut, which is charaterized based on the reconstruction along the target length was defined by $|z - 90| < 20$ cm. And the radial vertex cut was $r < 5.0$ cm. The systematic uncertainity can be estimated by varying (contracting) those nominal cuts by 10 %. This means that $|z - 90| < 20$ cm changes to $|z - 90| < 18$ cm. Also, $r < 5$ cm changes to $r < 4.5$ cm. The systematic uncetainity on the observables C_x, C_z, and P after varying the vertex cut is calculated using Eq. 5.2,

and the values are in Table 5.1. Figure 5.10 shows the difference distribution for C_x, C_z, and P after varied the vertex cuts.

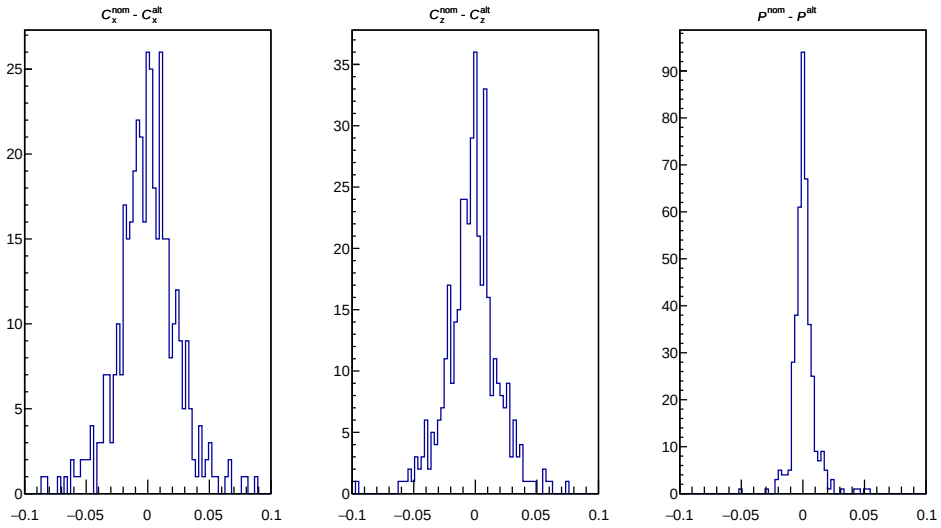

Figure 5.10: Difference distributions of C_x, C_z, and P after varying the z-vertex cut from $|z - 90| < 20$ cm to $|z - 90| < 18$ cm and a radial cut from $r < 5.0$ cm to $r < 4.5$ cm.

Vertex timing cut

In order to quantify the systematic uncertainity due to our specific choice of a cut range for photon selection based on vertex timing, i.e. ± 1 ns (our nominal cut), we varied by 10% to ± 0.9 ns. Figure 5.11 shows the difference distributions of C_x, C_z, and P from the nominal and modified results. The systematic uncertainties of C_x, C_z, and P due to the timing cut are reported in the Table 5.1.

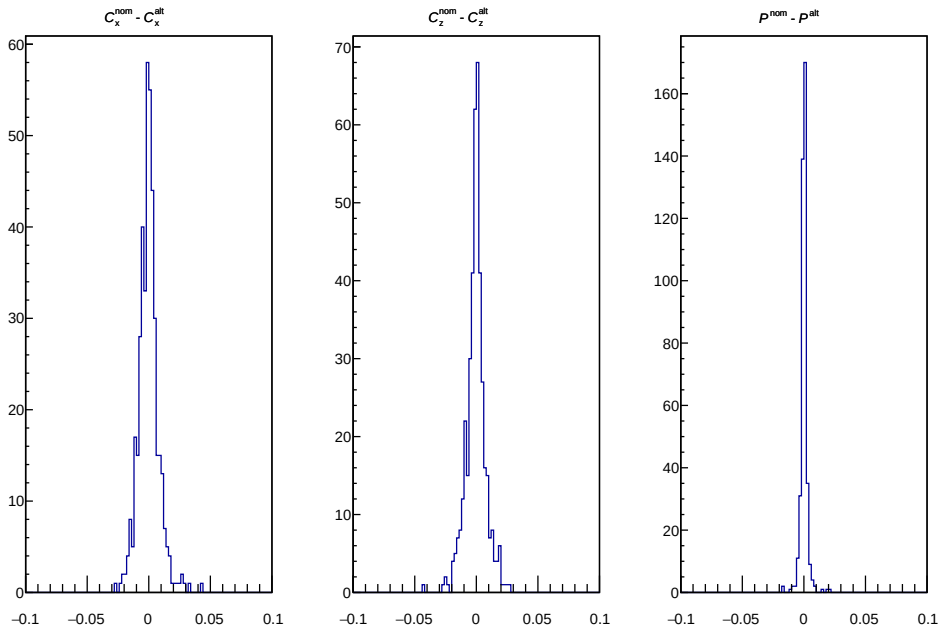

Figure 5.11: Difference distributions of C_x, C_z, and P observables after varying the vertex timing cut. A variation was set to be ± 0.9 ns as opposed to the ± 1 ns nominal cut.

Fiducial cut

The *nominal fiducial cut* that was applied in the current work, as described in Section 3.6, is changed to the *tight fiducial cut* to estimate the systematic uncertainties for C_x, C_z, and P due to this cut. The effect of nominal and tight fiducial cuts in the final state particles, K^+ and proton, are shown in Figure 3.5.

Figure 5.12 shows the difference distribution of C_x, C_z, and P after changing the selection from nominal to tight. Using Eq. 5.2, we got the absolute uncertainty for C_x, C_z, and P, which are tabulated in Table 5.1.

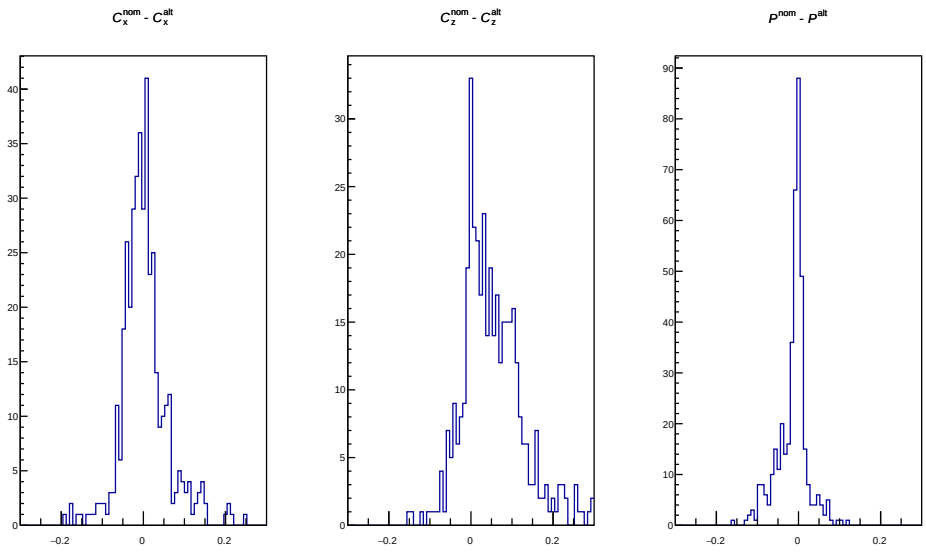

Figure 5.12: Difference distributions of C_x, C_z, and P observables after changing the fiducial cut from nominal to tight cut.

Confidence level cut

The kinematic fitting confidence level cut was applied for both three-track and two-track analyses. In this part, we have final results from the two-track analysis. So, in changing our nominal selection for two-track from 5% to 10%, we reduced the statistics for $K^+\Lambda$ events by removing the low confidence level events, those correspond to the background events. The estimated systematic uncertainties for C_x, C_z, and P from this method are tabulated in Table 5.1

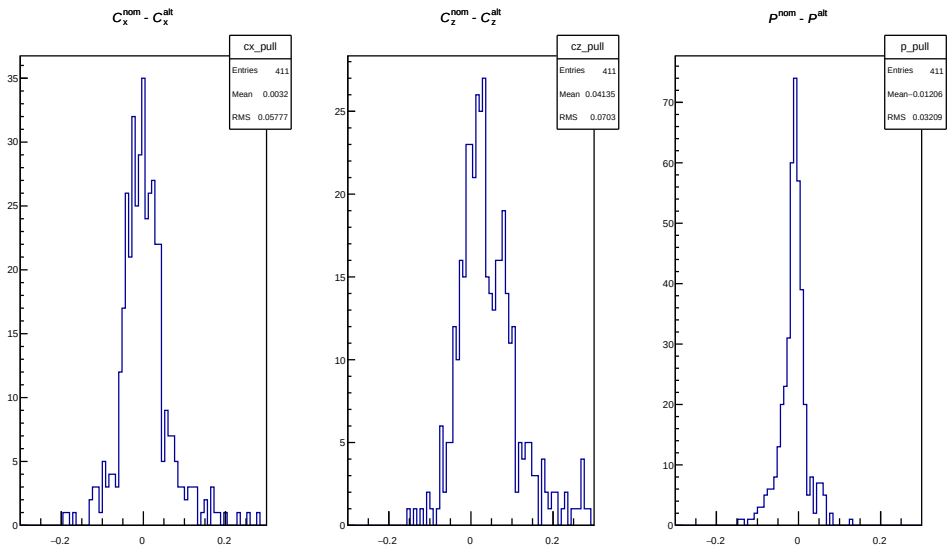

Figure 5.13: Difference distributions of C_x, C_z, and P observables after changing the 5% confidence level cut to 10% for $K^+p(\pi^-)$ events.

5.3.2 Uncertainties of background subtraction procedure

The Q-factor method we used as a background substraction contributes to the systematic uncertainty. It is hard to solve analytically and get the systematic from the Q-value, where extraction of observables is done by fitting the data. Therefore an alternative approach was applied. We changed the Q-value of each event by δ_{Q_i} (see the definition in section 3.11.1), where the δ_{Q_i} denotes the fit error in the Q-value of the i^{th} event. The modification was done by adding or substracting the δ_{Q_i} from the Q-value of each event. In the next step, we used the maximum likelihood method to extract all the polarization observables. The difference between the original and the modified observables, was used as the systematic uncertainity. Since we had Q-value variation through both adding and subtracting δ_{Q_i}, the average of the two variations becomes a systematic uncertainity for each bin. Figure 5.14 shows the results for C_x observables that are weighted by their Q-value and also weighted by modified

Q-value. The modification results are shifted by a small amount, which can be seen from the difference distribution in Figure 5.15.

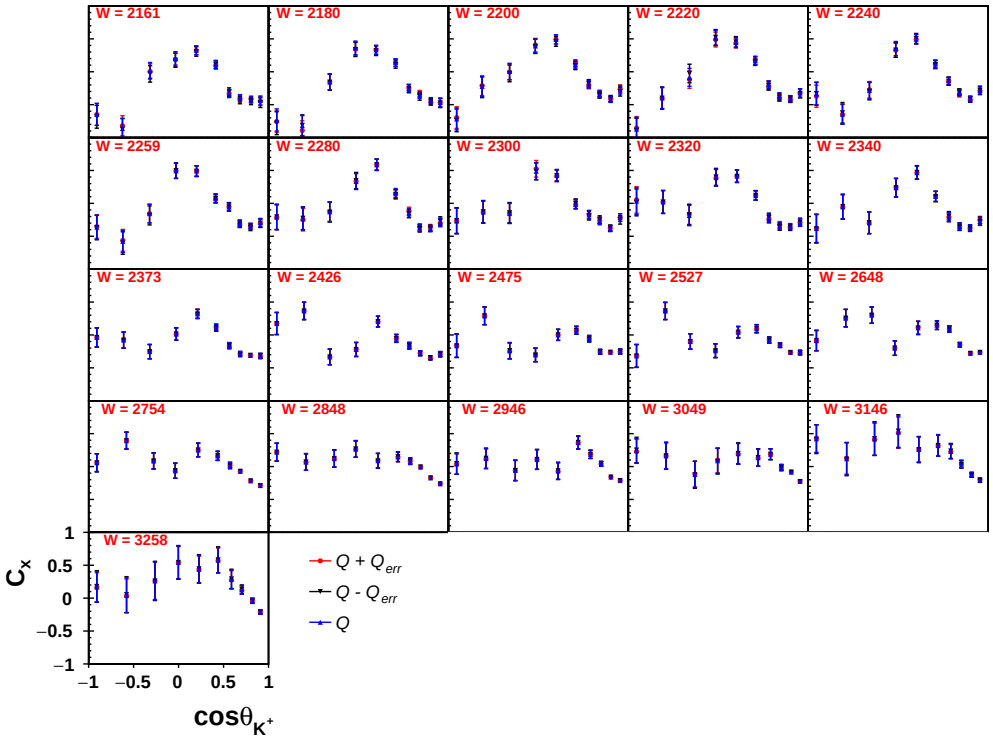

Figure 5.14: C_x vs $\cos\theta^{cm}_{k^+}$, weighted by a Q-value on each kinematic bin. The modification on the Q-value was done by adding or subtracting by the corresponding Q-value error.

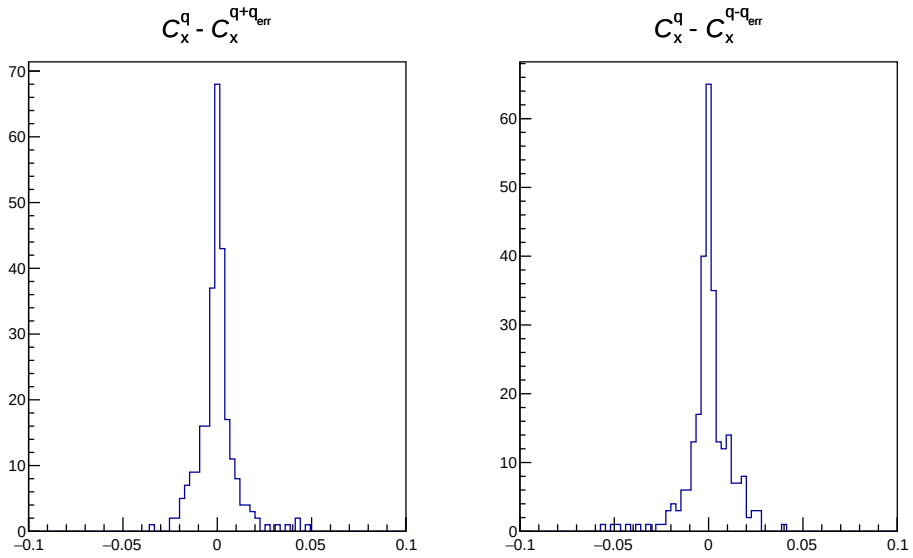

Figure 5.15: An example of difference distributions for C_x: (left) Difference between measurement with Q-value and $Q + Q_{err}$. (right) Difference between measurement with Q-value and $Q - Q_{err}$.

5.3.3 Systematics from Photon polarization and Self-analyzing power of the Λ

As a scale-type, we are measuring the systematic uncertainty of C_x, C_z, and P from the photon polarization and the self-analyzing power of Λ, $\alpha = 0.642 \pm 0.013$. From the maximum likelihood method, the final estimate for C_x and C_z are obtained by dividing the corresponding fit parameters by $\alpha = 0.642 \pm 0.013$ and photon polarization $P_\odot$ (details are in Section 4.2), whereas, the final estimate for P are obtained by dividing α only. So, the systematic uncertainity for C_x and C_z have uncertainties from α and $P_\odot$, and the systematic uncertainty for P has only from α. More details about the systematic uncertainty from these scale-type sources are presented in the following sections.

Systematic uncertainty from the Self-analyzing power

The relative uncertainty for C_x and C_z from the Self-analyzing power is estimated from the uncertainty propagation as,

$$\begin{aligned} \delta_\alpha(C_i) &= |C_i \frac{\delta\alpha}{\alpha}| \\ &= |C_i| 0.0202 \end{aligned} \tag{5.3}$$

which is 2.02% relative error. Similarly for P, the measurement of relative error is,

$$\delta_\alpha P = |P| 0.0202. \tag{5.4}$$

Systematic uncertainty from the photon polarization

In Eq. 3.11, assuming the electron and photon energies were correctly measured, the total uncertainty on the photon polarization propagate only from the electron polarization. From Table 3.4, the average uncertainty for the photon polarization from different runs is about 1.5%. Uncertainty propagation yields that the relative uncertainty of each C_x and C_z, taking an average beam polarization, is,

$$\delta P_\odot(C_i) = |C_i| 0.05 \tag{5.5}$$

This is the relative systematic uncertainty of C_x and C_z as for the scale-type.

5.3.4 Summary of Systematic Uncertainty

Table 5.1 reports the systematic uncertainties of C_x, C_z, and P from both the scale-type and the point-to-point type. The systematic uncertainties from the scale-type are relative errors, whereas the point-to-point types are absolute errors. The final results for C_x, C_z, and P reported in the next chapter include the total systematic uncertainty from both the scale-type and the point-to-point. The scale-type uncertainties were included as an overall scaling factor in the total error bar. In the case of the point-to-point type, the total systematic uncertainty is calculated using Eq. 5.1.

Table 5.1: Summary of systematic uncertainties from both the scale-type and the point-to-point type.

Source	δC_x	δC_z	δP
Timing Cuts	4.75×10^{-3}	4.2×10^{-3}	1.26×10^{-3}
Vertex Position	1.49×10^{-2}	1.26×10^{-2}	4.69×10^{-3}
Fiducial Cuts	8.5×10^{-3}	8.5×10^{-3}	4.17×10^{-3}
Confidence Level	1.72×10^{-2}	2.36×10^{-2}	1.09×10^{-2}
$P_\odot$	$0.05 C_x$	$0.05 C_z$	–
α	$0.02 C_x$	$0.02 C_z$	$0.02 P$

CHAPTER 6

FINAL RESULTS AND DISCUSSION

The final results for C_x, C_z, and P with systematic uncertainties will be presented in this chapter. Then, a comparison of the measurement from this analysis will be made with previous results.

6.1 Double polarization C_x and C_z

In the previous chapter, the results from both topologies, two-track and three-track, have been shown to be consistent with each other. This allows us to quote the final results (C_x, C_z, and P) using only the two-track analysis which has better precision.

Figures 6.1 and 6.2 show C_x and C_z as a function of $\cos\theta^{cm}_{K^+}$ for different W bins. All the error bars include both the statistical and the systematic error (point-to-point).

From Figure 6.1, C_x has strong dependency on $\cos\theta^{cm}_{K^+}$, particularly W >2019 MeV. At low W bins, C_x are mostly flat around zero. As for C_z, their values are close to 1, and occasionally exceeds 1 in low W bins as shown in Figure 6.2. For those $C_z > 1$, points are overlapped with $C_z = 1$ after adding the point-to-point type systematic uncertainty in the error bar.

The production behaviour of $K^+\Lambda$ seems more obvious in the energy dependent plots such as Figures 6.3 and 6.4 where the results plotted as a function of W for C_x and C_z at constant $\cos\theta^{cm}_{K^+}$. The s-channel resonance production is more prominant in low energy region where both C_x and C_z results are fluctuating, specifically at backward angles for C_z, and backward and mid-angle for C_x. In the high energy region, the t-channel production dominates which is clearly seen in Figures 6.3 and

6.4 where both C_x and C_z flatten out above about 2.6 GeV in the forward angle bins and 2.8 GeV in backward angle bins.

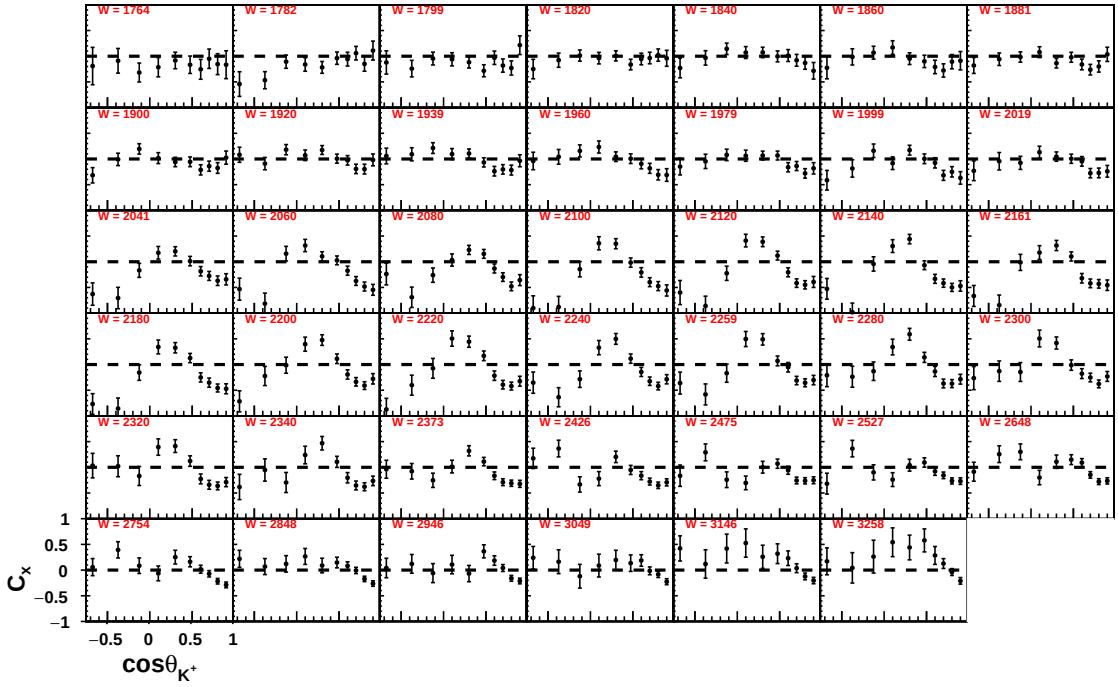

Figure 6.1: C_x as a function of $\cos\theta^{cm}_{K^+}$ for different W bins. A W bin reported in each plot is an average value calculated for total events within the bin range. The error bar on each data point includes statistical and point-to-point systematic error.

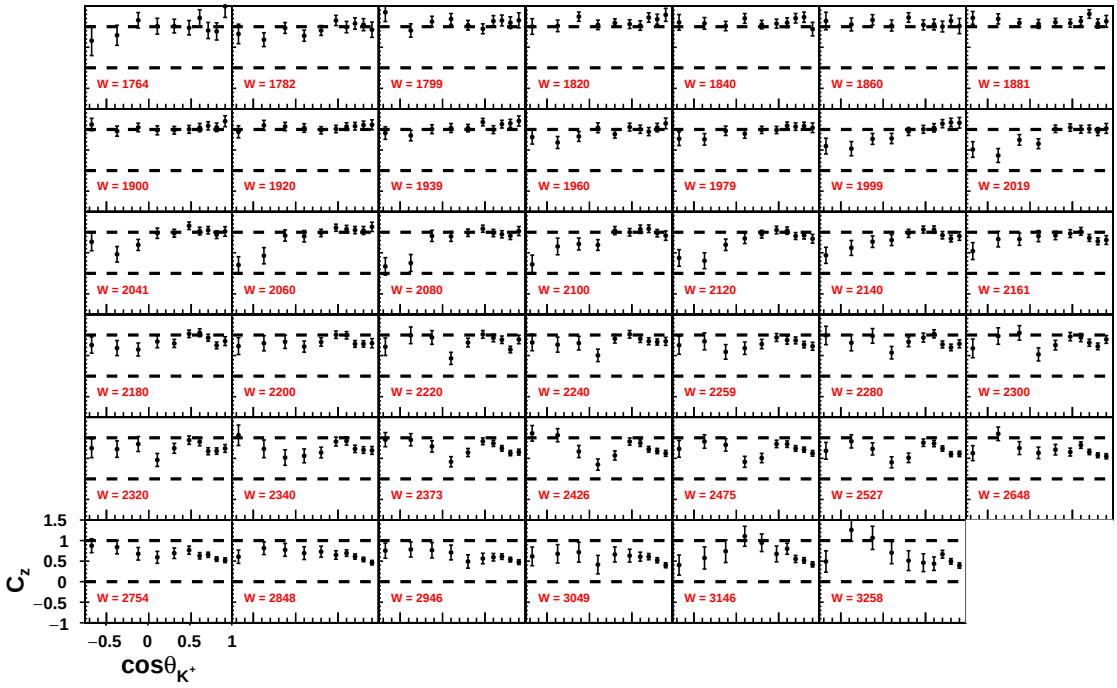

Figure 6.2: C_z as a function of $\cos\theta^{cm}_{K^+}$ for different W bins. A W bin reported in each plot is an average value calculated for total events within the bin range. The error bar on each data point includes statistical and point-to-point systematic error.

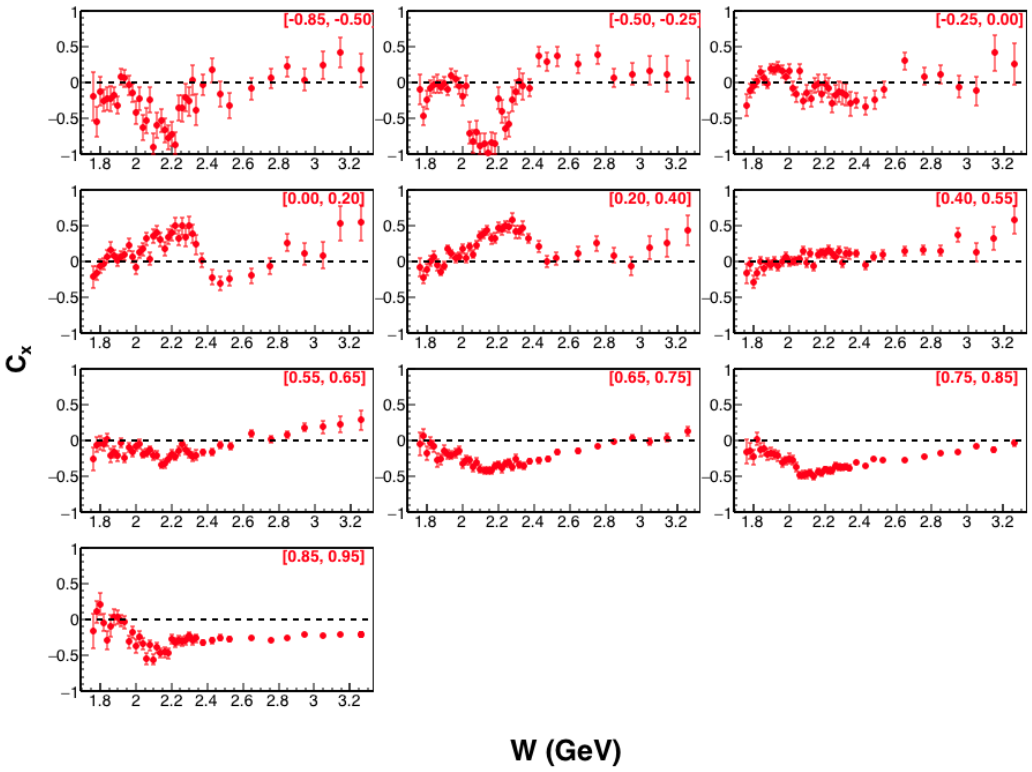

Figure 6.3: C_x as a function of W for the Λ hyperon in the energy range of $W \in \{1.75, 3.33\}$ GeV and $\cos\theta^{cm}_{K^+}$ bin as indicated in the plots.

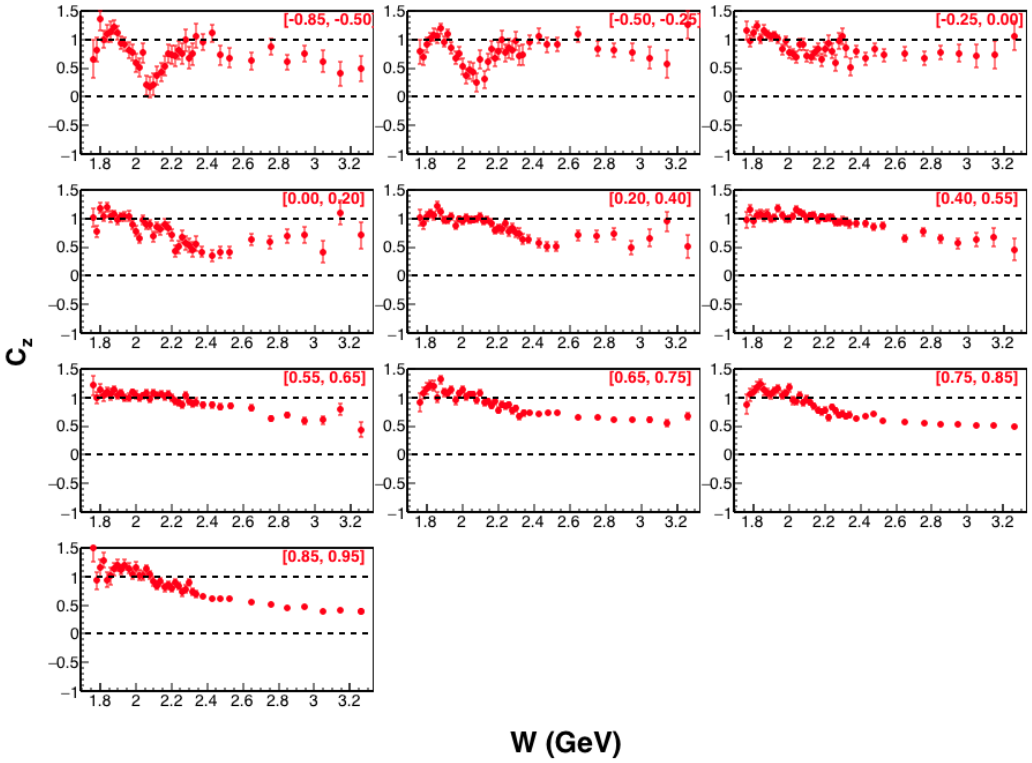

Figure 6.4: C_z as a function of W for the Λ hyperon in the energy range of $W \in \{1.75, 3.33\}$ GeV and $\cos\theta^{cm}_{K^+}$ bin as indicated in the plots.

Comparison with previous measurement

Figures 6.5 and 6.6 show the C_x and C_z results from the current analysis (red) and the previous *g1c* CLAS measurement at Jefferson Lab (black) [26], as a function of W at constant $\cos\theta^{cm}_{K^+}$. These C_x and C_z measurements show excellent agreement with *g1c* results and offer more data points with better precision within the overlap region and a 800 Mev increase in W coverage.

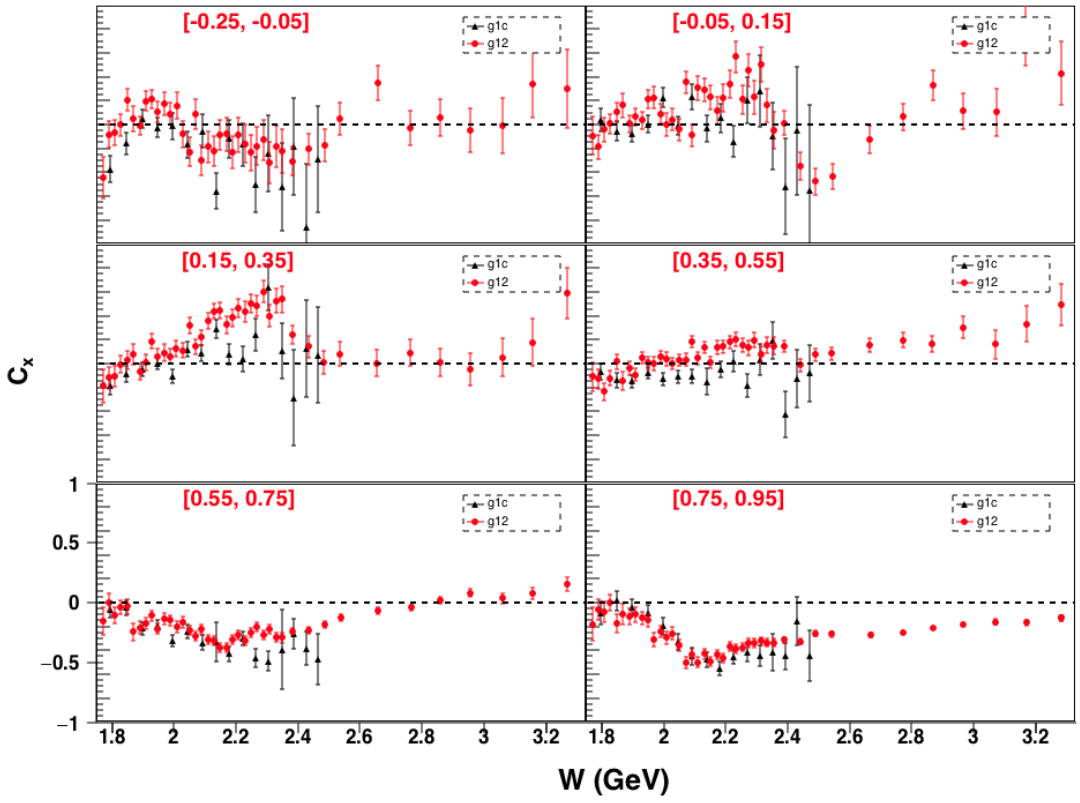

Figure 6.5: C_x vs W; plotted for the *g12* and the *g1c* in the same $\cos\theta^{cm}_{K^+}$ bin. The current measurement (red) overlapped and extends in W bins compared to previous measurement (black).

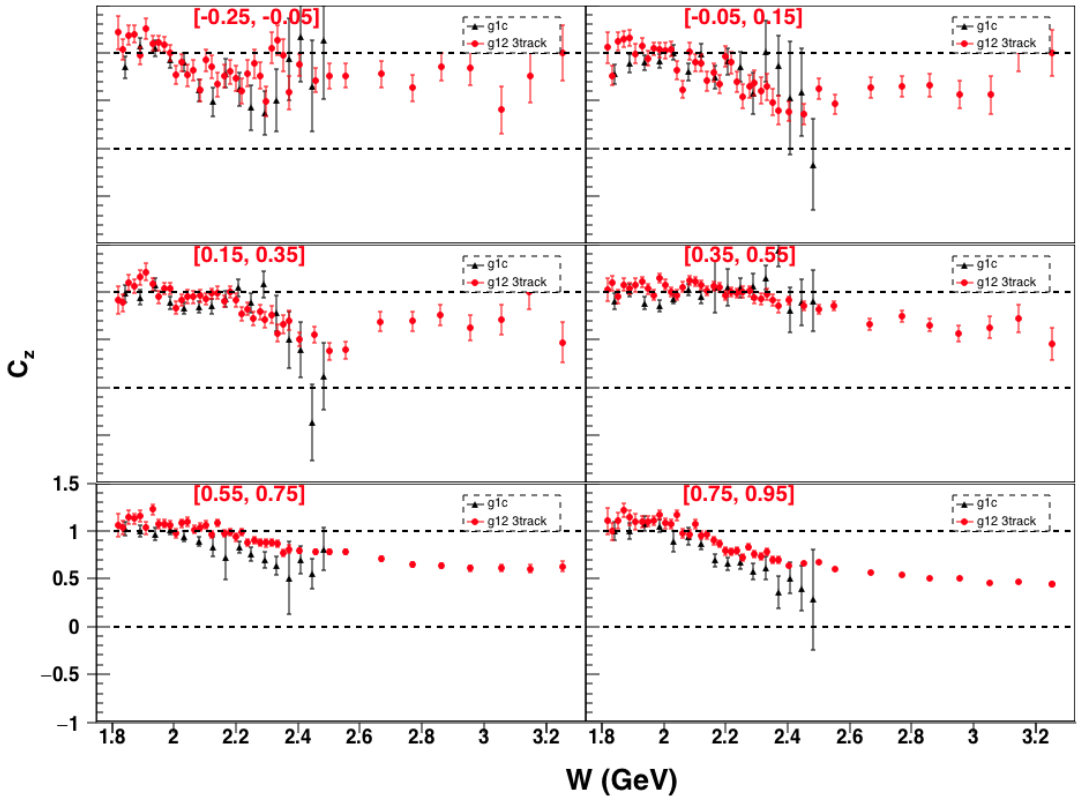

Figure 6.6: C_z vs W; plotted for the *g12* and the *g1c* in the same $\cos\theta^{cm}_{K^+}$ bin. The current measurement (red) overlapped and extends in W bins compared to previous measurement (black).

6.2 Recoil polarization P

Similar to C_x and C_z, the P observable also presents an interesting opportunity for interpretation of $K^+\Lambda$ production mechanisms. In Figure 6.7 P results are shown as a function of $\cos\theta^{cm}_{K^+}$ for various W bins. Overall the P values are varying from backward to forward angle bins. However, it is diffcult to interpret the angular dependence plots without comparison to calculation. Figure 6.8 shows the P observable ranging in W from 1.75 to 3.33 GeV. At low energies, the structure in P values could be due to s-channel production of various intermediate N^* states. In the high energy region, where t-channel production process become dominant, P values seem to flatten out.

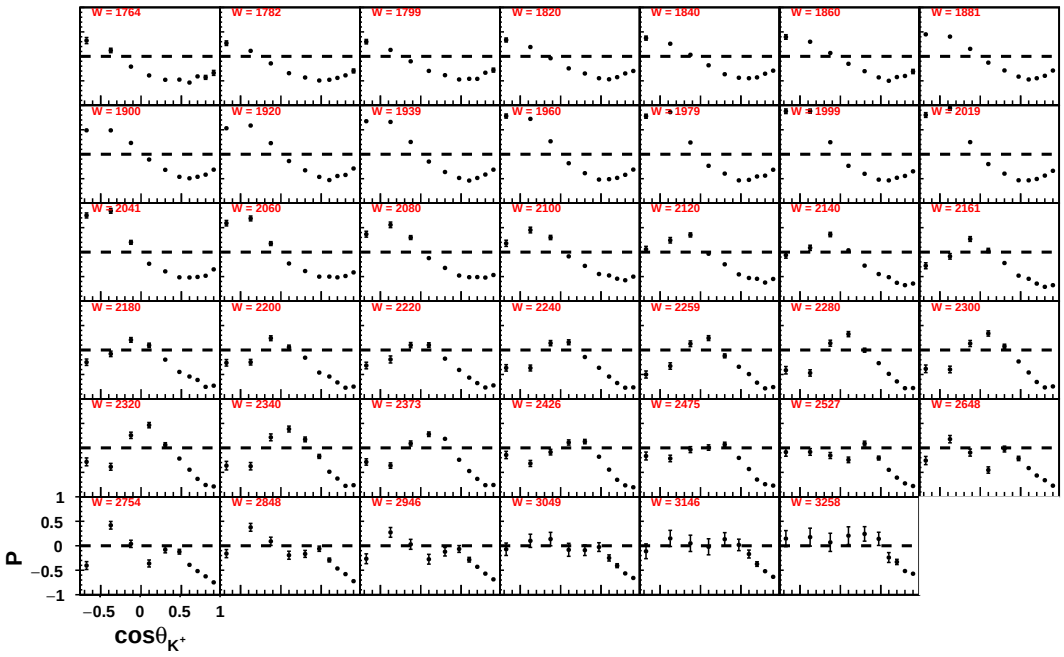

Figure 6.7: P as a function of $\cos\theta^{cm}_{K^+}$ for different W bins. A W bin reported in each plot is an average value calculated for total events within the bin range. The error bar on each data point includes statistical and point-to-point systematic error.

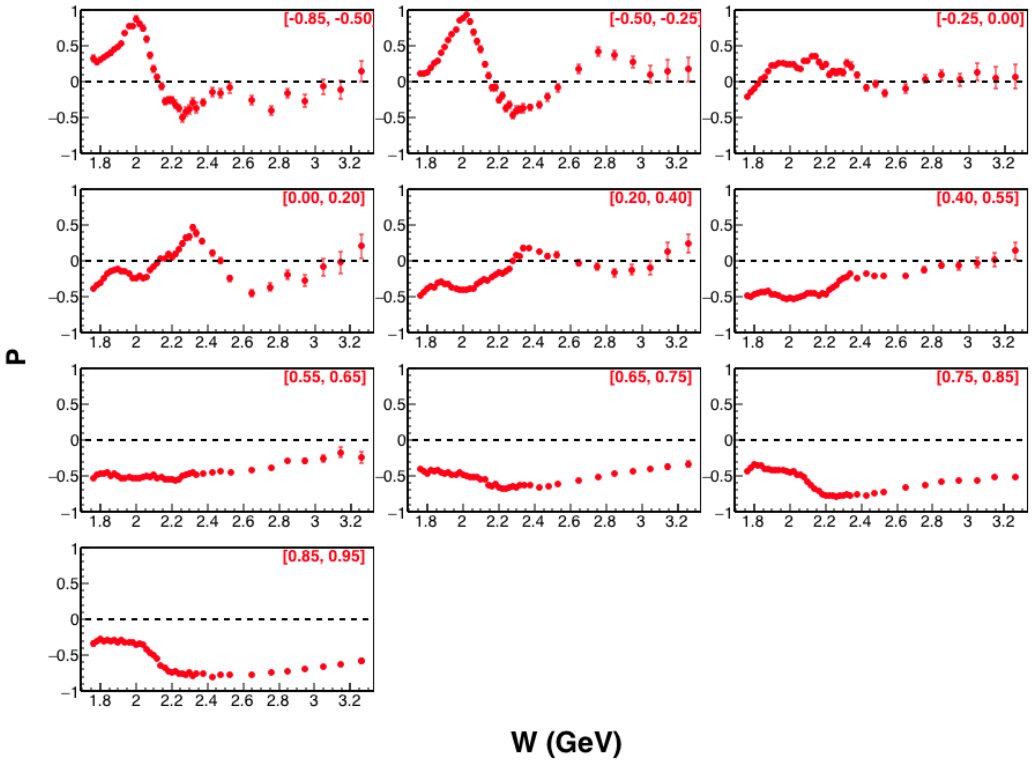

Figure 6.8: C_x as a function of W for the Λ hyperon in the energy range of $W \in \{1.75, 3.33\}$ GeV.

Comparison with previous measurement

Figure 6.9 shows the comparison of the current measurement with the *g11* measurement from the `CLAS` experiment [46]. Results include P vs W for different $\cos\theta^{cm}_{K^+}$ bins. The *g12* data agree well with previous results and offer a 500 MeV extension in energy range.

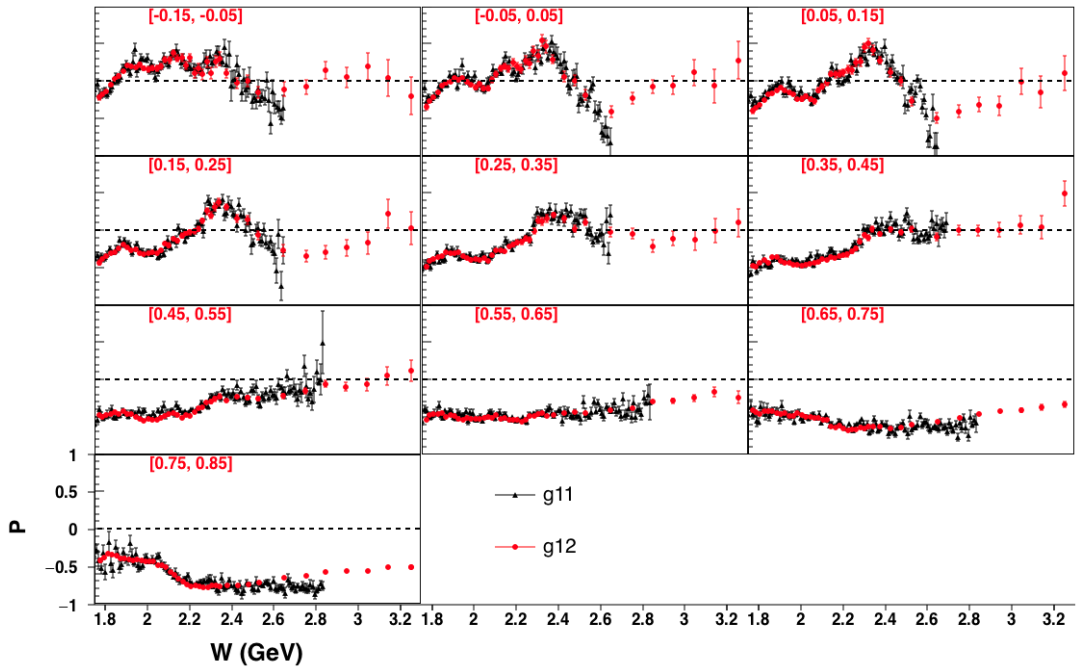

Figure 6.9: P vs W; plotted for the *g12* and the *g11* in the same $\cos\theta^{cm}_{K^+}$ bin. The current measurement (red) overlapped and extends in W bins compared to previous measurement (black).

6.3 Conclusion

Study of the excited-state nucleon have been long established as an essential tool to understand quantum chromodynamics in the non-perturbative region. However, even after decades of study, not all the resonances predicted by different theoretical approaches have been verified. This situation is known as the "missing baryon problem." In recent years, new experiments such as `CLAS` in Jefferson Lab, `ELSA` in Bonn, `MAMI` in Mainz and so on, provides high-precision photoproduction data for different final-state channels. These new data, along with pre-existing data (pion beam data) can be used together to understand missing states better, employing framework such as the Bonn-Gatchina coupled-channel analysis. The excited states are broad and overlapping, and very hard to disentangle using cross section results alone. Therefore, it is crucial to extract polarization observables in order to disentangle these overlapped states.

Existing data on pseudoscalar photoproduction for the $K^+\Lambda$ channel shows a glimpse of which of the missing resonances are coupled to it. Also, the suggestion from the coupled channel analysis of studying multiple channels [77] permits an ubiquitous solution to the missing baryon puzzle. Recently the coupled-channel approach extended to $K^+\Lambda$ along with πN, and other KY channels were analyzed simultaneously [77]. The improvement to understand the pre-existing states such as $N(1710)1/2^+$ and $N(1720)1/2^+$ were made by including the $K^+\Lambda$ channel [47]. Also, new states were added, such as $N(1900)3/2^+$ that was not seen through other channels. The current analysis also includes more data in the existing database for transferred and induced polarization observables for the Λ hyperon from `CLAS`'s *g12* experiment. The measurement was done at an extended center-of-mass energy (W) up to 3.33 GeV. The results presented here for double polarization observables, C_x

and C_z, are the first ever measurement for $W > 2.5$ GeV. For P the results are also first time measurement for $W > 2.84$ GeV. The high energy data provide a constraint on non-resonant processes.

To understand the part of the contribution to resonance production from $K^+\Lambda$, the refined understanding of background processes, such as t-channel and u-channel, are important. This analysis offers a first major step towards that goal. In the future, the current results for polarization observables will be compared with theoretical prediction. Our results show good agreement with previous measurements. We hope our results will provide a substantial basis for development in the understanding of quantum chromodynamics.

Bibliography

[1] J.J. Thomson. Cathode rays. *Philosophical Magazine*, 90(sup1):25–29, 2010.

[2] E. Rutherford. The scattering of α and β particles by matter and the structure of the atom. *Phil. Mag.*, 21:669–688, may 1911.

[3] I. Estermann, O. C. Simpson, and O. Stern. The magnetic moment of the proton. *Phys. Rev.*, 52(6):535–545, Sep 1937.

[4] M. Gell-Mann. A schematic model of baryons and mesons. *Physics Letters*, 8(3):214 – 215, 1964.

[5] Wikipedia contributors. Standard model — Wikipedia, the free encyclopedia, 2018. [Online; accessed 11-September-2018].

[6] David J. Gross and Frank Wilczek. Ultraviolet behavior of non-abelian gauge theories. *Phys. Rev. Lett.*, 30:1343–1346, Jun 1973.

[7] H. David Politzer. Reliable perturbative results for strong interactions? *Phys. Rev. Lett.*, 30:1346–1349, Jun 1973.

[8] S. Bethke. Experimental tests of asymptotic freedom. *Progress in Particle and Nuclear Physics*, 58(2):351 – 386, 2007.

[9] Kenneth G. Wilson. Confinement of quarks. *Phys. Rev. D*, 10:2445–2459, Oct 1974.

[10] G. Zweig. Cern preprint 8419/th412, 8182/th401.

[11] M. Tanabashi et al. Review of Particle Physics. *Phys. Rev. D*, 98:030001, 2018.

[12] Simon Capstick and W. Roberts. Strange decays of nonstrange baryons. *Phys. Rev. D*, 58:074011, Sep 1998.

[13] S. Capstick and W. Roberts. Quark models of baryon masses and decays. *Progress in Particle and Nuclear Physics*, 45(Supplement 2):S241 – S331, 2000.

[14] V Crede and W Roberts. Progress towards understanding baryon resonances. *Reports on Progress in Physics*, 76(7):076301, 2013.

[15] J. Ferretti, A. Vassallo, and E. Santopinto. Relativistic quark-diquark model of baryons. *Phys. Rev. C*, 83:065204, Jun 2011.

[16] Robert G Edwards, Jozef J Dudek, David G Richards, and Stephen J Wallace. Excited state baryon spectroscopy from lattice qcd. *Physical Review D*, 84(7):074508, 2011.

[17] Simon Capstick and W. Roberts. Strange decays of nonstrange baryons. *Phys. Rev.*, D58:074011, 1998.

[18] K.A. Olive et al. Review of particle physics. *Phys. Rev. C*, 38:090001, 2014.

[19] Jean Tate. "atomic spectra", originally published on universe today.

[20] I. S. Barker, A. Donnachie, and J. K. Storrow. Complete Experiments in Pseudoscalar Photoproduction. *Nucl. Phys.*, B95:347–356, 1975.

[21] Wen-Tai Chiang and Frank Tabakin. Completeness rules for spin observables in pseudoscalar meson photoproduction. *Phys. Rev.*, C55:2054–2066, 1997.

[22] G. F. Chew, M. L. Goldberger, F. E. Low, and Yoichiro Nambu. Relativistic dispersion relation approach to photomeson production. *Phys. Rev.*, 106:1345–1355, 1957.

[23] C. G. Fasano, Frank Tabakin, and Bijan Saghai. Spin observables at threshold for meson photoproduction. *Phys. Rev. C*, 46:2430–2455, Dec 1992.

[24] Greg Keaton and Ron Workman. Amplitude ambiguities in pseudoscalar meson photoproduction. *Phys. Rev. C*, 53:1434–1436, Mar 1996.

[25] C. A. Paterson et al. Photoproduction of Λ and Σ^0 hyperons using linearly polarized photons. *Phys. Rev. C*, 93:065201, Jun 2016.

[26] R. K. Bradford et al. First measurement of beam-recoil observables C_x and C_z in hyperon photoproduction. *Phys. Rev.*, C75:035205, 2007.

[27] P. L. Donoho and R. L. Walker. Photoproduction of K^+ Mesons in Hydrogen. *Phys. Rev.*, 112:981–986, 1958.

[28] B. D. McDaniel, A. Silverman, R. R. Wilson, and G. Cortellessa. Photoproduction of K^+ Mesons. *Phys. Rev.*, 115:1039–1048, 1959.

[29] R. L. Anderson, E. Gabathuler, D. Jones, B. D. McDaniel, and A. J. Sadoff. Photoproduction of K^+ mesons in hydrogen. *Phys. Rev. Lett.*, 9:131–133, Aug 1962.

[30] Charles W. Peck. $K^+\Lambda$ Photoproduction from Hydrogen at 1200 MeV. *Phys. Rev.*, 135:B830–B838, 1964.

[31] D. E. Groom and J. H. Marshall. Λ polarization at 90° in $K^+\Lambda$ photoproduction. *Phys. Rev.*, 159:1213–1219, Jul 1967.

[32] R. Erbe et al. Multipion and strange-particle photoproduction on protons at energies up to 5.8-GeV. *Phys. Rev.*, 188:2060–2077, 1969.

[33] A. Boyarski et al. PHOTOPRODUCTION OF $K^+\Lambda$ AND $K^+\Sigma^\circ$ FROM HYDROGEN FROM 5 GeV to 16 Gev. *Phys. Rev. Lett.*, 22:1131–1133, 1969.

[34] A. Bleckmann, S. Herda, U. Opara, W. Schulz, W. J. Schwille, and H. Urbahn. Photoproduction of $K^+\Lambda$ AND $K^+\Sigma^\circ$ from hydrogen between 1.3 and 1.45 GeV. *Z. Phys.*, 239:1–15, 1970.

[35] T. Fujii et al. Photoproduction of K^+ mesons and polarization of Λ hyperons in the 1 gev range. *Phys. Rev.*, D2:439–448, 1970.

[36] H. Goeing, W. Schorsch, J. Tietge, and W. Weilnboeck. Photoproduction of $K^+\Lambda$ and $K^+\Sigma^\circ$ in hydrogen between 1.19 and 1.68 gev. *Nucl. Phys.*, B26:121–133, 1971.

[37] P. Feller, D. Menze, U. Opara, W. Schulz, and W. J. Schwille. Photoproduction of $K^+\Lambda$ and $K^+\Sigma^\circ$ from hydrogen at constant momentum transfer t between 1.05 and 2.2 gev. *Nucl. Phys.*, B39:413–420, 1972.

[38] Robert L. Anderson, D. Gustavson, D. Ritson, G. A. Weitsch, H. J. Halpern, R. Prepost, D. H. Tompkins, and D. E. Wiser. Measurements of Exclusive Photoproduction Processes at Large Values of t and u from 4 GeV to 7.5 GeV. *Phys. Rev.*, D14:679, 1976.

[39] M. Bockhorst et al. Measurement of $\gamma p \to K^+\Lambda$ and $\gamma p \to K^+\Sigma^\circ$ at photon energies up to 1.47-GeV. *Z. Phys.*, C63:37–47, 1994.

[40] M.Q. Tran et al. Measurement of $\gamma p \to k^+\lambda$ and $\gamma p \to k^+\sigma^\circ$ at photon energies up to 2 gev. *Physics Letters B*, 445(1):20 – 26, 1998.

[41] K. H. Glander et al. Measurement of $\gamma p \to K^+\Lambda$ and $\gamma p \to K^+\Sigma^0$ at photon energies up to 2.6 GeV. *Eur. Phys. J.*, A19:251–273, 2004.

[42] J. W. C. McNabb et al. Hyperon photoproduction in the nucleon resonance region. *Phys. Rev.*, C69:042201, 2004.

[43] R. Bradford et al. Differential cross sections for $\gamma + p \to K^+ + Y$ for Λ and Σ^0 hyperons. *Phys. Rev.*, C73:035202, 2006.

[44] M. Sumihama et al. The Polarized $\gamma p \to K^+\Lambda$ and $\gamma p \to K^+\Sigma^\circ$ reactions at forward angles with photon energies from 1.5-GeV to 2.4-GeV. *Phys. Rev.*, C73:035214, 2006.

[45] K. Hicks et al. Measurement of the polarized $\gamma p \to K^+\Lambda$ reaction at backward angles. *Phys. Rev.*, C76:042201, 2007.

[46] M. E. McCracken et al. Differential cross section and recoil polarization measurements for the $\gamma p \to K^+\Lambda$ reaction using CLAS at Jefferson Lab. *Phys. Rev.*, C81:025201, 2010.

[47] A. V. Anisovich, V. Kleber, E. Klempt, V. A. Nikonov, A. V. Sarantsev, and U. Thoma. Baryon resonances and polarization transfer in hyperon photoproduction. *Eur. Phys. J.*, A34:243–254, 2007.

[48] CEBAF 2013_v2. `https://www.flickr.com/photos/jeffersonlab/12614907725/`. Accessed: 2013-06-12.

[49] Jefferson lab picture exchange. http://www.jlab.org.

[50] H. Olsen and L. C. Maximon. Photon and electron polarization in high-energy bremsstrahlung and pair production with screening. *Phys. Rev.*, 114:887–904, 1959.

[51] Sober D. I. et al. The bremsstrahlung tagged photon beam in Hall `B` at JLab. *Nucl. Instr. and Meth. A*, 440:263–284, 2000.

[52] B. Mecking *et al.* The CEBAF large acceptance spectrometer (CLAS). *Nucl. Instrum. Methods A 503, 513*, 2003.

[53] S. Christo. The `g11a` target cell.

[54] Y. G. Sharabian et al. A new highly segmented start counter for the `CLAS` detector. *Nucl. Instr. and Meth. A*, 556:246–258, 2006.

[55] B. A. Mecking et al. The `CEBAF` Large Acceptance Spectrometer (`CLAS`). *Nucl. Instr. and Meth. A*, 503:513, 2003.

[56] Steve Gagnon. Jefferson lab site tour. `https://education.jlab.org/sitetour/hallbin02.l.html`.

[57] M. Mestayer et al. The clas drift chamber system. *Nucl. Instr. and Meth. A*, 449:81–111, 2000.

[58] E. S. Smith et al. The time-of-flight system for `CLAS`. *Nucl. Instr. and Meth. A*, 432:265–298, 1999.

[59] G. Adams et al. The CLAS cherenkov detector. *Nucl. Instr. and Meth. A*, 465, 2001.

[60] M. Amarian et al. The CLAS forward electromagnetic calorimeter. *Nucl. Instr. and Meth. A*, 460, 2001.

[61] J. T. Goetz. *Ξ Hyperon Photoproduction from Threshold to 5.4 GeV with the `CEBAF` Large Acceptance Spectrometer.* PhD thesis, University of California Los Angeles, 2010.

[62] M. C. Kunkel. *Photoproduction of π^0 on hydrogen with `CLAS` from 1.1 GeV - 5.45 GeV using $e^+e\gamma$ decay.* PhD thesis, Old Dominion University, 2014.

[63] Jason Bono. *First Time Measurements of Polarization Observables for the Charged Cascade Hyperon in Photoproduction.* PhD thesis, Florida International University, 2014.

[64] g12 working group. g12 analysis procedures, statistics and systematics. *CLAS-NOTE*, 2017-002.

[65] E. Pasyuk. Energy loss corrections for charged particles in clas. *CLAS-NOTE*, 2007-016.

[66] K. Hicks D. Keller. Techniques in kinematic fitting. *CLAS-NOTE*, 2010-1.

[67] M Williams and C.A. Meyer. Kinematic fitting in clas. *CLAS-NOTE*, 2003-017.

[68] Wouter Verkerke and David P. Kirkby. The RooFit toolkit for data modeling. *eConf*, C0303241:MOLT007, 2003. [,186(2003)].

[69] Mike Williams. *Measurement of Differential Cross Sections and Spin Density Matrix Elements along with a Partial Wave Analysis for $\gamma p \to p\omega$ using* `CLAS` *at Jefferson Lab.* PhD thesis, Carnegie Mellon University, 2007.

[70] M. Williams, M. Bellis, and C. A. Meyer. Multivariate side-band subtraction using probabilistic event weights. *JINST*, 4:P10003, 2009.

[71] Haakon Olsen and L. C. Maximon. Photon and electron polarization in high-energy bremsstrahlung and pair production with screening. *Phys. Rev.*, 114:887–904, May 1959.

[72] D. S. Carman et al. First measurement of transferred polarization in the $\gamma p \to K^+\Lambda$ in polarized-Lambda reaction. *Phys. Rev. Lett.*, 90:131804, 2003.

[73] J. Bono et al. First measurement of Ξ^- polarization in photoproduction. *Phys. Lett.*, B783:280–286, 2018.

[74] D.G. Ireland. Extracting polarization observables in pseudoscalar photoproduction reactions. *CLAS-NOTE*, 2011-011 (2011).

[75] F. James and M. Roos. Minuit - a system for function minimization and analysis of the parameter errors and correlations. *Computer Physics Communications*, 10(6):343 – 367, 1975.

[76] F. James. MINUIT Function Minimization and Error Analysis: Reference Manual Version 94.1. 1994.

[77] A. V. Anisovich, R. Beck, E. Klempt, V. A. Nikonov, A. V. Sarantsev, and U. Thoma. Properties of baryon resonances from a multichannel partial wave analysis. *Eur. Phys. J.*, A48:15, 2012.

A APPENDIX

A.1 Data Table: C_x, C_z, and P for $K^+\Lambda$

This appendix contains table of numberical values for C_x, C_z, and P for the $K^+\Lambda$ analysis. The table consists of fourteen columns, which are interpreted as follows:

- Column 1: Lower limit of W bin (GeV).
- Column 2: Nominal midpoint of W bin (GeV).
- Column 3: Weighted average of W bin (GeV).
- Column 4: Upper limit of W bin (GeV).
- Column 5: Lower limit of $\cos\theta^{cm}_{K^+}$ bin.
- Column 6: Midpoint of $\cos\theta^{cm}_{K^+}$ bin.
- Column 7: Weighted average of $\cos\theta^{cm}_{K^+}$ bin.
- Column 8: Upper limit of $\cos\theta^{cm}_{K^+}$ bin.
- Column 9: C_x.
- Column 10: δC_x.
- Column 11: P.
- Column 12: δP.
- Column 13: C_z.
- Column 14: δC_z.

The error in the polarization observables include statistical error only.

1.75	1.76	1.7645	1.77	-0.85	-0.675	-0.6063	-0.50	-0.1916	0.3337	0.3227	0.0486	0.6600	0.3288
1.75	1.76	1.7644	1.77	-0.50	-0.375	-0.3559	-0.25	-0.0893	0.2098	0.1205	0.0312	0.7907	0.2103
1.75	1.76	1.7645	1.77	-0.25	-0.125	-0.1194	0.00	-0.3179	0.1539	-0.2101	0.0232	1.1562	0.1543
1.75	1.76	1.7644	1.77	0.00	0.100	0.1012	0.20	-0.2144	0.1573	-0.3899	0.0239	1.0120	0.1595
1.75	1.76	1.7645	1.77	0.20	0.300	0.3111	0.40	-0.0832	0.1308	-0.4789	0.0192	1.0152	0.1328
1.75	1.76	1.7644	1.77	0.40	0.475	0.4708	0.55	-0.1661	0.1392	-0.4753	0.0205	0.9757	0.1411
1.75	1.76	1.7645	1.77	0.55	0.600	0.6026	0.65	-0.2550	0.1631	-0.5356	0.0237	1.2119	0.1666
1.75	1.76	1.7644	1.77	0.65	0.700	0.6992	0.75	-0.0492	0.1581	-0.4093	0.0239	0.9075	0.1624
1.75	1.76	1.7644	1.77	0.75	0.800	0.7970	0.85	-0.1549	0.1733	-0.4297	0.0259	0.8857	0.1760
1.75	1.76	1.7645	1.77	0.85	0.900	0.8901	0.95	-0.1654	0.2410	-0.3379	0.0368	1.4944	0.2346
1.77	1.78	1.7818	1.79	-0.85	-0.675	-0.6048	-0.50	-0.5421	0.2099	0.2693	0.0331	0.8240	0.2034
1.77	1.78	1.7818	1.79	-0.50	-0.375	-0.3563	-0.25	-0.4671	0.1360	0.1124	0.0209	0.6847	0.1345

1.77	1.78	1.7818	1.79	-0.25	-0.125	-0.1174	0.00	-0.1068	0.0982	-0.1440	0.0156	0.9688	0.0984
1.77	1.78	1.7818	1.79	0.00	0.100	0.1004	0.20	-0.1608	0.1013	-0.3440	0.0160	0.7803	0.1021
1.77	1.78	1.7818	1.79	0.20	0.300	0.3112	0.40	-0.2175	0.0847	-0.4320	0.0131	0.9075	0.0862
1.77	1.78	1.7818	1.79	0.40	0.475	0.4718	0.55	-0.0380	0.0902	-0.4933	0.0139	1.1512	0.0907
1.77	1.78	1.7818	1.79	0.55	0.600	0.6018	0.65	-0.0569	0.1040	-0.4785	0.0161	0.9908	0.1048
1.77	1.78	1.7818	1.79	0.65	0.700	0.6994	0.75	0.0589	0.1018	-0.4403	0.0159	1.0784	0.1037
1.77	1.78	1.7818	1.79	0.75	0.800	0.7976	0.85	-0.1498	0.1119	-0.3883	0.0176	1.0497	0.1133
1.77	1.78	1.7817	1.79	0.85	0.900	0.8886	0.95	0.1094	0.1543	-0.2980	0.0257	0.9266	0.1525
1.79	1.80	1.7993	1.81	-0.85	-0.675	-0.6022	-0.50	-0.1222	0.1958	0.3000	0.0314	1.3500	0.1905
1.79	1.80	1.7991	1.81	-0.50	-0.375	-0.3558	-0.25	-0.2420	0.1308	0.1316	0.0206	0.9078	0.1295
1.79	1.80	1.7992	1.81	-0.25	-0.125	-0.1171	0.00	-0.0453	0.0944	-0.1014	0.0155	1.1248	0.0940
1.79	1.80	1.7992	1.81	0.00	0.100	0.1012	0.20	-0.0602	0.0981	-0.2974	0.0160	1.1874	0.0996
1.79	1.80	1.7992	1.81	0.20	0.300	0.3120	0.40	-0.1181	0.0824	-0.3848	0.0130	1.0358	0.0827
1.79	1.80	1.7992	1.81	0.40	0.475	0.4721	0.55	-0.2836	0.0869	-0.4720	0.0138	0.9489	0.0876
1.79	1.80	1.7992	1.81	0.55	0.600	0.6017	0.65	-0.0308	0.1002	-0.4587	0.0159	1.1357	0.1005
1.79	1.80	1.7992	1.81	0.65	0.700	0.6994	0.75	-0.1817	0.0985	-0.4597	0.0157	1.1501	0.0990
1.79	1.80	1.7992	1.81	0.75	0.800	0.7978	0.85	-0.2295	0.1079	-0.3345	0.0175	1.0976	0.1092
1.79	1.80	1.7991	1.81	0.85	0.900	0.8873	0.95	0.2138	0.1517	-0.2811	0.0263	1.1550	0.1491
1.81	1.82	1.8199	1.83	-0.85	-0.675	-0.5990	-0.50	-0.2499	0.1593	0.3344	0.0265	1.0050	0.1560
1.81	1.82	1.8197	1.83	-0.50	-0.375	-0.3580	-0.25	-0.0776	0.1079	0.1906	0.0178	1.0202	0.1066
1.81	1.82	1.8197	1.83	-0.25	-0.125	-0.1167	0.00	0.0130	0.0786	-0.0383	0.0132	1.2451	0.0783
1.81	1.82	1.8196	1.83	0.00	0.100	0.1006	0.20	-0.0375	0.0822	-0.2456	0.0137	1.0446	0.0825
1.81	1.82	1.8197	1.83	0.20	0.300	0.3117	0.40	0.0070	0.0687	-0.3501	0.0112	1.0904	0.0686
1.81	1.82	1.8196	1.83	0.40	0.475	0.4725	0.55	-0.1625	0.0732	-0.4470	0.0121	1.0625	0.0727
1.81	1.82	1.8197	1.83	0.55	0.600	0.6011	0.65	-0.0545	0.0829	-0.4686	0.0136	1.0280	0.0819
1.81	1.82	1.8198	1.83	0.65	0.700	0.6992	0.75	-0.0349	0.0821	-0.4253	0.0137	1.2228	0.0809
1.81	1.82	1.8197	1.83	0.75	0.800	0.7979	0.85	0.0220	0.0890	-0.3491	0.0149	1.1812	0.0884
1.81	1.82	1.8196	1.83	0.85	0.900	0.8881	0.95	-0.0410	0.1251	-0.2985	0.0227	1.2882	0.1243
1.83	1.84	1.8403	1.85	-0.85	-0.675	-0.5995	-0.50	-0.2290	0.1615	0.3728	0.0273	1.1046	0.1568
1.83	1.84	1.8402	1.85	-0.50	-0.375	-0.3589	-0.25	-0.0325	0.1102	0.2579	0.0186	1.0809	0.1082
1.83	1.84	1.8401	1.85	-0.25	-0.125	-0.1163	0.00	0.1444	0.0802	0.0320	0.0140	1.0160	0.0805
1.83	1.84	1.8400	1.85	0.00	0.100	0.1004	0.20	0.0714	0.0855	-0.1828	0.0146	1.2017	0.0852
1.83	1.84	1.8402	1.85	0.20	0.300	0.3116	0.40	0.0733	0.0713	-0.3653	0.0119	1.0513	0.0701
1.83	1.84	1.8401	1.85	0.40	0.475	0.4733	0.55	-0.0035	0.0762	-0.4372	0.0128	1.0752	0.0746
1.83	1.84	1.8401	1.85	0.55	0.600	0.6008	0.65	0.0132	0.0855	-0.4469	0.0145	1.0980	0.0839
1.83	1.84	1.8402	1.85	0.65	0.700	0.6991	0.75	-0.0795	0.0847	-0.4297	0.0143	1.2061	0.0827
1.83	1.84	1.8402	1.85	0.75	0.800	0.7985	0.85	-0.1310	0.0929	-0.3547	0.0158	1.2310	0.0907
1.83	1.84	1.8401	1.85	0.85	0.900	0.8896	0.95	-0.2839	0.1312	-0.2922	0.0241	0.9410	0.1310
1.85	1.86	1.8599	1.87	-0.85	-0.675	-0.5999	-0.50	-0.2251	0.1848	0.3961	0.0324	1.1375	0.1792
1.85	1.86	1.8601	1.87	-0.50	-0.375	-0.3592	-0.25	-0.0131	0.1277	0.2986	0.0222	1.0546	0.1250
1.85	1.86	1.8599	1.87	-0.25	-0.125	-0.1163	0.00	0.0687	0.0950	0.0681	0.0171	1.1653	0.0945
1.85	1.86	1.8600	1.87	0.00	0.100	0.0997	0.20	0.1692	0.1015	-0.1521	0.0180	1.0284	0.1010
1.85	1.86	1.8600	1.87	0.20	0.300	0.3112	0.40	-0.0478	0.0840	-0.3031	0.0145	1.2226	0.0823
1.85	1.86	1.8599	1.87	0.40	0.475	0.4747	0.55	-0.1010	0.0902	-0.4299	0.0156	1.0437	0.0883
1.85	1.86	1.8600	1.87	0.55	0.600	0.6011	0.65	-0.2088	0.1004	-0.4992	0.0177	1.0531	0.0979
1.85	1.86	1.8599	1.87	0.65	0.700	0.6989	0.75	-0.2776	0.0990	-0.4232	0.0177	1.0033	0.0970
1.85	1.86	1.8600	1.87	0.75	0.800	0.7978	0.85	-0.1067	0.1085	-0.4007	0.0192	1.1409	0.1065
1.85	1.86	1.8601	1.87	0.85	0.900	0.8895	0.95	-0.0881	0.1484	-0.3097	0.0289	1.0158	0.1519
1.87	1.88	1.8809	1.89	-0.85	-0.675	-0.5985	-0.50	-0.1806	0.1244	0.4496	0.0232	1.2139	0.1225
1.87	1.88	1.8808	1.89	-0.50	-0.375	-0.3610	-0.25	-0.0586	0.0917	0.4035	0.0164	1.1900	0.0896
1.87	1.88	1.8808	1.89	-0.25	-0.125	-0.1173	0.00	-0.0157	0.0704	0.1530	0.0130	1.0903	0.0691
1.87	1.88	1.8807	1.89	0.00	0.100	0.1002	0.20	0.0787	0.0754	-0.1285	0.0137	1.0675	0.0750
1.87	1.88	1.8807	1.89	0.20	0.300	0.3113	0.40	-0.1364	0.0623	-0.2877	0.0112	1.1075	0.0607
1.87	1.88	1.8807	1.89	0.40	0.475	0.4759	0.55	-0.0206	0.0665	-0.4138	0.0120	1.0853	0.0645
1.87	1.88	1.8807	1.89	0.55	0.600	0.6007	0.65	-0.1604	0.0735	-0.4721	0.0133	1.1357	0.0713
1.87	1.88	1.8808	1.89	0.65	0.700	0.6992	0.75	-0.2620	0.0729	-0.4473	0.0134	1.3096	0.0708
1.87	1.88	1.8807	1.89	0.75	0.800	0.7972	0.85	-0.1996	0.0796	-0.3973	0.0145	1.0779	0.0770
1.87	1.88	1.8808	1.89	0.85	0.900	0.8902	0.95	0.0361	0.1082	-0.2896	0.0216	1.1304	0.1099
1.89	1.90	1.8995	1.91	-0.85	-0.675	-0.5998	-0.50	-0.3174	0.1189	0.4891	0.0226	1.1203	0.1168
1.89	1.90	1.8995	1.91	-0.50	-0.375	-0.3634	-0.25	-0.0082	0.0904	0.4879	0.0166	0.9594	0.0892
1.89	1.90	1.8995	1.91	-0.25	-0.125	-0.1172	0.00	0.1962	0.0705	0.2309	0.0135	1.0491	0.0700
1.89	1.90	1.8996	1.91	0.00	0.100	0.1008	0.20	0.0168	0.0762	-0.1082	0.0142	0.9792	0.0753
1.89	1.90	1.8998	1.91	0.20	0.300	0.3118	0.40	-0.0589	0.0611	-0.3189	0.0112	0.9806	0.0594
1.89	1.90	1.8999	1.91	0.40	0.475	0.4777	0.55	-0.0548	0.0641	-0.4617	0.0119	1.0039	0.0616
1.89	1.90	1.8999	1.91	0.55	0.600	0.6009	0.65	-0.2120	0.0692	-0.4917	0.0132	1.0456	0.0676
1.89	1.90	1.9000	1.91	0.65	0.700	0.6995	0.75	-0.1398	0.0683	-0.4610	0.0130	1.0892	0.0666

1.89	1.90	1.9001	1.91	0.75	0.800	0.7971	0.85	-0.1753	0.0741	-0.4176	0.0139	1.0527	0.0707
1.89	1.90	1.9002	1.91	0.85	0.900	0.8905	0.95	0.0266	0.0979	-0.3152	0.0198	1.2002	0.1000
1.91	1.92	1.9202	1.93	-0.85	-0.675	-0.6004	-0.50	0.0822	0.1169	0.5312	0.0227	0.9440	0.1141
1.91	1.92	1.9199	1.93	-0.50	-0.375	-0.3642	-0.25	-0.0899	0.0898	0.5862	0.0168	1.0999	0.0879
1.91	1.92	1.9200	1.93	-0.25	-0.125	-0.1159	0.00	0.1813	0.0695	0.2268	0.0137	1.0716	0.0683
1.91	1.92	1.9201	1.93	0.00	0.100	0.1018	0.20	0.0720	0.0724	-0.1390	0.0139	1.0353	0.0712
1.91	1.92	1.9202	1.93	0.20	0.300	0.3123	0.40	0.1744	0.0560	-0.3283	0.0106	0.9802	0.0545
1.91	1.92	1.9202	1.93	0.40	0.475	0.4784	0.55	0.0064	0.0579	-0.4630	0.0112	1.0112	0.0561
1.91	1.92	1.9202	1.93	0.55	0.600	0.6012	0.65	-0.0266	0.0619	-0.5276	0.0121	1.0704	0.0602
1.91	1.92	1.9202	1.93	0.65	0.700	0.6997	0.75	-0.1927	0.0609	-0.4448	0.0121	1.0791	0.0591
1.91	1.92	1.9201	1.93	0.75	0.800	0.7973	0.85	-0.1973	0.0651	-0.4232	0.0127	1.1080	0.0625
1.91	1.92	1.9202	1.93	0.85	0.900	0.8900	0.95	-0.0179	0.0851	-0.2915	0.0177	1.1140	0.0868
1.93	1.94	1.9393	1.95	-0.85	-0.675	-0.6012	-0.50	0.0582	0.1224	0.6752	0.0244	0.9135	0.1201
1.93	1.94	1.9392	1.95	-0.50	-0.375	-0.3655	-0.25	0.0915	0.0975	0.6602	0.0189	0.8531	0.0954
1.93	1.94	1.9392	1.95	-0.25	-0.125	-0.1159	0.00	0.2126	0.0745	0.2508	0.0153	1.0071	0.0737
1.93	1.94	1.9392	1.95	0.00	0.100	0.1023	0.20	0.0955	0.0769	-0.1498	0.0153	1.0353	0.0755
1.93	1.94	1.9393	1.95	0.20	0.300	0.3121	0.40	0.1067	0.0580	-0.3630	0.0113	1.0325	0.0562
1.93	1.94	1.9394	1.95	0.40	0.475	0.4796	0.55	-0.0664	0.0591	-0.4846	0.0119	1.1796	0.0572
1.93	1.94	1.9394	1.95	0.55	0.600	0.6012	0.65	-0.2377	0.0635	-0.5380	0.0127	0.9954	0.0618
1.93	1.94	1.9394	1.95	0.65	0.700	0.6998	0.75	-0.2026	0.0622	-0.4850	0.0125	1.1294	0.0600
1.93	1.94	1.9394	1.95	0.75	0.800	0.7971	0.85	-0.2161	0.0665	-0.4149	0.0135	1.1488	0.0638
1.93	1.94	1.9394	1.95	0.85	0.900	0.8892	0.95	-0.0344	0.0864	-0.3151	0.0184	1.2065	0.0903
1.95	1.96	1.9593	1.97	-0.85	-0.675	-0.6021	-0.50	-0.0388	0.1400	0.7805	0.0279	0.8142	0.1359
1.95	1.96	1.9593	1.97	-0.50	-0.375	-0.3651	-0.25	0.0418	0.1133	0.7223	0.0223	0.6830	0.1116
1.95	1.96	1.9594	1.97	-0.25	-0.125	-0.1153	0.00	0.1575	0.0866	0.2643	0.0182	0.8301	0.0857
1.95	1.96	1.9594	1.97	0.00	0.100	0.1031	0.20	0.2330	0.0875	-0.1840	0.0177	1.0415	0.0863
1.95	1.96	1.9596	1.97	0.20	0.300	0.3115	0.40	0.0446	0.0633	-0.3872	0.0128	0.8854	0.0614
1.95	1.96	1.9597	1.97	0.40	0.475	0.4810	0.55	0.0060	0.0643	-0.5174	0.0133	1.0576	0.0618
1.95	1.96	1.9597	1.97	0.55	0.600	0.6013	0.65	-0.0935	0.0684	-0.5098	0.0143	1.0051	0.0664
1.95	1.96	1.9597	1.97	0.65	0.700	0.7000	0.75	-0.1820	0.0668	-0.4831	0.0139	0.9487	0.0652
1.95	1.96	1.9597	1.97	0.75	0.800	0.7977	0.85	-0.3071	0.0707	-0.4208	0.0148	1.0467	0.0685
1.95	1.96	1.9597	1.97	0.85	0.900	0.8884	0.95	-0.3119	0.0927	-0.3136	0.0199	1.1473	0.0962
1.97	1.98	1.9794	1.99	-0.85	-0.675	-0.6033	-0.50	-0.1481	0.1325	0.7770	0.0273	0.7748	0.1317
1.97	1.98	1.9792	1.99	-0.50	-0.375	-0.3659	-0.25	-0.0463	0.1091	0.8598	0.0213	0.7598	0.1071
1.97	1.98	1.9793	1.99	-0.25	-0.125	-0.1149	0.00	0.0796	0.0816	0.2398	0.0173	0.9673	0.0802
1.97	1.98	1.9794	1.99	0.00	0.100	0.1038	0.20	0.0632	0.0785	-0.2364	0.0162	0.8973	0.0769
1.97	1.98	1.9795	1.99	0.20	0.300	0.3103	0.40	0.0668	0.0557	-0.3956	0.0115	0.9894	0.0540
1.97	1.98	1.9795	1.99	0.40	0.475	0.4813	0.55	0.0670	0.0561	-0.5338	0.0118	0.9871	0.0543
1.97	1.98	1.9795	1.99	0.55	0.600	0.6013	0.65	-0.1609	0.0599	-0.5238	0.0127	1.0894	0.0581
1.97	1.98	1.9795	1.99	0.65	0.700	0.7002	0.75	-0.1371	0.0581	-0.4542	0.0124	1.0692	0.0566
1.97	1.98	1.9795	1.99	0.75	0.800	0.7981	0.85	-0.2804	0.0615	-0.4376	0.0130	1.0833	0.0597
1.97	1.98	1.9795	1.99	0.85	0.900	0.8877	0.95	-0.1817	0.0806	-0.3168	0.0175	1.0416	0.0837
1.99	2.00	1.9992	2.01	-0.85	-0.675	-0.6053	-0.50	-0.4142	0.1608	0.8789	0.0332	0.5954	0.1582
1.99	2.00	1.9991	2.01	-0.50	-0.375	-0.3656	-0.25	-0.1849	0.1390	0.8810	0.0275	0.5329	0.1384
1.99	2.00	1.9992	2.01	-0.25	-0.125	-0.1134	0.00	0.1601	0.1009	0.2453	0.0222	0.7711	0.0992
1.99	2.00	1.9993	2.01	0.00	0.100	0.1041	0.20	-0.0821	0.0930	-0.2368	0.0198	0.7810	0.0914
1.99	2.00	1.9993	2.01	0.20	0.300	0.3098	0.40	0.1715	0.0650	-0.3994	0.0137	0.9510	0.0628
1.99	2.00	1.9994	2.01	0.40	0.475	0.4815	0.55	0.0036	0.0644	-0.5193	0.0142	1.0042	0.0624
1.99	2.00	1.9994	2.01	0.55	0.600	0.6014	0.65	-0.0749	0.0699	-0.5343	0.0151	1.0406	0.0674
1.99	2.00	1.9993	2.01	0.65	0.700	0.7004	0.75	-0.3188	0.0669	-0.4811	0.0146	1.1413	0.0654
1.99	2.00	1.9994	2.01	0.75	0.800	0.7984	0.85	-0.2498	0.0704	-0.4433	0.0153	1.1700	0.0687
1.99	2.00	1.9994	2.01	0.85	0.900	0.8865	0.95	-0.3681	0.0916	-0.3491	0.0205	1.1626	0.0954
2.01	2.02	2.0186	2.03	-0.85	-0.675	-0.6052	-0.50	-0.2300	0.1611	0.8015	0.0345	0.5127	0.1564
2.01	2.02	2.0184	2.03	-0.50	-0.375	-0.3654	-0.25	-0.0442	0.1397	0.9397	0.0283	0.3668	0.1358
2.01	2.02	2.0186	2.03	-0.25	-0.125	-0.1109	0.00	-0.0755	0.0977	0.2475	0.0220	0.7469	0.0956
2.01	2.02	2.0186	2.03	0.00	0.100	0.1056	0.20	0.1306	0.0878	-0.2010	0.0192	0.6531	0.0862
2.01	2.02	2.0188	2.03	0.20	0.300	0.3091	0.40	0.0463	0.0604	-0.3962	0.0131	1.0163	0.0581
2.01	2.02	2.0188	2.03	0.40	0.475	0.4820	0.55	0.0051	0.0593	-0.5320	0.0133	1.0469	0.0572
2.01	2.02	2.0189	2.03	0.55	0.600	0.6016	0.65	-0.0464	0.0628	-0.5332	0.0142	1.0036	0.0613
2.01	2.02	2.0188	2.03	0.65	0.700	0.7005	0.75	-0.2763	0.0606	-0.5055	0.0135	1.0149	0.0591
2.01	2.02	2.0188	2.03	0.75	0.800	0.7988	0.85	-0.2711	0.0640	-0.4366	0.0142	0.9481	0.0626
2.01	2.02	2.0189	2.03	0.85	0.900	0.8857	0.95	-0.2396	0.0840	-0.3388	0.0190	1.0257	0.0869
2.03	2.04	2.0403	2.05	-0.85	-0.675	-0.6076	-0.50	-0.5838	0.1640	0.7667	0.0364	0.7284	0.1607
2.03	2.04	2.0403	2.05	-0.50	-0.375	-0.3643	-0.25	-0.7206	0.1445	0.8228	0.0315	0.4633	0.1436
2.03	2.04	2.0404	2.05	-0.25	-0.125	-0.1098	0.00	-0.2049	0.0971	0.2050	0.0230	0.7128	0.0962
2.03	2.04	2.0404	2.05	0.00	0.100	0.1057	0.20	0.1714	0.0854	-0.2300	0.0193	0.9313	0.0836

2.03	2.04	2.0406	2.05	0.20	0.300	0.3077	0.40	0.1948	0.0576	-0.3933	0.0129	0.9593	0.0554
2.03	2.04	2.0406	2.05	0.40	0.475	0.4822	0.55	0.0110	0.0553	-0.5197	0.0129	1.1295	0.0535
2.03	2.04	2.0406	2.05	0.55	0.600	0.6016	0.65	-0.1802	0.0592	-0.5216	0.0137	1.0202	0.0572
2.03	2.04	2.0406	2.05	0.65	0.700	0.7007	0.75	-0.2683	0.0562	-0.5049	0.0129	1.0388	0.0550
2.03	2.04	2.0407	2.05	0.75	0.800	0.7998	0.85	-0.3644	0.0578	-0.4820	0.0133	0.9455	0.0567
2.03	2.04	2.0406	2.05	0.85	0.900	0.8851	0.95	-0.3214	0.0771	-0.3495	0.0179	0.9983	0.0801
2.05	2.06	2.0600	2.07	-0.85	-0.675	-0.6067	-0.50	-0.5232	0.1676	0.6027	0.0393	0.1814	0.1616
2.05	2.06	2.0601	2.07	-0.50	-0.375	-0.3646	-0.25	-0.7190	0.1540	0.6858	0.0341	0.3706	0.1493
2.05	2.06	2.0601	2.07	-0.25	-0.125	-0.1084	0.00	0.1570	0.0980	0.1825	0.0237	0.9013	0.0957
2.05	2.06	2.0602	2.07	0.00	0.100	0.1074	0.20	0.3198	0.0840	-0.2175	0.0196	0.8262	0.0824
2.05	2.06	2.0602	2.07	0.20	0.300	0.3068	0.40	0.1356	0.0555	-0.3792	0.0129	0.9675	0.0535
2.05	2.06	2.0603	2.07	0.40	0.475	0.4824	0.55	0.0348	0.0532	-0.5061	0.0128	1.0640	0.0511
2.05	2.06	2.0604	2.07	0.55	0.600	0.6015	0.65	-0.1576	0.0564	-0.5059	0.0134	1.0637	0.0547
2.05	2.06	2.0604	2.07	0.65	0.700	0.7009	0.75	-0.3857	0.0532	-0.5097	0.0125	1.0330	0.0518
2.05	2.06	2.0604	2.07	0.75	0.800	0.8002	0.85	-0.4758	0.0545	-0.4823	0.0128	1.0340	0.0534
2.05	2.06	2.0604	2.07	0.85	0.900	0.8842	0.95	-0.5511	0.0716	-0.4136	0.0172	1.1235	0.0746
2.07	2.08	2.0799	2.09	-0.85	-0.675	-0.6031	-0.50	-0.2881	0.1721	0.3779	0.0427	0.1793	0.1710
2.07	2.08	2.0801	2.09	-0.50	-0.375	-0.3621	-0.25	-0.6687	0.1565	0.5576	0.0372	0.2606	0.1520
2.07	2.08	2.0799	2.09	-0.25	-0.125	-0.1088	0.00	-0.2612	0.0988	0.2833	0.0245	0.8576	0.0968
2.07	2.08	2.0799	2.09	0.00	0.100	0.1093	0.20	0.0394	0.0840	-0.1107	0.0205	0.8732	0.0823
2.07	2.08	2.0799	2.09	0.20	0.300	0.3053	0.40	0.2223	0.0556	-0.3198	0.0135	0.9458	0.0537
2.07	2.08	2.0800	2.09	0.40	0.475	0.4818	0.55	0.1489	0.0519	-0.4813	0.0130	1.0784	0.0504
2.07	2.08	2.0800	2.09	0.55	0.600	0.6015	0.65	-0.1069	0.0555	-0.5129	0.0136	0.9826	0.0535
2.07	2.08	2.0800	2.09	0.65	0.700	0.7009	0.75	-0.2966	0.0521	-0.5045	0.0126	0.9377	0.0504
2.07	2.08	2.0801	2.09	0.75	0.800	0.8006	0.85	-0.4781	0.0523	-0.5129	0.0126	0.9195	0.0512
2.07	2.08	2.0800	2.09	0.85	0.900	0.8838	0.95	-0.3445	0.0703	-0.4586	0.0171	0.9612	0.0726
2.09	2.10	2.0998	2.11	-0.85	-0.675	-0.6046	-0.50	-0.9341	0.1809	0.1958	0.0465	0.2191	0.1793
2.09	2.10	2.0998	2.11	-0.50	-0.375	-0.3634	-0.25	-0.8371	0.1607	0.4281	0.0399	0.5800	0.1586
2.09	2.10	2.0999	2.11	-0.25	-0.125	-0.1115	0.00	-0.1074	0.1073	0.2863	0.0273	0.6544	0.1046
2.09	2.10	2.0997	2.11	0.00	0.100	0.1100	0.20	0.3513	0.0915	-0.0636	0.0227	0.6060	0.0908
2.09	2.10	2.0997	2.11	0.20	0.300	0.3043	0.40	0.3612	0.0609	-0.2860	0.0151	0.9899	0.0588
2.09	2.10	2.0998	2.11	0.40	0.475	0.4820	0.55	-0.0188	0.0567	-0.4508	0.0145	0.9984	0.0549
2.09	2.10	2.0998	2.11	0.55	0.600	0.6016	0.65	-0.1831	0.0594	-0.4769	0.0149	1.0578	0.0573
2.09	2.10	2.0998	2.11	0.65	0.700	0.7004	0.75	-0.3803	0.0549	-0.5404	0.0136	1.1009	0.0534
2.09	2.10	2.0999	2.11	0.75	0.800	0.8009	0.85	-0.4656	0.0544	-0.5708	0.0134	0.9670	0.0535
2.09	2.10	2.0999	2.11	0.85	0.900	0.8842	0.95	-0.5455	0.0740	-0.4920	0.0184	0.9000	0.0775
2.11	2.12	2.1204	2.13	-0.85	-0.675	-0.6046	-0.50	-0.5309	0.1655	0.0713	0.0436	0.3861	0.1600
2.11	2.12	2.1204	2.13	-0.50	-0.375	-0.3662	-0.25	-0.8976	0.1450	0.2334	0.0373	0.2546	0.1405
2.11	2.12	2.1202	2.13	-0.25	-0.125	-0.1124	0.00	-0.1910	0.0999	0.3506	0.0261	0.6236	0.0991
2.11	2.12	2.1203	2.13	0.00	0.100	0.1111	0.20	0.3997	0.0869	-0.0257	0.0222	0.7914	0.0854
2.11	2.12	2.1202	2.13	0.20	0.300	0.3037	0.40	0.3499	0.0578	-0.2447	0.0148	0.8968	0.0556
2.11	2.12	2.1203	2.13	0.40	0.475	0.4814	0.55	0.1470	0.0523	-0.4583	0.0137	1.0076	0.0505
2.11	2.12	2.1203	2.13	0.55	0.600	0.6022	0.65	-0.2096	0.0546	-0.5289	0.0139	1.0162	0.0530
2.11	2.12	2.1203	2.13	0.65	0.700	0.7006	0.75	-0.4029	0.0499	-0.5427	0.0127	0.9227	0.0485
2.11	2.12	2.1204	2.13	0.75	0.800	0.8012	0.85	-0.4410	0.0484	-0.6207	0.0121	0.9099	0.0480
2.11	2.12	2.1204	2.13	0.85	0.900	0.8849	0.95	-0.3854	0.0669	-0.5386	0.0169	0.8510	0.0695
2.13	2.14	2.1401	2.15	-0.85	-0.675	-0.6026	-0.50	-0.5307	0.1529	-0.0624	0.0417	0.4208	0.1537
2.13	2.14	2.1399	2.15	-0.50	-0.375	-0.3678	-0.25	-0.9695	0.1381	0.0979	0.0367	0.5086	0.1363
2.13	2.14	2.1397	2.15	-0.25	-0.125	-0.1142	0.00	-0.0612	0.1003	0.3511	0.0271	0.6756	0.0994
2.13	2.14	2.1397	2.15	0.00	0.100	0.1128	0.20	0.2684	0.0863	0.0484	0.0232	0.7927	0.0853
2.13	2.14	2.1398	2.15	0.20	0.300	0.3035	0.40	0.4475	0.0579	-0.2631	0.0153	0.9273	0.0557
2.13	2.14	2.1399	2.15	0.40	0.475	0.4817	0.55	-0.0795	0.0518	-0.4491	0.0140	1.0702	0.0500
2.13	2.14	2.1399	2.15	0.55	0.600	0.6019	0.65	-0.3234	0.0536	-0.5201	0.0141	1.0528	0.0522
2.13	2.14	2.1399	2.15	0.65	0.700	0.7008	0.75	-0.4119	0.0486	-0.6194	0.0125	0.8958	0.0472
2.13	2.14	2.1400	2.15	0.75	0.800	0.8015	0.85	-0.4821	0.0461	-0.6663	0.0118	0.8416	0.0457
2.13	2.14	2.1400	2.15	0.85	0.900	0.8857	0.95	-0.4682	0.0645	-0.6302	0.0163	0.8720	0.0674
2.15	2.16	2.1607	2.17	-0.85	-0.675	-0.6015	-0.50	-0.5742	0.1571	-0.2556	0.0444	0.4779	0.1555
2.15	2.16	2.1605	2.17	-0.50	-0.375	-0.3683	-0.25	-0.8554	0.1447	-0.0435	0.0392	0.8432	0.1437
2.15	2.16	2.1604	2.17	-0.25	-0.125	-0.1167	0.00	0.0230	0.1111	0.2568	0.0305	0.6583	0.1077
2.15	2.16	2.1603	2.17	0.00	0.100	0.1137	0.20	0.2594	0.0952	0.0334	0.0257	0.8394	0.0932
2.15	2.16	2.1604	2.17	0.20	0.300	0.3035	0.40	0.3256	0.0635	-0.2184	0.0171	0.8604	0.0613
2.15	2.16	2.1605	2.17	0.40	0.475	0.4812	0.55	0.1241	0.0552	-0.4753	0.0153	0.9263	0.0536
2.15	2.16	2.1605	2.17	0.55	0.600	0.6023	0.65	-0.3270	0.0569	-0.5382	0.0153	1.0061	0.0555
2.15	2.16	2.1606	2.17	0.65	0.700	0.7009	0.75	-0.3774	0.0507	-0.6382	0.0134	0.8582	0.0495
2.15	2.16	2.1606	2.17	0.75	0.800	0.8017	0.85	-0.4212	0.0470	-0.7017	0.0123	0.7661	0.0463
2.15	2.16	2.1606	2.17	0.85	0.900	0.8866	0.95	-0.4242	0.0669	-0.6783	0.0173	0.7889	0.0693

2.17	2.18	2.1800	2.19	-0.85	-0.675	-0.6002	-0.50	-0.7425	0.1552	-0.2379	0.0441	0.6907	0.1503
2.17	2.18	2.1800	2.19	-0.50	-0.375	-0.3675	-0.25	-0.7219	0.1418	-0.0590	0.0391	0.6144	0.1390
2.17	2.18	2.1799	2.19	-0.25	-0.125	-0.1173	0.00	-0.1686	0.1095	0.2044	0.0309	0.5656	0.1078
2.17	2.18	2.1799	2.19	0.00	0.100	0.1164	0.20	0.3207	0.0952	0.0942	0.0264	0.7437	0.0952
2.17	2.18	2.1799	2.19	0.20	0.300	0.3039	0.40	0.2694	0.0643	-0.2061	0.0178	0.7272	0.0615
2.17	2.18	2.1798	2.19	0.40	0.475	0.4816	0.55	0.1279	0.0547	-0.4449	0.0155	0.9636	0.0531
2.17	2.18	2.1800	2.19	0.55	0.600	0.6022	0.65	-0.2621	0.0555	-0.5354	0.0154	1.0430	0.0542
2.17	2.18	2.1800	2.19	0.65	0.700	0.7006	0.75	-0.3558	0.0494	-0.6117	0.0134	0.9043	0.0478
2.17	2.18	2.1801	2.19	0.75	0.800	0.8019	0.85	-0.4457	0.0453	-0.7443	0.0119	0.7423	0.0447
2.17	2.18	2.1800	2.19	0.85	0.900	0.8880	0.95	-0.4448	0.0645	-0.7025	0.0169	0.8372	0.0671
2.19	2.20	2.1998	2.21	-0.85	-0.675	-0.6005	-0.50	-0.6288	0.1548	-0.2617	0.0451	0.5807	0.1510
2.19	2.20	2.1997	2.21	-0.50	-0.375	-0.3682	-0.25	-0.1450	0.1416	-0.2070	0.0399	0.7156	0.1376
2.19	2.20	2.1995	2.21	-0.25	-0.125	-0.1184	0.00	-0.0664	0.1120	0.2272	0.0324	0.7677	0.1109
2.19	2.20	2.1997	2.21	0.00	0.100	0.1162	0.20	0.3999	0.0954	0.0566	0.0273	0.6715	0.0939
2.19	2.20	2.1996	2.21	0.20	0.300	0.3043	0.40	0.4498	0.0642	-0.1459	0.0185	0.7943	0.0620
2.19	2.20	2.1997	2.21	0.40	0.475	0.4809	0.55	0.1242	0.0551	-0.4557	0.0160	0.9852	0.0532
2.19	2.20	2.1997	2.21	0.55	0.600	0.6025	0.65	-0.1863	0.0550	-0.5339	0.0155	0.9518	0.0534
2.19	2.20	2.1998	2.21	0.65	0.700	0.7008	0.75	-0.3334	0.0480	-0.6545	0.0133	0.7661	0.0469
2.19	2.20	2.1998	2.21	0.75	0.800	0.8015	0.85	-0.4092	0.0434	-0.7622	0.0117	0.7625	0.0431
2.19	2.20	2.1998	2.21	0.85	0.900	0.8886	0.95	-0.2582	0.0617	-0.7381	0.0164	0.7873	0.0633
2.21	2.22	2.2201	2.23	-0.85	-0.675	-0.6022	-0.50	-0.7224	0.1630	-0.2615	0.0489	0.6304	0.1574
2.21	2.22	2.2199	2.23	-0.50	-0.375	-0.3684	-0.25	-0.3577	0.1508	-0.1660	0.0442	0.9334	0.1459
2.21	2.22	2.2201	2.23	-0.25	-0.125	-0.1191	0.00	-0.0704	0.1230	0.1233	0.0362	0.8519	0.1194
2.21	2.22	2.2202	2.23	0.00	0.100	0.1193	0.20	0.4715	0.1030	0.1069	0.0297	0.3992	0.1001
2.21	2.22	2.2201	2.23	0.20	0.300	0.3045	0.40	0.4536	0.0699	-0.1655	0.0203	0.8041	0.0667
2.21	2.22	2.2202	2.23	0.40	0.475	0.4808	0.55	0.1770	0.0580	-0.3952	0.0174	0.9784	0.0567
2.21	2.22	2.2202	2.23	0.55	0.600	0.6028	0.65	-0.1963	0.0574	-0.5460	0.0165	0.8964	0.0561
2.21	2.22	2.2202	2.23	0.65	0.700	0.7009	0.75	-0.3324	0.0499	-0.6587	0.0140	0.8681	0.0487
2.21	2.22	2.2203	2.23	0.75	0.800	0.8009	0.85	-0.3879	0.0445	-0.7612	0.0122	0.6456	0.0440
2.21	2.22	2.2203	2.23	0.85	0.900	0.8896	0.95	-0.3149	0.0627	-0.6995	0.0170	0.8620	0.0641
2.23	2.24	2.2404	2.25	-0.85	-0.675	-0.6052	-0.50	-0.2280	0.1548	-0.3340	0.0465	0.7351	0.1493
2.23	2.24	2.2402	2.25	-0.50	-0.375	-0.3670	-0.25	-0.5901	0.1400	-0.3062	0.0422	0.7119	0.1364
2.23	2.24	2.2403	2.25	-0.25	-0.125	-0.1207	0.00	-0.2062	0.1157	0.1238	0.0351	0.6554	0.1136
2.23	2.24	2.2402	2.25	0.00	0.100	0.1196	0.20	0.2959	0.0962	0.1714	0.0288	0.4723	0.0955
2.23	2.24	2.2402	2.25	0.20	0.300	0.3064	0.40	0.4319	0.0668	-0.1385	0.0201	0.8163	0.0649
2.23	2.24	2.2402	2.25	0.40	0.475	0.4818	0.55	0.1261	0.0550	-0.3569	0.0170	0.9347	0.0535
2.23	2.24	2.2402	2.25	0.55	0.600	0.6028	0.65	-0.1625	0.0546	-0.5278	0.0160	0.8760	0.0526
2.23	2.24	2.2403	2.25	0.65	0.700	0.7010	0.75	-0.2898	0.0459	-0.6585	0.0133	0.8282	0.0451
2.23	2.24	2.2403	2.25	0.75	0.800	0.8005	0.85	-0.3915	0.0410	-0.7480	0.0116	0.8167	0.0402
2.23	2.24	2.2404	2.25	0.85	0.900	0.8896	0.95	-0.2761	0.0562	-0.7491	0.0160	0.7906	0.0577
2.25	2.26	2.2590	2.27	-0.85	-0.675	-0.6044	-0.50	-0.2869	0.1606	-0.4415	0.0508	0.6817	0.1570
2.25	2.26	2.2593	2.27	-0.50	-0.375	-0.3670	-0.25	-0.4858	0.1480	-0.2985	0.0448	0.7695	0.1454
2.25	2.26	2.2592	2.27	-0.25	-0.125	-0.1224	0.00	-0.2024	0.1253	0.1474	0.0388	0.4376	0.1228
2.25	2.26	2.2591	2.27	0.00	0.100	0.1193	0.20	0.4705	0.1028	0.2210	0.0315	0.5700	0.1028
2.25	2.26	2.2591	2.27	0.20	0.300	0.3070	0.40	0.4386	0.0712	-0.1273	0.0221	0.7215	0.0700
2.25	2.26	2.2592	2.27	0.40	0.475	0.4809	0.55	0.0598	0.0582	-0.3434	0.0184	0.8422	0.0573
2.25	2.26	2.2592	2.27	0.55	0.600	0.6030	0.65	-0.0719	0.0568	-0.4751	0.0174	0.8356	0.0561
2.25	2.26	2.2592	2.27	0.65	0.700	0.7016	0.75	-0.2918	0.0486	-0.6348	0.0144	0.8227	0.0474
2.25	2.26	2.2592	2.27	0.75	0.800	0.7998	0.85	-0.3366	0.0427	-0.7509	0.0124	0.7574	0.0420
2.25	2.26	2.2593	2.27	0.85	0.900	0.8897	0.95	-0.2766	0.0579	-0.7142	0.0167	0.7202	0.0588
2.27	2.28	2.2800	2.29	-0.85	-0.675	-0.6066	-0.50	-0.1637	0.1682	-0.3207	0.0545	0.9864	0.1657
2.27	2.28	2.2799	2.29	-0.50	-0.375	-0.3666	-0.25	-0.3408	0.1536	-0.4177	0.0460	0.7366	0.1478
2.27	2.28	2.2797	2.29	-0.25	-0.125	-0.1213	0.00	-0.0868	0.1323	0.1403	0.0418	0.8670	0.1297
2.27	2.28	2.2798	2.29	0.00	0.100	0.1197	0.20	0.3004	0.1060	0.2578	0.0335	0.5101	0.1057
2.27	2.28	2.2798	2.29	0.20	0.300	0.3084	0.40	0.5554	0.0751	-0.0088	0.0240	0.7262	0.0733
2.27	2.28	2.2798	2.29	0.40	0.475	0.4818	0.55	0.1444	0.0612	-0.2660	0.0198	0.9130	0.0602
2.27	2.28	2.2799	2.29	0.55	0.600	0.6035	0.65	-0.1394	0.0587	-0.4759	0.0181	0.9800	0.0568
2.27	2.28	2.2799	2.29	0.65	0.700	0.7018	0.75	-0.3568	0.0497	-0.6285	0.0152	0.7568	0.0484
2.27	2.28	2.2799	2.29	0.75	0.800	0.7992	0.85	-0.3524	0.0440	-0.7476	0.0129	0.6507	0.0430
2.27	2.28	2.2799	2.29	0.85	0.900	0.8899	0.95	-0.2706	0.0581	-0.7329	0.0170	0.7347	0.0594
2.29	2.30	2.2995	2.31	-0.85	-0.675	-0.6089	-0.50	-0.2250	0.1671	-0.3239	0.0544	0.5540	0.1639
2.29	2.30	2.2994	2.31	-0.50	-0.375	-0.3655	-0.25	-0.0450	0.1486	-0.3372	0.0478	0.8514	0.1471
2.29	2.30	2.2995	2.31	-0.25	-0.125	-0.1238	0.00	-0.1683	0.1342	0.1211	0.0422	0.8756	0.1281
2.29	2.30	2.2996	2.31	0.00	0.100	0.1203	0.20	0.4594	0.1099	0.3074	0.0350	0.5122	0.1074
2.29	2.30	2.2995	2.31	0.20	0.300	0.3088	0.40	0.3735	0.0765	0.0435	0.0249	0.7036	0.0751
2.29	2.30	2.2995	2.31	0.40	0.475	0.4819	0.55	0.0047	0.0623	-0.2433	0.0206	0.8396	0.0610

2.29	2.30	2.2996	2.31	0.55	0.600	0.6039	0.65	-0.1637	0.0588	-0.4377	0.0188	0.8825	0.0576
2.29	2.30	2.2996	2.31	0.65	0.700	0.7019	0.75	-0.2541	0.0494	-0.6261	0.0152	0.7909	0.0477
2.29	2.30	2.2996	2.31	0.75	0.800	0.7987	0.85	-0.3654	0.0430	-0.7261	0.0130	0.7027	0.0424
2.29	2.30	2.2997	2.31	0.85	0.900	0.8895	0.95	-0.2188	0.0563	-0.6953	0.0171	0.8127	0.0571
2.31	2.32	2.3200	2.33	-0.85	-0.675	-0.6086	-0.50	0.0116	0.1698	-0.2571	0.0559	0.5577	0.1640
2.31	2.32	2.3200	2.33	-0.50	-0.375	-0.3657	-0.25	0.0029	0.1532	-0.3194	0.0492	0.7449	0.1477
2.31	2.32	2.3200	2.33	-0.25	-0.125	-0.1260	0.00	-0.1049	0.1343	0.2588	0.0443	0.6857	0.1305
2.31	2.32	2.3199	2.33	0.00	0.100	0.1190	0.20	0.4091	0.1090	0.3955	0.0351	0.4329	0.1084
2.31	2.32	2.3198	2.33	0.20	0.300	0.3113	0.40	0.4100	0.0802	0.0410	0.0266	0.6788	0.0766
2.31	2.32	2.3199	2.33	0.40	0.475	0.4825	0.55	0.0723	0.0624	-0.2182	0.0215	0.8140	0.0617
2.31	2.32	2.3200	2.33	0.55	0.600	0.6038	0.65	-0.1912	0.0581	-0.4300	0.0192	0.8382	0.0566
2.31	2.32	2.3199	2.33	0.65	0.700	0.7024	0.75	-0.3198	0.0494	-0.5942	0.0156	0.6350	0.0480
2.31	2.32	2.3200	2.33	0.75	0.800	0.7984	0.85	-0.3389	0.0426	-0.7257	0.0132	0.6413	0.0417
2.31	2.32	2.3201	2.33	0.85	0.900	0.8889	0.95	-0.2550	0.0547	-0.7433	0.0168	0.6930	0.0553
2.33	2.34	2.3399	2.35	-0.85	-0.675	-0.6100	-0.50	-0.4817	0.1783	-0.3457	0.0605	0.9133	0.1730
2.33	2.34	2.3397	2.35	-0.50	-0.375	-0.3686	-0.25	0.0540	0.1602	-0.2798	0.0526	0.6686	0.1575
2.33	2.34	2.3398	2.35	-0.25	-0.125	-0.1264	0.00	-0.2416	0.1411	0.2029	0.0486	0.4171	0.1377
2.33	2.34	2.3397	2.35	0.00	0.100	0.1196	0.20	0.1830	0.1173	0.3116	0.0394	0.4976	0.1166
2.33	2.34	2.3396	2.35	0.20	0.300	0.3115	0.40	0.3114	0.0856	0.1245	0.0295	0.5443	0.0839
2.33	2.34	2.3398	2.35	0.40	0.475	0.4828	0.55	0.0794	0.0674	-0.1877	0.0234	0.8287	0.0659
2.33	2.34	2.3397	2.35	0.55	0.600	0.6044	0.65	-0.2186	0.0618	-0.4561	0.0205	0.8426	0.0607
2.33	2.34	2.3398	2.35	0.65	0.700	0.7026	0.75	-0.3151	0.0511	-0.5907	0.0167	0.6911	0.0503
2.33	2.34	2.3397	2.35	0.75	0.800	0.7983	0.85	-0.3557	0.0443	-0.7276	0.0141	0.6513	0.0440
2.33	2.34	2.3398	2.35	0.85	0.900	0.8893	0.95	-0.2576	0.0563	-0.7154	0.0179	0.6429	0.0565
2.35	2.38	2.3726	2.40	-0.85	-0.675	-0.6103	-0.50	-0.0337	0.1154	-0.2385	0.0404	0.8077	0.1103
2.35	2.38	2.3730	2.40	-0.50	-0.375	-0.3647	-0.25	0.0151	0.1032	-0.2637	0.0349	0.6964	0.0989
2.35	2.38	2.3726	2.40	-0.25	-0.125	-0.1254	0.00	-0.1926	0.0930	0.0979	0.0321	0.7044	0.0909
2.35	2.38	2.3722	2.40	0.00	0.100	0.1172	0.20	0.0403	0.0773	0.2389	0.0272	0.3291	0.0767
2.35	2.38	2.3723	2.40	0.20	0.300	0.3130	0.40	0.2772	0.0576	0.1352	0.0203	0.5678	0.0564
2.35	2.38	2.3726	2.40	0.40	0.475	0.4837	0.55	0.1433	0.0438	-0.2449	0.0158	0.7349	0.0432
2.35	2.38	2.3729	2.40	0.55	0.600	0.6044	0.65	-0.1291	0.0392	-0.4321	0.0136	0.7843	0.0383
2.35	2.38	2.3732	2.40	0.65	0.700	0.7034	0.75	-0.2555	0.0322	-0.5913	0.0108	0.6892	0.0314
2.35	2.38	2.3732	2.40	0.75	0.800	0.7979	0.85	-0.2877	0.0280	-0.7084	0.0092	0.5646	0.0275
2.35	2.38	2.3734	2.40	0.85	0.900	0.8888	0.95	-0.2715	0.0348	-0.6990	0.0113	0.5836	0.0347
2.40	2.42	2.4261	2.45	-0.85	-0.675	-0.6169	-0.50	0.0927	0.1276	-0.0733	0.0457	0.6367	0.1194
2.40	2.42	2.4255	2.45	-0.50	-0.375	-0.3650	-0.25	0.2914	0.1091	-0.2691	0.0392	0.7933	0.1034
2.40	2.42	2.4253	2.45	-0.25	-0.125	-0.1278	0.00	-0.3216	0.0988	-0.0417	0.0367	0.6176	0.0978
2.40	2.42	2.4255	2.45	0.00	0.100	0.1147	0.20	-0.2045	0.0854	0.0874	0.0320	0.3229	0.0849
2.40	2.42	2.4253	2.45	0.20	0.300	0.3158	0.40	0.1595	0.0658	0.0665	0.0246	0.4677	0.0644
2.40	2.42	2.4255	2.45	0.40	0.475	0.4849	0.55	-0.0356	0.0477	-0.1905	0.0183	0.7325	0.0475
2.40	2.42	2.4257	2.45	0.55	0.600	0.6044	0.65	-0.1290	0.0416	-0.4093	0.0152	0.7311	0.0408
2.40	2.42	2.4260	2.45	0.65	0.700	0.7042	0.75	-0.2499	0.0331	-0.6078	0.0117	0.6281	0.0326
2.40	2.42	2.4260	2.45	0.75	0.800	0.7986	0.85	-0.3104	0.0289	-0.6991	0.0099	0.6021	0.0281
2.40	2.42	2.4261	2.45	0.85	0.900	0.8892	0.95	-0.2469	0.0349	-0.7196	0.0120	0.5143	0.0346
2.45	2.48	2.4746	2.50	-0.85	-0.675	-0.6189	-0.50	0.0303	0.1267	-0.1339	0.0479	0.6331	0.1201
2.45	2.48	2.4745	2.50	-0.50	-0.375	-0.3609	-0.25	0.1994	0.1089	-0.1429	0.0419	0.6704	0.1044
2.45	2.48	2.4748	2.50	-0.25	-0.125	-0.1291	0.00	-0.2970	0.1002	-0.0267	0.0386	0.6821	0.0990
2.45	2.48	2.4745	2.50	0.00	0.100	0.1089	0.20	-0.3013	0.0826	0.0147	0.0335	0.4088	0.0833
2.45	2.48	2.4740	2.50	0.20	0.300	0.3175	0.40	0.0090	0.0673	0.0310	0.0265	0.4619	0.0660
2.45	2.48	2.4745	2.50	0.40	0.475	0.4862	0.55	0.0711	0.0484	-0.1932	0.0194	0.6925	0.0478
2.45	2.48	2.4745	2.50	0.55	0.600	0.6045	0.65	-0.0242	0.0404	-0.3949	0.0157	0.7080	0.0398
2.45	2.48	2.4751	2.50	0.65	0.700	0.7048	0.75	-0.2116	0.0312	-0.5926	0.0115	0.6767	0.0305
2.45	2.48	2.4750	2.50	0.75	0.800	0.8001	0.85	-0.2275	0.0268	-0.6783	0.0098	0.6202	0.0263
2.45	2.48	2.4750	2.50	0.85	0.900	0.8900	0.95	-0.2157	0.0324	-0.6858	0.0117	0.5472	0.0321
2.50	2.53	2.5272	2.56	-0.85	-0.675	-0.6260	-0.50	-0.3861	0.1228	-0.0135	0.0497	0.4086	0.1174
2.50	2.53	2.5273	2.56	-0.50	-0.375	-0.3590	-0.25	0.2771	0.1026	-0.0312	0.0425	0.7878	0.0994
2.50	2.53	2.5269	2.56	-0.25	-0.125	-0.1272	0.00	-0.1878	0.0941	-0.1300	0.0384	0.6752	0.0939
2.50	2.53	2.5266	2.56	0.00	0.100	0.1061	0.20	-0.2430	0.0818	-0.1789	0.0344	0.3359	0.0817
2.50	2.53	2.5268	2.56	0.20	0.300	0.3174	0.40	0.0108	0.0680	0.0431	0.0280	0.4012	0.0672
2.50	2.53	2.5268	2.56	0.40	0.475	0.4880	0.55	0.0581	0.0479	-0.2278	0.0203	0.7179	0.0476
2.50	2.53	2.5273	2.56	0.55	0.600	0.6048	0.65	-0.0773	0.0389	-0.3900	0.0159	0.7308	0.0381
2.50	2.53	2.5274	2.56	0.65	0.700	0.7051	0.75	-0.1412	0.0288	-0.5601	0.0113	0.6254	0.0281
2.50	2.53	2.5276	2.56	0.75	0.800	0.8016	0.85	-0.2231	0.0247	-0.6470	0.0096	0.5040	0.0241
2.50	2.53	2.5277	2.56	0.85	0.900	0.8909	0.95	-0.2346	0.0292	-0.6909	0.0111	0.5151	0.0288
2.60	2.65	2.6495	2.70	-0.85	-0.675	-0.6359	-0.50	-0.1730	0.1081	-0.1774	0.0489	0.3888	0.1032
2.60	2.65	2.6485	2.70	-0.50	-0.375	-0.3621	-0.25	0.2051	0.1007	0.1869	0.0449	0.7900	0.0980

2.60	2.65	2.6477	2.70	-0.25	-0.125	-0.1191	0.00	0.1996	0.0927	-0.0301	0.0428	0.5766	0.0917
2.60	2.65	2.6472	2.70	0.00	0.100	0.0966	0.20	-0.2007	0.0817	-0.3266	0.0382	0.5846	0.0825
2.60	2.65	2.6455	2.70	0.20	0.300	0.3145	0.40	0.1125	0.0768	-0.0434	0.0350	0.6096	0.0758
2.60	2.65	2.6465	2.70	0.40	0.475	0.4904	0.55	0.1153	0.0502	-0.1965	0.0237	0.5355	0.0505
2.60	2.65	2.6475	2.70	0.55	0.600	0.6062	0.65	0.0565	0.0380	-0.3641	0.0172	0.6918	0.0372
2.60	2.65	2.6481	2.70	0.65	0.700	0.7046	0.75	-0.1412	0.0266	-0.4968	0.0116	0.5525	0.0263
2.60	2.65	2.6494	2.70	0.75	0.800	0.8030	0.85	-0.2331	0.0216	-0.5665	0.0092	0.4628	0.0211
2.60	2.65	2.6495	2.70	0.85	0.900	0.8924	0.95	-0.2179	0.0247	-0.6577	0.0103	0.4584	0.0242
2.70	2.75	2.7543	2.80	-0.85	-0.675	-0.6455	-0.50	0.0552	0.0906	-0.2561	0.0434	0.5384	0.0874
2.70	2.75	2.7535	2.80	-0.50	-0.375	-0.3667	-0.25	0.3501	0.0938	0.3325	0.0463	0.6295	0.0921
2.70	2.75	2.7532	2.80	-0.25	-0.125	-0.1110	0.00	-0.0138	0.0840	0.1042	0.0413	0.5454	0.0825
2.70	2.75	2.7529	2.80	0.00	0.100	0.0925	0.20	-0.0748	0.0802	-0.2701	0.0408	0.4430	0.0816
2.70	2.75	2.7527	2.80	0.20	0.300	0.3082	0.40	0.1514	0.0793	-0.0871	0.0389	0.6573	0.0763
2.70	2.75	2.7522	2.80	0.40	0.475	0.4915	0.55	0.0913	0.0512	-0.1429	0.0263	0.6169	0.0512
2.70	2.75	2.7533	2.80	0.55	0.600	0.6078	0.65	0.0337	0.0357	-0.3520	0.0176	0.4915	0.0348
2.70	2.75	2.7541	2.80	0.65	0.700	0.7043	0.75	-0.0617	0.0242	-0.4549	0.0115	0.5358	0.0239
2.70	2.75	2.7552	2.80	0.75	0.800	0.8019	0.85	-0.1803	0.0183	-0.5384	0.0085	0.4442	0.0178
2.70	2.75	2.7559	2.80	0.85	0.900	0.8930	0.95	-0.2329	0.0202	-0.6282	0.0092	0.4227	0.0199
2.80	2.85	2.8481	2.90	-0.85	-0.675	-0.6507	-0.50	0.1265	0.0884	-0.1100	0.0441	0.4175	0.0830
2.80	2.85	2.8487	2.90	-0.50	-0.375	-0.3746	-0.25	0.0693	0.0885	0.3180	0.0461	0.5985	0.0866
2.80	2.85	2.8484	2.90	-0.25	-0.125	-0.1074	0.00	0.0649	0.0863	0.1102	0.0451	0.5947	0.0840
2.80	2.85	2.8476	2.90	0.00	0.100	0.0944	0.20	0.2198	0.0839	-0.1091	0.0460	0.5068	0.0861
2.80	2.85	2.8469	2.90	0.20	0.300	0.3043	0.40	0.0457	0.0820	-0.2042	0.0424	0.5921	0.0788
2.80	2.85	2.8464	2.90	0.40	0.475	0.4931	0.55	0.0760	0.0539	-0.1040	0.0293	0.5402	0.0545
2.80	2.85	2.8469	2.90	0.55	0.600	0.6089	0.65	0.0868	0.0359	-0.2834	0.0189	0.5329	0.0353
2.80	2.85	2.8478	2.90	0.65	0.700	0.7065	0.75	-0.0487	0.0233	-0.4260	0.0118	0.5033	0.0228
2.80	2.85	2.8483	2.90	0.75	0.800	0.8012	0.85	-0.1271	0.0169	-0.4960	0.0084	0.4424	0.0165
2.80	2.85	2.8495	2.90	0.85	0.900	0.8921	0.95	-0.2068	0.0176	-0.6082	0.0086	0.3755	0.0174
2.90	2.95	2.9465	3.00	-0.85	-0.675	-0.6588	-0.50	-0.0508	0.0983	-0.2105	0.0530	0.4792	0.0940
2.90	2.95	2.9469	3.00	-0.50	-0.375	-0.3803	-0.25	0.1195	0.1041	0.2133	0.0565	0.5364	0.1007
2.90	2.95	2.9462	3.00	-0.25	-0.125	-0.1030	0.00	-0.0074	0.1005	0.1194	0.0557	0.4434	0.0991
2.90	2.95	2.9466	3.00	0.00	0.100	0.1024	0.20	0.0424	0.1007	-0.1555	0.0571	0.4558	0.1004
2.90	2.95	2.9468	3.00	0.20	0.300	0.3021	0.40	-0.0566	0.0919	-0.1196	0.0525	0.3555	0.0957
2.90	2.95	2.9447	3.00	0.40	0.475	0.4928	0.55	0.2255	0.0704	-0.1077	0.0404	0.4742	0.0713
2.90	2.95	2.9450	3.00	0.55	0.600	0.6094	0.65	0.1626	0.0448	-0.2530	0.0249	0.4708	0.0438
2.90	2.95	2.9468	3.00	0.65	0.700	0.7099	0.75	0.0411	0.0271	-0.3869	0.0146	0.4959	0.0265
2.90	2.95	2.9472	3.00	0.75	0.800	0.8026	0.85	-0.1251	0.0193	-0.4922	0.0100	0.4228	0.0187
2.90	2.95	2.9480	3.00	0.85	0.900	0.8902	0.95	-0.1773	0.0187	-0.5869	0.0096	0.4036	0.0184
3.00	3.05	3.0499	3.10	-0.85	-0.675	-0.6635	-0.50	0.2110	0.1141	-0.0233	0.0657	0.3069	0.1111
3.00	3.05	3.0486	3.10	-0.50	-0.375	-0.3831	-0.25	0.0755	0.1294	0.1369	0.0744	0.4964	0.1234
3.00	3.05	3.0483	3.10	-0.25	-0.125	-0.1095	0.00	-0.0850	0.1252	0.1076	0.0746	0.4717	0.1290
3.00	3.05	3.0502	3.10	0.00	0.100	0.1061	0.20	0.1180	0.1240	-0.1354	0.0751	0.3330	0.1262
3.00	3.05	3.0500	3.10	0.20	0.300	0.3014	0.40	0.1603	0.1082	-0.1116	0.0649	0.4423	0.1085
3.00	3.05	3.0476	3.10	0.40	0.475	0.4905	0.55	0.1031	0.0921	-0.1065	0.0537	0.5607	0.0919
3.00	3.05	3.0480	3.10	0.55	0.600	0.6084	0.65	0.1108	0.0582	-0.2240	0.0344	0.4929	0.0571
3.00	3.05	3.0491	3.10	0.65	0.700	0.7113	0.75	-0.0218	0.0322	-0.3599	0.0182	0.4719	0.0316
3.00	3.05	3.0505	3.10	0.75	0.800	0.8054	0.85	-0.0890	0.0219	-0.4979	0.0120	0.3988	0.0214
3.00	3.05	3.0511	3.10	0.85	0.900	0.8886	0.95	-0.1628	0.0204	-0.5705	0.0110	0.3102	0.0200
3.10	3.15	3.1460	3.20	-0.85	-0.675	-0.6713	-0.50	0.2073	0.1290	0.0082	0.0775	0.2953	0.1235
3.10	3.15	3.1454	3.20	-0.50	-0.375	-0.3835	-0.25	-0.0643	0.1553	0.1675	0.0930	0.4194	0.1446
3.10	3.15	3.1461	3.20	-0.25	-0.125	-0.1176	0.00	0.2205	0.1520	0.0355	0.0934	0.4909	0.1506
3.10	3.15	3.1451	3.20	0.00	0.100	0.1091	0.20	0.3621	0.1521	-0.0420	0.0929	0.5750	0.1438
3.10	3.15	3.1463	3.20	0.20	0.300	0.3041	0.40	0.1536	0.1283	0.0769	0.0792	0.7067	0.1249
3.10	3.15	3.1456	3.20	0.40	0.475	0.4881	0.55	0.3072	0.1143	-0.0264	0.0716	0.5567	0.1176
3.10	3.15	3.1447	3.20	0.55	0.600	0.6090	0.65	0.1144	0.0768	-0.1893	0.0458	0.6455	0.0745
3.10	3.15	3.1460	3.20	0.65	0.700	0.7098	0.75	0.0467	0.0388	-0.3453	0.0226	0.4439	0.0384
3.10	3.15	3.1470	3.20	0.75	0.800	0.8077	0.85	-0.1038	0.0245	-0.4559	0.0139	0.4162	0.0238
3.10	3.15	3.1471	3.20	0.85	0.900	0.8869	0.95	-0.1536	0.0223	-0.5558	0.0124	0.3202	0.0219
3.20	3.27	3.2581	3.33	-0.85	-0.675	-0.6713	-0.50	0.0152	0.1360	0.0495	0.0827	0.1614	0.1307
3.20	3.27	3.2573	3.33	-0.50	-0.375	-0.3882	-0.25	-0.0947	0.1609	0.0743	0.0974	0.8253	0.1542
3.20	3.27	3.2561	3.33	-0.25	-0.125	-0.1176	0.00	0.0917	0.1761	0.0559	0.1035	0.7144	0.1613
3.20	3.27	3.2595	3.33	0.00	0.100	0.1053	0.20	0.4366	0.1563	0.1862	0.1022	0.3908	0.1527
3.20	3.27	3.2582	3.33	0.20	0.300	0.3014	0.40	0.2559	0.1342	0.1901	0.0835	0.1511	0.1364
3.20	3.27	3.2587	3.33	0.40	0.475	0.4834	0.55	0.4269	0.1274	0.0891	0.0811	0.4187	0.1297
3.20	3.27	3.2577	3.33	0.55	0.600	0.6108	0.65	0.2870	0.0927	-0.2165	0.0577	0.3708	0.0908
3.20	3.27	3.2569	3.33	0.65	0.700	0.7094	0.75	0.0881	0.0436	-0.2924	0.0263	0.5134	0.0429

3.20	3.27	3.2604	3.33	0.75	0.800	0.8100	0.85	-0.0347	0.0244	-0.4619	0.0141	0.3834	0.0235
3.20	3.27	3.2598	3.33	0.85	0.900	0.8857	0.95	-0.1665	0.0228	-0.5355	0.0131	0.3091	0.0224

VITA

SHANKAR D. ADHIKARI

2004 - 2007	B.Sc., Physics Tribhuvan University Kathmandu, Nepal
2008 - 2011	M.Sc., Physics Tribhuvan University Kathmandu, Nepal
2012 - 2018	Ph.D., Physics Florida International University Miami, Florida

SELECTED PUBLICATIONS AND PRESENTATIONS

1. Freese, A., Puentes, D., Adhikari, S., Badui, R., Guo, L., Raue, B. *"Extraction of t slopes from experimental $\gamma p \to K^+\Lambda$ and $\gamma p \to K^+\Sigma^\circ$ cross section data"*, Physical Review C 96 (4), 044601 (2017)
2. Bono, J., Guo, L., Raue, B., Adhikari, S., Kunkel, M., and et al. *"First measurement of Ξ^- polarization in photoproduction"*, Physics Letters B 783, 280-286 (2018)
3. Adhikari, S., Guo, L., Raue, B. *"Measurement of Polarization observables of Λ in the reaction $\gamma p \to K^+\Lambda$"*, NSTAR 2017, Columbia, SC
4. Adhikari, S., Guo, L., Raue, B. *"Measurement of Polarization observables in the reaction $\gamma p \to K^+\Lambda$"*, APS April Meeting 2018 Columbus, OH